Alfred-Wegener-Institut Helmholtz Zentrum für Polar- und Meeresforschung

Forschungsstelle Potsdam, Sektion Periglazialforschung

Climatic drivers of retrogressive thaw slump activity and resulting sediment and carbon release to the nearshore zone of Herschel Island, Yukon Territory, Canada

Dissertation

zur Erlangung des akademischen Grades

"doctor rerum naturalium"

(Dr. rer. nat.)

in der Wissenschaftsdisziplin "Geologie"

eingereicht an der

Mathematisch-Naturwissenschaftlichen Fakultät

der Universität Potsdam

von

Stefanie Weege

Potsdam, den 23. November 2016

Published online at the
Institutional Repository of the University of Potsdam:
URN urn:nbn:de:kobv:517-opus4-397947
http://nbn-resolving.de/urn:nbn:de:kobv:517-opus4-397947

'You see, Momo,' he told her one day, 'it's like this: Sometimes, when you've a very long street ahead of you, you think how terribly long it is and feel sure you'll never get it swept.' He gazed silently into space before continuing. 'And then you start to hurry,' he went on. 'You work faster and faster, and every time you look up there seems to be just as much left to sweep as before, and you try even harder, and you panic, and in the end you're out of breath and have to stop - and still the street stretches away in front of you. That's not the way to do it.' He pondered a while. Then he said, 'You must never think of the whole street at once, understand? You must only concentrate on the next step, the next breath, the next stroke of the broom, and the next, and the next. Nothing else.' Again he paused for thought before adding, 'That way you enjoy your work, which is important, because then you make a good job of it. And that's how it ought to be.'

Michael Ende in Momo 1973

Table of Contents

Abstract

The Yukon Coast in Canada is an ice-rich permafrost coast and highly sensitive to changing environmental conditions. Retrogressive thaw slumps are a common thermoerosion feature along this coast, and develop through the thawing of exposed ice-rich permafrost on slopes and removal of accumulating debris. They contribute large amounts of sediment, including organic carbon and nitrogen, to the nearshore zone.

The objective of this study was to 1) identify the climatic and geomorphological drivers of sediment-meltwater release, 2) quantify the amount of released meltwater, sediment, organic carbon and nitrogen, and 3) project the evolution of sediment-meltwater release of retrogressive thaw slumps in a changing future climate.

The analysis is based on data collected over 18 days in July 2013 and 18 days in August 2012. A cut-throat flume was set up in the main sediment-meltwater channel of the largest retrogressive thaw slump on Herschel Island. In addition, two weather stations, one on top of the undisturbed tundra and one on the slump floor, measured incoming solar radiation, air temperature, wind speed and precipitation. The discharge volume eroding from the ice-rich permafrost and retreating snowbanks was measured and compared to the meteorological data collected in real time with a resolution of one minute.

The results show that the release of sediment-meltwater from thawing of the ice-rich permafrost headwall is strongly related to snowmelt, incoming solar radiation and air temperature. Snowmelt led to seasonal differences, especially due to the additional contribution of water to the eroding sediment-meltwater from headwall ablation, lead to dilution of the sediment-meltwater composition. Incoming solar radiation and air temperature were the main drivers for diurnal and inter-diurnal fluctuations. In July (2013), the retrogressive thaw slump released about 25 000 m^3 of sediment-meltwater, containing 225 kg dissolved organic carbon and 2050 t of sediment, which in turn included 33 t organic carbon, and 4 t total nitrogen. In August (2012), just 15 600 m^3 of sediment-meltwater was released, since there was no additional contribution from snowmelt. However, even without the additional dilution, 281 kg dissolved organic carbon was released. The sediment concentration was twice as high as in July, with sediment contents of up to 457 g l^{-1} and 3058 t of sediment, including 53 t organic carbon and 5 t nitrogen, being released.

In addition, the data from the 36 days of observations from Slump D were upscaled to cover the main summer season of 1 July to 31 August (62 days) and to include all 229 active retrogressive thaw slumps along the Yukon Coast. In total, all retrogressive thaw slumps along the Yukon Coast contribute a minimum of 1.4 Mio. m^3 sediment-meltwater each thawing season, containing a minimum of 172 000 t sediment with 3119 t organic carbon, 327 t nitrogen and 17 t dissolved organic carbon. Therefore, in addition to the coastal erosion input to the Beaufort Sea, retrogressive thaw slumps additionally release 3 % of sediment and 8 % of organic carbon into the ocean. Finally, the future evolution of retrogressive thaw slumps under a warming scenario with summer air temperatures increasing by 2-3 °C by 2081-2100, would lead to an increase of 109-114% in release of sediment-meltwater.

It can be concluded that retrogressive thaw slumps are sensitive to climatic conditions and under projected future Arctic warming will contribute larger amounts of thawed permafrost material (including organic carbon and nitrogen) into the environment.

Kurzfassung

Die Yukon Küste in Kanada ist eine eisreiche Permafrost Küste und reagiert hoch sensibel auf verändernde Umweltbedingungen. Rückschreitende auftaubedingte Rutschungen sind vielzählig entlang der Küste und entstehen, wenn exponierter eisreicher Permafrost an Hängen auftaut und der daraus resultierende Schlamm abtransportiert wird. Diese Rutschungen tragen große Mengen von Sediment, inklusive organischen Kohlenstoff und Stickstoff, in den küstennahen Bereich.

Das Ziel dieser Studie war 1) die klimatischen und geomorphologischen Antriebskräfte für die Freisetzung von Sediment-Schmelzwasser zu identifizieren 2) die Mengen an Schmelzwasser, Sediment, organischen Kohlenstoff und Stickstoff zu quantifizieren und 3) die Entwicklung der Sediment-Schmelzwasser-Freigabe von rückschreitenden Rutschungen unter zukünftigen klimatischen Veränderungen abzuschätzen.

Die größte rückschreitende Rutschung auf Herschel Island wird als „Slump D“ bezeichnet und steht im Fokus dieser Arbeit. Die Analysen basierten auf den Daten, die über 18 Tage im Juli (2013) und 18 Tage im August (2012) erhoben wurden. Eine Abfluss-Messrinne wurde in den Haupt-Sediment-Schmelzwasser-Kanal eingebaut, um die Sediment-Schmelzwasser-massen zu erfassen. Zusätzlich wurden zwei Wetterstationen aufgebaut (auf der unberührten Tundra und innerhalb der Erosionsfläche), die Sonneneinstrahlung, Lufttemperatur, Windgeschwindigkeit und Niederschlagsmenge aufzeichneten. Das Abflussvolumen, das vom auftauenden, eisreichen Permafrost und den schmelzenden Schneebänken ablief, wurde gemessen und mit den meteorologischen Daten in Echtzeit mit einer Auflösung von einer Minute verglichen.

Die Ergebnisse zeigen, dass eine Freigabe von Sediment-Schmelzwasser beim Auftauen der eisreichen Permafrost-Steilklippe stark von Schneeschmelze, Sonneneinstrahlung und Lufttemperatur abhängen. Die Schneeschmelze führt zu saisonalen Unterschieden, besonders durch den zusätzlichen Betrag von Wasser zu dem erodierenden Sediment-Schmelzwasser der auftauenden Steilklippe. Dies führt zu einer Verdünnung des Sediment-Schmelzwassers. Sonneneinstrahlung und Lufttemperaturen waren die Hauptantriebskräfte für die Schwankungen im Tagesverlauf und die Unterschiede zwischen den Tagen. Die rückschreitende Rutschung gab im Juli (2013) ungefähr 25 000 m³ Sediment-Schmelzwasser frei, welches 225 kg gelösten organischen Kohlenstoff, 2050 t Sediment, inklusive 33 t

organischen Kohlenstoff und 4 t Stickstoff enthielt. Im August (2012) fehlte der zusätzliche Eintrag der Schneeschmelze und das Sediment-Schmelzwasser-Volumen war geringer mit 15 600 m^3. Dennoch, ohne die zusätzliche Verdünnung, wurden 281 kg gelöster organischer Kohlenstoff freigesetzt. Die Sedimentkonzentration war doppelt so hoch und führte zu einem Sedimentgehalt mit bis zu 457 $g\,l^{-1}$ zu 3058 t Sediment, inklusive 53 t organischen Kohlenstoff und 5 t Stickstoff.

Zusätzlich wurden die Daten der 36-tägigen Abflussmessung der rückschreitenden Rutschung auf 62 Tage, von 1. Juli bis 31. August auf alle 229 aktiven Rutschungen entlang der Yukon Küste hochgerechnet. Es wurde diskutiert, dass alle rückschreitenden Rutschungen entlang der Yukon Küste zusammen mindestens 1,4 Mio. m^3 Sediment-Schmelzwasser während jeder Auftausaison freigeben. Diese enthalten ein Minimum von 172 000 t Sediment, 3119 t organischen Kohlenstoff, 327 t Stickstoff und 17 t gelösten organischen Kohlenstoff. Daher kann zusammengefasst werden, dass zusätzlich zur Küstenerosion von allen Rutschungen noch ein zusätzlicher Beitrag von 3 % Sediment und 8 % organischen Kohlenstoff in die Beaufort See eingetragen wird. Schließlich wurde die zukünftige Entwicklung dieser rückschreitenden Rutschungen bei einem Temperaturanstieg von 2-3 °C bis 2081-2100 diskutiert. Dies könnte zu einem Anstieg der Sediment-Schmelzwasser-Freigabe von 109-114 % führen.

Es kann daraus geschlossen werden, dass rückschreitende Rutschungen sensibel auf Klimabedingungen reagieren und mit der Arktischen Erwärmung größere Mengen an auftauenden Permafrost (inklusive organischen Kohlenstoff und Stickstoff) in die Umwelt freigeben werden.

Abbreviations and nomenclature

Notation	Meaning
cm	centimeter
CO_2	carbon dioxide
DGPS	Differential Global Positioning System
DIC	dissolved inorganic carbon
DOC	dissolved organic carbon
g	gram
h	hour
HCO_{3-}	hydrogen carbonate
i.e.	id est („it is“)
kg	kilogram
km^2	square kilometer
l	liter
LiDAR	Light Detection And Ranging
m	meter
ml	milliliter
$m^2\ s^{-1}$	square meter per second
Pg	petagram=10^{15} gram
pH	potential of hydrogen
R-squared	coefficient of determination
t	tons
TOC/TN	total organic carbon/ total nitrogen ratio
UTC	Coordinated Universal Time
VPDB	Vienna Pee Dee Belemnite standard
vol %	per cent by volume
wt %	per cent by weight
~	approximately

°C	degrees Celsius
$\delta^{13}C$ [‰]	ratio of $^{13}C/^{12}C$ ratio of the sample relative to the standard in per mil
µ	10^{6}
%	percent; a number or ratio as a fraction of 100
‰	per mille; a number or ratio as a fraction of 1000

1. Introduction

Approximately 24 % of the landmass in the northern hemisphere is affected by permafrost and is highly sensitive to climatic change (Schaefer et al., 2011; Zhang et al., 1999). Current climate models project an increase of Arctic mean annual surface air temperatures by up to 8.3 ± 1.9 °C until 2081-2100 compared to 1986-2005 (Collins et al., 2013). These rising air temperatures will lead to warming of permafrost and to an increase in active layer thickness, a process that has commenced in most of the northern hemisphere (Romanovsky et al., 2010; Schaefer et al., 2011; Schuur et al., 2008). Permafrost thawing will have two main consequences: Firstly, an impact on ecosystems and climate due to the release and remobilization of organic carbon formerly stored in frozen ground, termed the "Permafrost Carbon Feedback" (Hugelius et al., 2014; Schaefer et al., 2014; Vonk et al., 2013). Secondly, permafrost warming will lead to thaw settlement, threatening infrastructure, increasing thermokarst and/or permafrost-thaw related mass movements and changing hydrological pathways (Nelson et al., 2001 (Boike et al., 2012; Jorgenson et al., 2006; Lantuit and Pollard, 2005; Nelson et al., 2001).

Retrogressive thaw slumps are a form of mass movement found exclusively in permafrost regions. They are currently increasing in frequency, leading to heightened release of large quantities of organic carbon and nutrients to the environment (Lantuit and Pollard, 2005, 2008; Lantz and Kokelj, 2008). Retrogressive thaw slumps are backward retreating thermal erosion features which form C-shaped depressions (Lantuit et al., 2012b). They are initiated by thawing of exposed ice-rich permafrost on a steep slope and removal of debris by down sliding mudflows, wave erosion along coasts, or fluvial erosion along lake shores or river banks (Burn and Lewkowicz, 1990; Kokelj et al., 2013; Lantuit et al., 2012b). Climatic factors such as solar radiation, air temperature, rain, wind speed, debris, and snow cover affect the ablation of the headwall (Lewkowicz, 1986, 1987). Sunny days lead to high ablation rates, whereas thick debris and snow cover protect the ice (Lewkowicz, 1987).

Traditionally, analyses of retrogressive thaw slump evolution have focused on the ablation of the headwall, providing substantial moisture required to drive the eroding material out of the slump (e.g. Grom and Pollard, 2008; Lantuit and Pollard, 2005; Lewkowicz, 1986; Lewkowicz, 1987). However, the output of sediment-meltwater does not necessary reflect ablation. Kokelj et al. (2015) show that heavy rainfall events can increase the likelihood of

large debris flows in retrogressive thaw slumps. In addition, sediment-meltwater output is controlled by the complex geomorphology of these landforms, the deposition processes in the slump floor and the seasonal and/or daily variations in climatic forcing (Kokelj et al., 2013; Lantuit et al., 2012b; Lewkowicz, 1986).

Thawing permafrost in retrogressive thaw slumps leads to the release of massive amounts of freshwater, sediment, organic carbon, and nitrogen (Fritz et al., 2015; Keuper et al., 2012; Kokelj et al., 2013; Lantuit et al., 2012b; Vonk et al., 2013). This material is derived from the organic rich top layer and the ice-rich layer underneath, composed of ice wedges and massive ground ice. The released organic carbon and nutrients have a strong effect on the coastal ecosystem and are highly biolabile (Battin et al., 2008; Vonk et al., 2013).

The aim of this study is to assess the influence of climatic forcing on the output of the slump (meltwater, sediment, organic carbon, and nitrogen), that is discharged from the slump outlet on a daily, monthly, and seasonal basis. Furthermore, it will quantify the potential increase of future sediment-meltwater discharge (Figure 1). The specific objectives of the study are:

1. Identifying the climatic drivers of thaw in a retrogressive thaw slump, and assess their respective contribution to discharge
2. Quantifying the amount of sediment-meltwater being discharged from the retrogressive thaw slump with specific focus on the amount of organic carbon and nitrogen released into the near shore zone
3. Project the evolution of sediment-meltwater release from this retrogressive thaw slump under changing climatic conditions

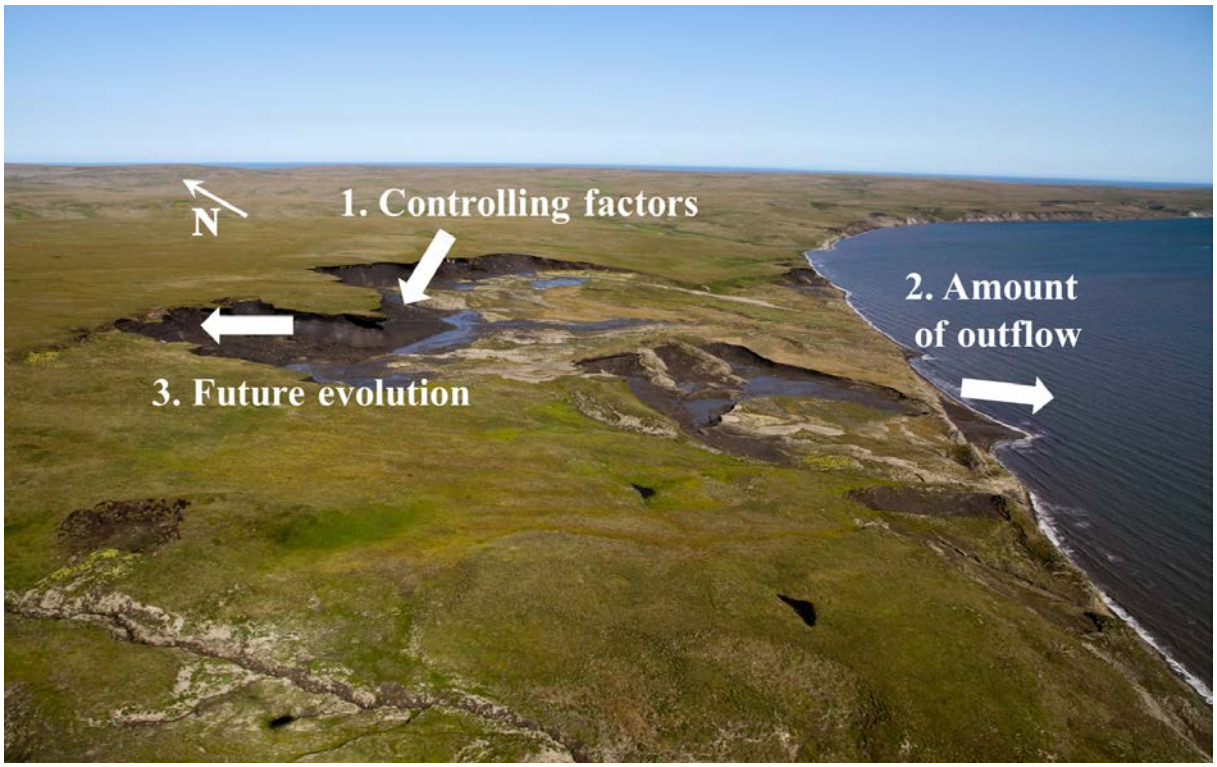

Figure 1. Illustrates the objectives of this study: 1) Identifying the controlling factors of snowmelt and permafrost thaw; 2) quantifying the release of sediment-meltwater; and 3) predicting future evolution of sediment-meltwater release.

2. Scientific Background

2.1. Permafrost

Permafrost is defined as ground which stays at or below 0 °C for at least two consecutive years (Permafrost Subcommittee, 1988). It affects large areas of the high latitudes and high mountain regions (Brown et al., 1997). 24 % of the northern hemisphere landmass is affected by permafrost (Zhang et al., 1999). Permafrost exists along the continental shelves of Siberia, Canada, and Alaska below the Arctic Ocean. It is called subsea permafrost and developed during the last Ice Age as terrestrial permafrost when sea level was more than 125 m lower than today (Schuur et al., 2015).

Permafrost is classified in three zones: continuous permafrost with coverage > 90 %, discontinuous/sporadic areas with 10-90 % coverage, and isolated patches with less than 10 % permafrost affected ground (French, 2007; Figure 2). Negative ground temperatures are associated with negative mean annual air temperatures due to very low winter temperatures, but are also influenced by snow, vegetation cover, and soil properties (Burn and Zhang, 2009; Romanovsky et al., 2002). The active layer is the top layer of permafrost, which thaws during warm summer days and refreezes in winter (French, 2007).

Permafrost can contain ice, which is then called “ground ice”. There are several origins of ground ice in permafrost. Ground ice can occur as pore ice, when soil freezes and the existing water freezes in situ. It can also occur as segregated ice when water moves to the freezing plane and forms ice lenses. There are two more origins of ground ice, one is intrusive ice when water injects under pressure and the other one is called vein ice when surface water penetrates into soil cracks e.g. ice wedges. In the western Canadian Arctic, ice wedges form the third largest volume of ground-ice (20-35 %; French, 2007)). Ice wedges develop and grow due to thermal-contraction cracking and infilling of ice. Ground ice can form relatively pure and massive ice bodies. These ice bodies are often several meters-thick and are characterized by gravimetric ice content >250 %. Those mainly originate as segregated ice or buried glacier ice (French, 2007).

Permafrost is highly sensitive to changes in the climate. Increasing air temperature or snow cover can change the energy balance of the ground and lead to warmer ground temperatures, active layer thickening, and may hinder refreezing of the ground in winter. It can lead to

permafrost degradation and thermal erosion. Thermal erosion of ice-rich permafrost is a combination of thermal thawing and mechanical removal of material (Harris, 2002). It can induce thermokarst, taliks, or retrogressive thaw slumps (French, 2007).

Thawing of ice-rich permafrost can also threaten infrastructure in permafrost regions (Nelson et al., 2001). Thaw-induced damages to roads, residential buildings, rail roads, power stations, and airports were reported in the literature (Streletskiy et al., 2012). The majority of the infrastructures was built for current climatic conditions and future warming could lead to its severe destabilization (Streletskiy et al., 2012).

Permafrost soils store large quantities of carbon. The surface permafrost carbon pool of the top 3 m is estimated to be 1035 ± 150 Pg carbon (Hugelius et al., 2014). That is more than the atmospheric carbon content with 730 Pg (Zimov et al., 2006). The release of even a small fraction of carbon due to thawing permafrost in forms of CO_2 and methane into the atmosphere is expected to accelerate climatic changes (Hugelius et al., 2014; Schuur et al., 2015).

Arctic permafrost coastlines often consist of consolidated sediments due to frozen ice (Günther et al., 2013; Rampton, 1982; Schirrmeister et al., 2011). These sediments are organic rich and contain large amounts of carbon (Fritz et al., 2012). In particular the Arctic coast is vulnerable to thermal erosion and environmental changes. Prolonging open water seasons, extending summer seasons, rising thawing degree days, increase of storm events, and sea level rise will accelerate coastal erosion (Lantuit et al., 2012a). Retrogressive thaw slumps are a wide spread phenomena along these ice-rich permafrost coasts (Wolfe et al., 2001). An increase in coastal erosion might accelerate their retreat and lead to additional slump formation (Lantuit et al., 2012b). This study focuses on retrogressive thaw slump sensibility to climate and their release of freshwater, sediment, carbon, and nitrogen.

Figure 2. The map of the Arctic shows the permafrost distribution. In the northern hemisphere permafrost is classified in continuous, discontinuous, sporadic, isolated patches, and subsea permafrost (Brown et al., 1997). The investigated area is along the Yukon Coast in northwest Canada.

2.2. Retrogressive Thaw Slumps

Retrogressive thaw slumps are backward retreating thermal erosion features. They are initiated by thawing of exposed ice-rich sediment and removal of debris due to down sliding mudflows and erosion along coastal, river, or lake shorelines (French, 2007). It is a form of thermokarst and can be found where unconsolidated ice-rich sediment thaws e.g. in Siberia, Alaska, Canada, and on the South Shetland Islands in the Antarctic (Ashastina et al., 2016; Lantuit and Pollard, 2005; Leibman, 1995; Oliva and Ruiz-Fernández, 2015; Séjourné et al., 2015). They have been observed in forests, tundra, and polar deserts, along coasts, river, lake shorelines and inland (Czudek and Demek, 1970; French, 1974; French, 2007; Leibman et al., 2008; Mackay, 1966; Oliva and Ruiz-Fernández, 2015; Zoltai and Pettapiece, 1973).

The morphology of an active retrogressive thaw slump from top to bottom includes (1) the vertical headwall with the active layer and ice-poor permafrost; (2) the steep thermal erosion headwall with ablation of the ice-rich permafrost; and (3) the slump floor with a mud pool and a slope evacuating the accumulated debris. Debris can be removed by consistently moderate mud flows or sporadic mass movements (Lantuit et al., 2012b; Figure 3) The retreat of retrogressive thaw slumps leaves bare soil behind in the slump floor. That slump floor is then slowly revegetated by pioneering vegetation species. The composition of the vegetation in the disturbed zone keeps being altered for several hundred years (Cray and Pollard, 2015).

The stabilization of a retrogressive thaw slump depends on the balance of removal of debris and the release of newly liquefied debris. In Canada, it was observed that retrogressive thaw slumps develop rapidly and stabilize within 30-50 years (French, 2007). Their activity can occur in pulses and active headwalls can develop along former headwall scarps (a process termed “polycyclicity”). The pace of that polycyclicity depends on the capacity of the terrain to enable down sliding debris, the ice-content, the liquefaction of material, and its removal (Lantuit et al., 2012b).

Mega retrogressive thaw slumps (greater than 5 ha) were identified along the Yukon Coast, in the Mackenzie Mountains, and on the Peel Plateau in northwest Canada (Kokelj et al., 2013; Lantuit et al., 2012b). In the Siberian Yana Highlands, a very large mega retrogressive thaw slumps with a retreat rate of 15 m per year, 80 m depth and 800 m width was also observed (Ashastina et al., 2016). The Canadian retrogressive thaw slumps of the western Canadian Arctic generally show retreat rates of up to 9 m per year, headwall heights of 20 m and/or headwall length greater than 1000 m (Kokelj et al., 2013; Lantuit et al., 2012b).

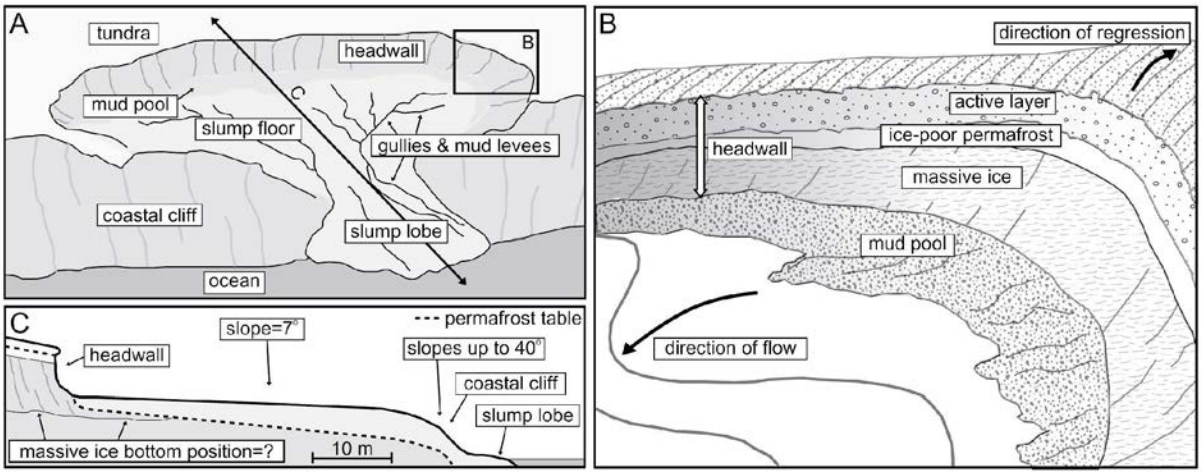

Figure 3. Schematic structure of an active retrogressive thaw slump showing the entire landform from an oblique perspective (A), with a focus on the headwall (B), and a cross section (C). Retrogressive thaw slumps develop when ice-rich permafrost is exposed e.g. through wave erosion along the coast. Ice-rich permafrost and massive ice in the headwall thaws, erodes into the mud pool, and is evacuated through the slump lobe via gullies and mud levees down into the ocean. The headwall continues to cut into undisturbed tundra as long as debris gets removed from the thawing ice-rich permafrost (Lantuit and Pollard, 2005).

The evolution of retrogressive thaw slumps depends on air temperature, solar radiation, precipitation, snow cover, active layer thaw, and ground temperature (Kokelj et al., 2013; Lacelle et al., 2010; Lantuit et al., 2012b; Lewkowicz, 1986). In particular, ablation rates of ground ice depend on net radiation and air temperature with high ablation rates measured on warm and sunny days (Lewkowicz, 1986). 40-50 % of the annual ablation and retreat takes place in July. It is even 70-80 % of the total annual ablation taking July and August into consideration (Kerfoot, 1969; Lewkowicz, 1987). There is a high positive correlation between thawing degree days and the retreat rate of the headwall (r= 0.92; Kerfoot, 1969). In the northern hemisphere, retrogressive thaw slumps with south/southeast wards facing headwalls show higher retreat rates of the headwall and it is assumed to be due to insolation with high energy in the afternoon (Lewkowicz, 1987; Séjourné et al., 2015).

Ablation of ice-rich permafrost headwalls has been the focus of prior analyses (e.g. Grom and Pollard, 2008; Lantuit and Pollard, 2005; Lewkowicz, 1986; Lewkowicz, 1987). However, little is known of the sediment-meltwater release from retrogressive thaw slumps. The discharge of retrogressive thaw slumps is not linearly coupled to air temperature and radiation. It is also presumably related to permafrost properties, elevation, slope aspect, mass evacuation of the slump floor, removal of debris on slump exit, and additional water input i.e. snowmelt, rain, and water from the hinterland and polygons (Kerfoot, 1969; Kokelj et al., 2015; Lacelle et al., 2010; Lacelle et al., 2015).

A strong linkage between rainfall events and debris evacuation rate has been suggested by Lacelle et al. (2010). Rain clears the ice-rich permafrost headwall of thawed debris and favours further melt of the ground ice. In the Peel Plateau (Canada), rainfall events provided saturated conditions along the slope, accelerated soil moisture and could lead to reduced soil strength resulting in major mass flows (Kokelj et al., 2015). Snowmelt and active layer thaw in summer also derive additional water that helps to liquefy thawed debris (Kerfoot, 1969).

Retrogressive thaw slumps are a common thermal erosion feature along the Yukon Coast. 73 retrogressive thaw slumps were detected between Shingle Point and Kay Point in 1999 (Wolfe et al., 2001). On Herschel Island 164 retrogressive thaw slumps were counted in 2000 (Lantuit and Pollard, 2005). Each thaw slump releases large quantities of freshwater, sediment (including organic carbon and nutrients), and potentially has a strong impact on the regional ecosystem (Lantuit et al., 2012b). Their total contribution in terms of sediment and organic matter could have substantial impacts for the entire Beaufort Sea (Lantuit and Pollard, 2005; Lantuit et al., 2009).

In recent years an increase in thawing and coastal erosion led to an increasing frequency and extent of retrogressive thaw slumps (Lantuit and Pollard, 2005). Recent publications anticipate an accelerating activity of retrogressive thaw slumps with warming air temperatures and rising precipitation (Kokelj et al., 2015; Lantuit et al., 2012b; Lantz and Kokelj, 2008).

Most of the knowledge gained on retrogressive thaw slumps is based on the relationship between the ablation of the headwall and climatic parameters. This relationship is essential to the melting of the ground ice, but does not necessarily capture all processes taking place in the slump and is also not necessarily a good predictor of discharge from the slump system. It is therefore necessary to understand the exact relationship between climatic and/or morphological parameters and the discharge. This is important in order to understand and quantify the impact the released sediment and organic matter has on the aquatic ecosystem.

2.3. Inputs of Freshwater, Sediment and Carbon into the Canadian Beaufort Sea

The Beaufort Sea is located north of the coastline of the Alaskan North Slope, the Canadian Yukon Territory, and Canadian North West Territories. It is part of the Arctic Ocean and receives large amounts of freshwater, sediment, and organic carbon, from river discharge and coastal erosion (Brown et al., 1997; Figure 2). Several studies have reported on freshwater, sediment, and organic carbon inputs into the Beaufort Sea by river and coastal erosion (Hill et

al., 1991; Lantuit et al., 2012a; Macdonald et al., 1998). These studies, however, have generally omitted the role of retrogressive thaw slumps along the coast. Since these features are associated with fast retreat rates and substantial release of water and sediment, their relevance to the overall sediment and organic matter budget of the Beaufort Sea could be important.

The current knowledge on sediment and organic matter input from rivers and coastal erosion provide large numbers for the Beaufort Sea area. The Mackenzie River is the fourth largest river entering the Arctic Ocean and releases large amounts of suspended sediment and freshwater (Macdonald et al., 1998). It yields approximately $3.3 \cdot 10^{11}$ m^3 a^{-1} of freshwater into the shelf region (Macdonald et al., 1998). The sediment load depends on the discharge and is rising with an increase in discharge. Carson et al. (1998) estimate that up to 99 % of the sediment is supplied from May to October with an annual sediment supply of mainly fine grained sediment in the Mackenzie Delta of $127 \cdot 10^6$ t a^{-1} (Macdonald et al., 1998). The particulate organic carbon content of the Mackenzie River was estimated at 4.8 ± 1.3 % in winter and at 1.4 ± 0.2 % in summer. This amounts to $2.1 \cdot 10^6$ t a^{-1} of particulate organic carbon is released and $1.3 \cdot 10^6$ t a^{-1} of dissolved organic carbon (Macdonald et al., 1998).

The sediment supply of the Canadian Beaufort shelf comes mainly from the Mackenzie River (95 %), but additional sediment is contributed from other rivers along the Yukon coast ($1.45 \cdot 10^6$ t a^{-1}) and from coastal erosion ($5.62 \cdot 10^6$ t a^{-1}) (Hill et al., 1991). Organic carbon input of rivers other than the Mackenzie River into the Canadian Beaufort shelf is assumed to be $0.02 \cdot 10^6$ t a^{-1} with 1.6 % particulate organic carbon (Macdonald et al., 1998). The Canadian Yukon Coast has an erosion rate of 1.12 m a^{-1} (Lantuit et al., 2012a) and on Herschel Island 0.45 m a^{-1} (Lantuit and Pollard, 2008). The input of particulate organic carbon solely from coastal erosion along the Yukon Coast is estimated to be $0.04 \cdot 10^6$ t a^{-1} (Couture, 2010).

These studies divide fluxes into two categories, river fluxes and coastal (i.e. cliff) erosion, excluding the contribution of retrogressive thaw slumps (Rachold et al., 2004). Yet, retrogressive thaw slumps are known to release large quantities of freshwater, sediment, and carbon (Lantuit and Pollard, 2005). Their widespread distribution along the Yukon Coast (Wolfe et al., 2001) and the high amount of water and sediment they presumably release show the importance of including them coastal sediment and organic matter budgets (Lantuit and Pollard, 2005).

3. Study Area

3.1. Regional Setting: Yukon Coast and Herschel Island

The field sites investigated in this thesis are located along the Yukon Coast in northwest Canada. The Yukon Coastal Plain was partially glaciated during the Buckland Glaciation (early Wisconsin) by the Laurentide ice sheet coming from the Mackenzie Valley. The limits of the glaciation are defined by moraines (Figure 4). It is assumed that it did not reach further west than the Firth River (Rampton, 1982). The area is influenced by the retreat of the glacier which left morainic and glacial-fluvial deposits. Ground ice (and often massive ground ice) is ubiquitous in the area and occurs as buried glacier ice, ice wedges, segregated ice, and snowbank ice (Fritz et al., 2011; Fritz et al., 2012; Pollard, 1990). In this area, continuous permafrost has a thickness reaching up to 300 m in depth (Rampton, 1982).

The main focus of the study is Herschel Island. The island is located 3 km offshore the Yukon Coast in the Beaufort Sea (Figure 4). The highest elevation of the island is 185 m (Lantuit and Pollard, 2005) and the vegetation is characterized by lowland tundra (Myers-Smith et al., 2011b; Smith et al., 1989). The island was formed by an overriding glacier as an ice-thrust moraine. Herschel Island consists of marine material from Herschel Basin located 9 km to the southeast (Bouchard, 1974; Mackay, 1959; Rampton, 1982). The disturbed perennially frozen sediments are composed of silty clay with pebbles, silt, sand, and marine Pleistocene fossils, covered by glacial deposits (Fritz et al., 2012; Rampton, 1982). On the island, bodies of ice are very large with respect to other locations in the Arctic. Although exposures rarely exceed 20 m in height, thicker massive ice bodies can be expected because only the upper part is visible in the headwall of retrogressive thaw slumps. 60-70 % of the upper permafrost of the island consists of ground ice (buried glacier ice, segregated ice, and ice wedges; Fritz et al., 2011; Pollard, 1990). The very high ice content observed in these massive ground ice bodies, exceeding 250 % on a gravimetric basis or around 85-90 % by volume (Pollard, 1990), leads to the occurrence of large retrogressive thaw slumps (Lantuit and Pollard, 2005; Mackay, 1959). The total number of retrogressive thaw slumps on Herschel Island increased from 80 to 164 between 1952 and 2000, while coastal erosion, largely responsible for slump initiation, was about 0.45 m a^{-1} from 1970-2000 (Lantuit and Pollard, 2008). Over 2000-2011 erosion rates increased to 0.68 m a^{-1} (Obu et al., 2016a).

Herschel Island is characterized by a - 9.6 °C mean annual air temperature (1999-2005). Mean daily air temperatures are commonly above zero degrees Celsius from late May to mid-October with the warmest months of the year being July (+7.3 °C) and August (+5.9 °C) (Burn and Zhang, 2009). Yearly precipitation data does not exist for Herschel Island. They are estimated to be similar to the closest measured weather station at Shingle Point (254 mm) and Komakuk Beach (161 mm) (Burn and Zhang, 2009). Herschel Island is classified with this low precipitation and low summer temperatures as a polar desert.

Between 2002 and 2007, the mean annual ground temperature on the northeastern tip of Herschel Island, at Collinson Head, was -8.0 °C (Burn and Zhang, 2009). The depth of zero annual amplitude was below 14.5 m. Permafrost temperatures have increased by 1.9 °C - 2.6 °C on Herschel Island since 1899 according to Burn and Zhang (2009). Active layer thickness measured continuously at one location is currently about 55 cm and is 15 to 25 cm greater than in 1985 (Burn and Zhang, 2009). On Herschel Island, snow depth usually ranges between 10 and 26 cm on upland flat tundra terrain with a mean snow depth of 17 cm (Burn and Zhang, 2009). In depressions, it can reach up to 140 cm, highlighting the influence of wind shadow, topography and greater vegetation cover to capture snow and shield soils in winter (Burn and Zhang, 2009; Myers-Smith et al., 2011a).

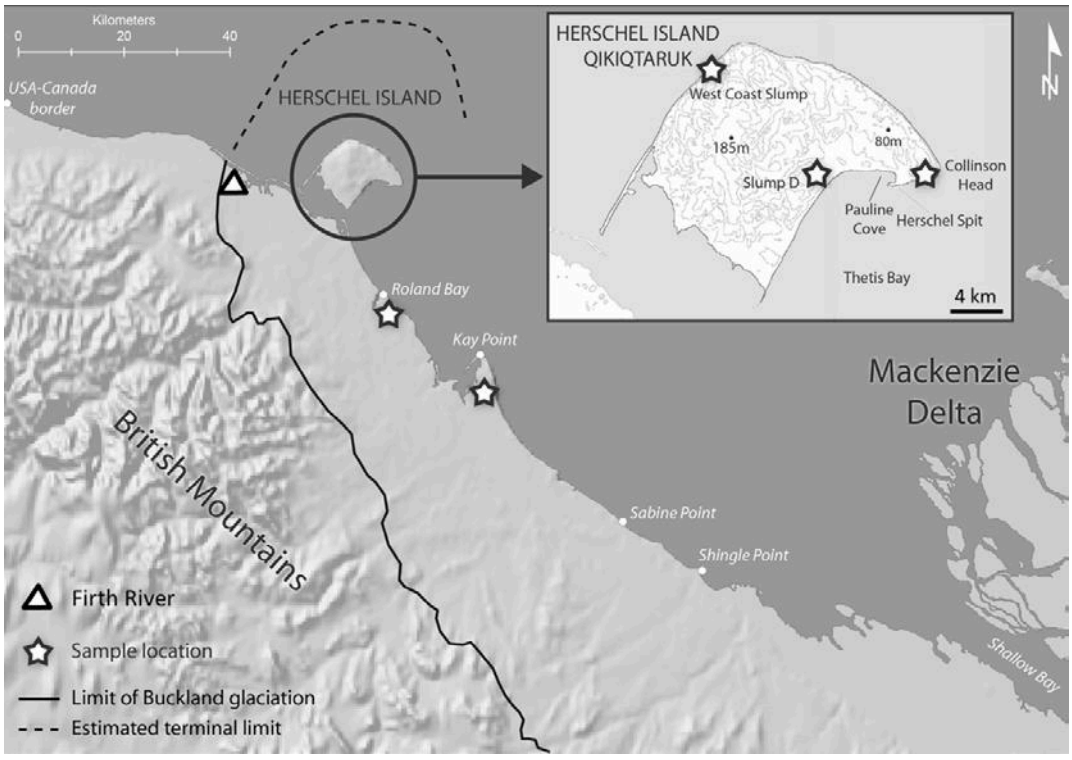

Figure 4. The map shows the limit of the Buckland glaciation coming from the east reaching up to Firth River (black line) and is estimated to have its limit west of Herschel Island (dotted line).The location of study sites are marked, including on Herschel Island Slump D and West Coast slump. Study sites along the Yukon Coast were Collinson Head slump, Roland Bay slump, and Kay Point slump (Map based on Bouchard, 1974 and Smith *et al.*, 1989, adapted from Lantuit *et al.*, 2012; more information in Appendix 8.1).

3.2. Retrogressive Thaw Slumps

Several hundred retrogressive thaw slumps were counted along the Yukon Coast (Lantuit and Pollard, 2008; Wolfe et al., 2001). Slump D is one of the larger along the Yukon Coast has been under observation since 1952. Slump D was chosen as prime field site due to its long observation record and close vicinity to the field camp. However, four additional retrogressive thaw slumps were sampled to put Slump D into perspective. On Herschel Island, the Collinson Head slump was selected due to its close vicinity and walking distance (Appendix 8.1.2). Herschel Island West Coast slump, Roland Bay slump, and Kay Point slump were sampled by helicopter to get information from additional retrogressive thaw slumps along the Yukon Coast (Appendix 8.1.3 - 8.1.5).

Slump D is a retrogressive thaw slump located on Herschel Island. The field site is situated on the southeast coast of the island (N 69.569529, W 139.018061; Figure 4). The retrogressive thaw slump is informally called “Slump D” (following the terminology established by Fritz et al. (2011) and Lantuit et al. (2012b). It is amongst the largest on Herschel Island and can be defined as a “mega slump”, following the definition established by Kokelj et al. (2013). Slump D releases the eroded material directly to the Beaufort Sea through a series of outlets.

In 2012, the highest point of the headwall was located at 52 m above sea level and 470 m inland from the coastline (Figure 5). The total width of the retrogressive thaw slump exceeded 450 m, however the actual total upper headwall length was greater than 1000 m due to the irregular shape of the headwall. The headwall consists of massive ground ice of up to 16 m in height topped with an organic sediment-rich layer of 1-3 m.

Lantuit et al. (2012b) measured retreat rates at Slump D of up to 9 m per year (2004-2006). Lantuit and Pollard (2005) estimated that the retrogressive thaw slump released more than 2 000 000 m^3 of thawed permafrost (i.e. ground ice and enclosed sediment) over 52 years. The retrogressive thaw slump is polycyclic, which is visible in the stabilized and vegetated former headwall cliffs (Figure 5). It shows at least three cycles of activity since 1944 (Lantuit et al., 2012b). At present, it features a slump (lower southern headwall) reactivating in the floor of the main slump (upper northern headwall).

The progression of a retrogressive thaw slump is related to the amount of days above 0 °C, precipitation, solar radiation and higher surface air temperatures in summer (Kokelj et al., 2015; Lacelle et al., 2010; Lantz and Kokelj, 2008; Lewkowicz, 1986, 1987). Discharge at the outlet of the slump is however not necessarily directly coupled to ablation. Other important

factors such as snowbanks, water generated from the hinterland, evaporation, and percolation contribute to modify the water balance and to add or reduce the amount of meltwater and sediment flowing into the outlet. Additionally, the mud pool located at the foot of the headwall occasionally breaches levees and releases massive mudflows, resulting in pulses of meltwater and sediment that are also decoupled from climatic forcing.

Meltwater and sediment released by Slump D are channeled into three outflow channels (Figure 5). The northern outflow channel of Slump D was not considered in this study, because its discharge was insignificantly small in comparison with the two other channels. The southern channel did deliver large quantities of material, mostly through episodic but large mudflows, which hindered the capacity to install any monitoring instruments in the channel. Therefore the lower southern headwall was not under more detailed observation although potentially more sediment-meltwater entered the near shore zone than from the upper northern headwall via the middle outflow channel. The middle outflow channel was well constrained and did not exhibit signs of large mudflow activity. In 2012 and 2013, field inspections showed that around 90 % of the total upper northern headwall area contributed material to the catchment of the middle channel and not to the other ones (Figure 5).

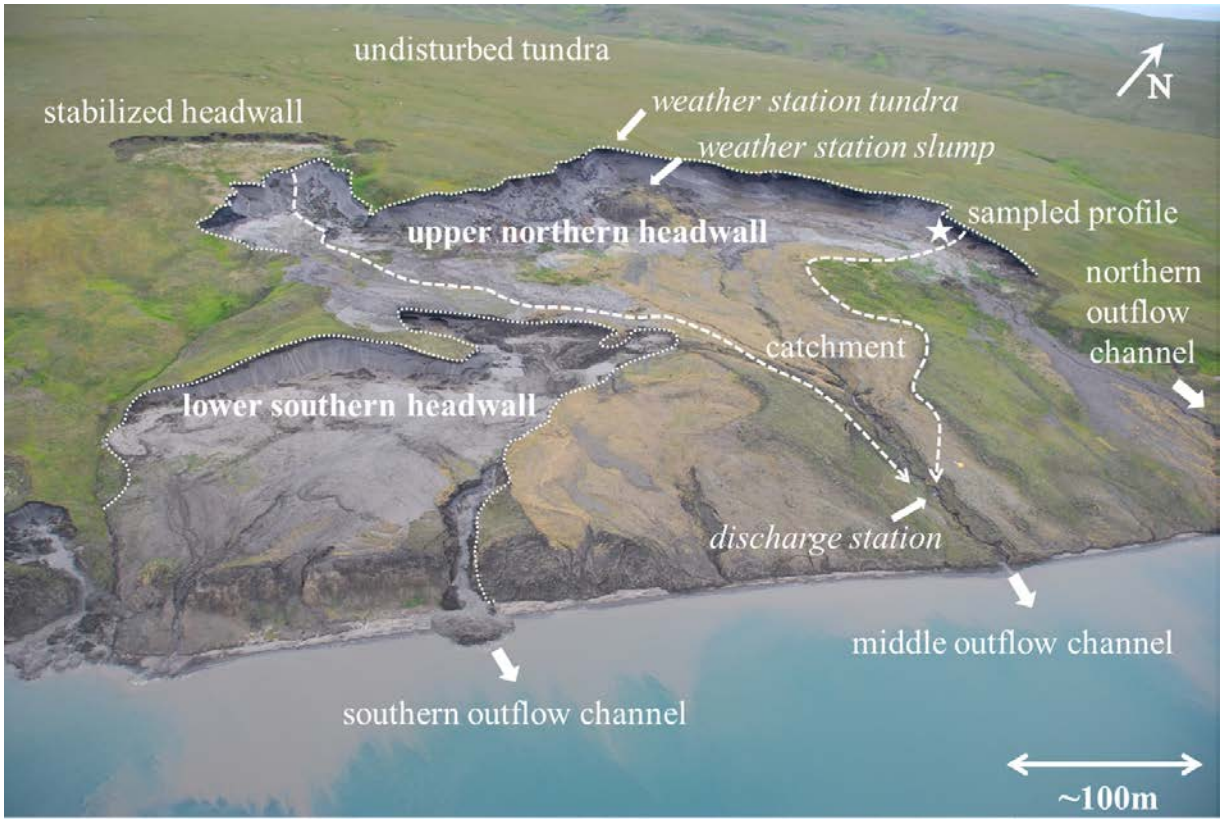

Figure 5. Slump D is over 450 m wide. The upper northern headwall is located about 470 m inland from the shoreline. A second retrogressive thaw slump is reactivating polycyclic in the floor of the main slump. Its headwall is labelled as lower southern headwall. The three channels delivering meltwater and sediments are shown with white arrows.

4. Material and Methods

The study aims at investigating the thawing process and the subsequent release of sediment-meltwater in a retrogressive thaw slump. To put discharge data and sediment-meltwater samples of Slump D into wider perspective, headwall samples were taken from Slump D and from four additional slumps (Appendix 8.1 and 8.2). Samples taken on Herschel Island and along the Yukon Coast were analysed and compared to Slump D to determine if ice-sediment content, organic carbon and nitrogen release of the outflow channel were comparable.

This chapter is divided into two parts: field work and laboratory work. The first part focuses on the measurement of microclimatic and hydrological data as well as water sampling at Slump D, and sampling of headwall profiles of Slump D and four additional slumps. The second part was the data analysis with Excel, Grapher, and multiple regression with R Statistics and laboratory analysis of the samples. All measurements were standardized to UTC-6h (Mountain Daylight Time, Inuvik time) with a shift compared to solar time on Herschel Island (solar minimum at around 03.00 h, UTC-6h).

In total 54 000 minutes of micrometeorological and hydrological data were processed, 163 sediment-meltwater samples were analysed for hydrochemistry and 43 samples for sedimentology. Additionally, 43 headwall samples from Slump D and the four other slumps were analysed sedimentologically (Appendix 8.2).

4.1. Field Work

4.1.1. Terrain Photography

Terrain photographs of Slump D were taken during the summer expeditions from helicopter in 2006 (date unknown), 28 July 2010, 12 August 2012, 29 July 2013 and 11 August 2014 (Appendix 8.3). The images show the slump evolution over the years. Additionally, they illustrate the interannual and intraseasonal variation of remaining snow accumulations along the headwall.

In July 2013, additional photos were taken within the slump to document the retreat of the ice-rich permafrost headwall and melting of snow banks. One photo series was taken of a section of the lower southern headwall of Slump D over 16 days. The other photo series

illustrates the regression of snowbanks along one part of the upper northern headwall over 16 days. Photos were taken with a LEICA, V-LUX 40 camera and a WINGSCAPES Timelapse Camera.

4.1.2. Differential Global Positioning System (DGPS)

In 2011, 2013, and 2014, the headwall was surveyed with Trimble R4 differential global positioning system. Points were measured along the headwall scarp in less than ten meter steps. The device specific accuracy is 0.05 m, but manual accuracy can be up to 1 m, due to inaccessible unstable headwall conditions. The data was displayed with Arc GIS on a Geo Eye satellite image from 2011 with an accuracy of 0.50 m.

4.1.3. Light Detection And Ranging (LiDAR) and Digital Elevation Model (DEM)

Light detection and ranging (LiDAR) scanning of Slump D took place on 22 July 2013 and was performed by the research aircraft Polar 5 during the AIRMETH campaign (Kohnert et al., 2014). LiDAR data was interpolated to a Digital Elevation Model (DEM) with horizontal resolution of 1 m and vertical resolution of 15 cm (Obu et al., 2016a). The DEM was used to measure the original headwall length, average headwall angle, headwall surface area, and the area of the catchment (including the undisturbed tundra on top of the slump and the slump floor) running into the outflow channel and recorded at the cut-throat flume. The information was used as basic data for further calculations related to the thawing headwall and rainfall events in this thesis.

4.1.4. Micrometeorology

Long-term records:

Weather data on Herschel Island was recorded by an Environment Canada weather station, situated on Herschel Spit, 4 km east of Slump D. The station is labelled station number 71501 in the World Meteorological Organization (WMO) network. Meteorological data has been manually collected on the island from 1899-1905 and automatically since 1994. Surface air temperature, wind direction, wind speed, and precipitation is measured hourly with interruptions due to device failure. The station has complete surface air temperature records for the years 1900-1905, 1917, 1995-1997, 2002-2004, and since 2009.

Field measurements 2012/2013:

In August 2012 and July 2013, two weather stations and a cut-throat flume were installed at Slump D to analyse and quantify the relationship between micrometeorological drivers and the release of thawed permafrost material at the slump outlet. In 2012, two weather stations were set up from the 31st of July until the 18th of August to provide input data and test microclimatic differences between the inner and the outer part of the slump. One weather station (weather station tundra) was situated above the slump on the undisturbed tundra about 50 m off the eroding headwall. An additional weather station (weather station slump), within the slump floor, was erected in closest possible vicinity (15 m) to the headwall (Figure 5). In 2013, only one weather station was installed; between 7th and 15th of July on the undisturbed tundra surface, and between 15th and 25th of July moved to the location within the retrogressive thaw slump, due to repeated disturbance of the instruments from wildlife.

Snowbanks remaining from winter snowdrift within the retrogressive thaw slump along the bottom of the headwall protected the permafrost from thawing. They were visually inspected throughout both field seasons and recorded through terrain photography (Section 5.1.1).

The two field weather stations collected air temperature, incoming solar radiation and wind speed data 2 m above ground level. Precipitation data was collected 1 m above the ground, 2 m away from the weather station to avoid interfering wind shadow. Temperature was measured with an external sensor (BTF11/002 TSic 506; ± 0.1 °C accuracy); precipitation was collected with a tipping bucket rain gauge (Young Model 52203; 0.1 mm per tip; accuracy ± 2 %). Incoming solar radiation was detected by UTK – EcoSens (11.6.6133.0051;

error < 10 %) and wind speed by Thies CLIMA (4.3519.00.173; ± 0.5 m s-1 accuracy). All weather data was recorded every 60 seconds on a logger (LogTrans6-GPRS) and uploaded with the program SENSOlog v5.1.2.1.

4.1.5. Discharge Measurement

The upper northern headwall released its thawed sediment-meltwater discharge into the middle outflow channel. Sediment-meltwater from the upper northern headwall output via the middle outflow channel was passed through a cut-throat flume (Figure 6; throat width W = 0.2 m, flume length L = 0.7 m and height 0.5 m). The cutthroat flume was constructed after Skogerboe et al. (1972) using standard sizes:

$$B = W + \frac{L}{4.5}$$

L	length (=0.70 m)	2.30	[feet]
W	throat width (=0.20 m)	0.66	[feet]
B	width of mouth; B=W+L/4.5(=0.355 m)	1.16	[feet]

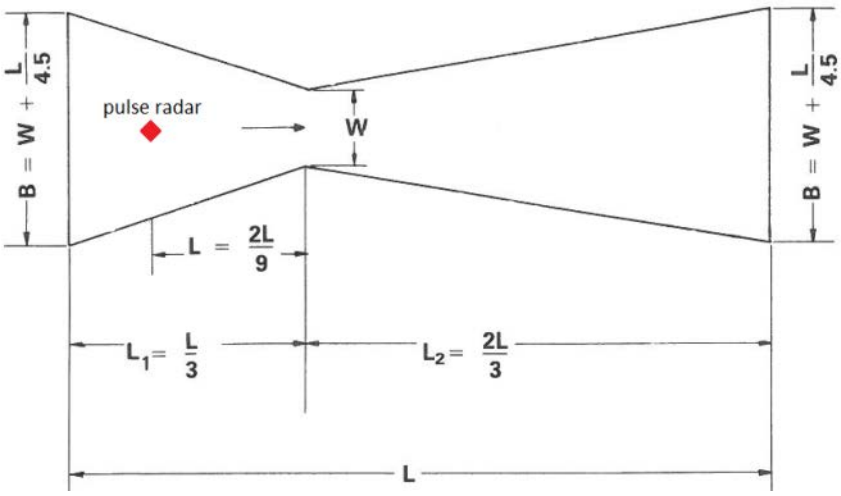

Figure 6. Cutthroat flume construction manual after Skogerboe et al. (1972). The length of the flume installed in slump D was L= 0.70 m and had a throat width of W = 0.20 m and a mouth width B = 0.355 m. The pulse radar sensor was mounted in the entrance of the flume (red square).

The cut throat flume was installed at the very end of the channel, less than 50 m from the shoreline (Figure 5 and Figure 7). The height of the sediment-meltwater stream surface running through the cut-throat flume (upstream flow depth-h_u) was measured by a pulse radar (VEGAPULS WL61; ± 2 mm accuracy) at an interval of 60 seconds. Data was logged with the LogTrans6-GPRS and downloaded with the program SENSOlog v5.1.2.1.

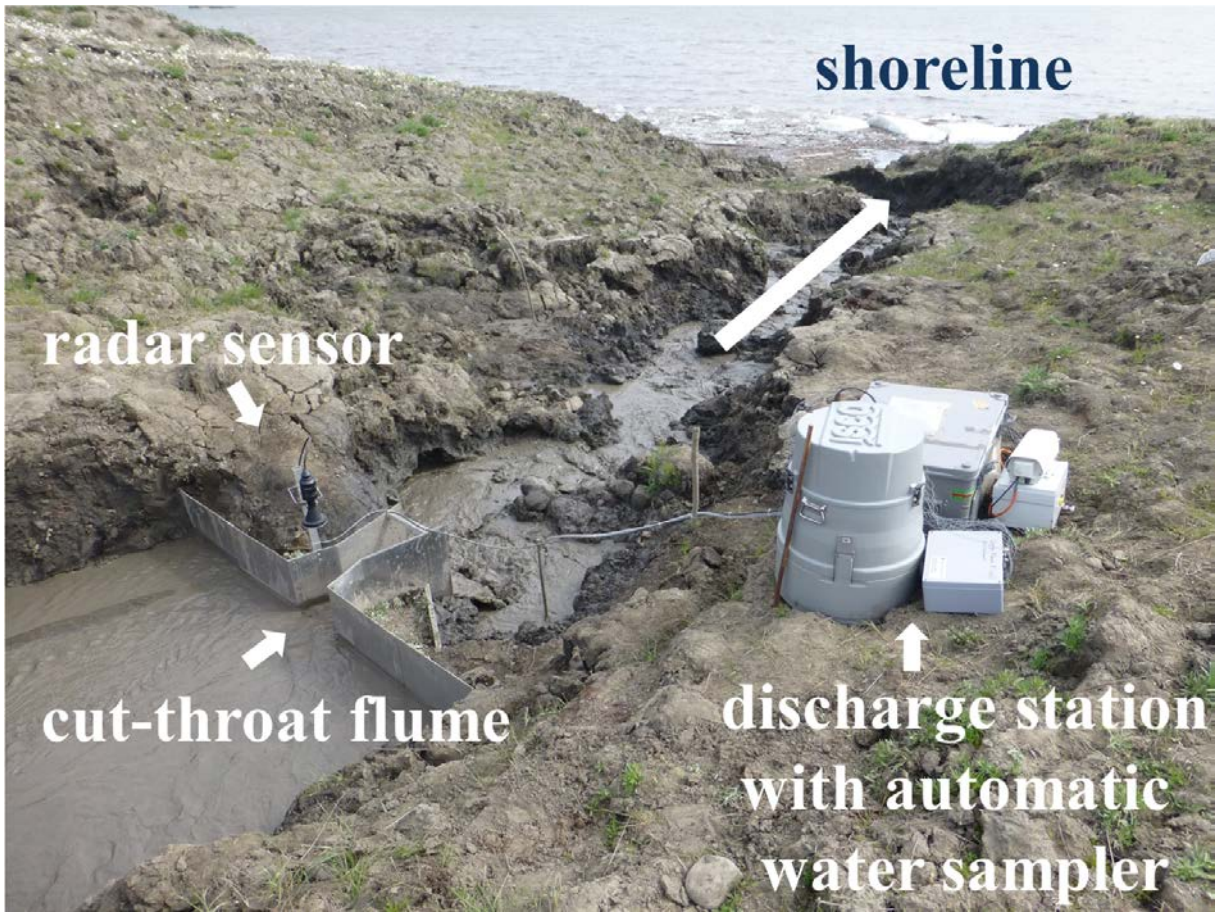

Figure 7. Discharge station in the middle outflow channel installed 50 m inland from the shoreline. The pulse radar sensor detected fluctuations in sediment-meltwater height in the cut-throat flume and was used to calculate the total volume of sediment-meltwater released into the ocean. The automatic water sampler sucked sediment-water after passing the cut-throat flume into sample bottles.

Discharge data was recorded in the periods between the 30th of July and 16th of August 2012 (18 days), and the 7th and 25th of July 2013 (19 days). The discrepancy between the two periods was part of the experiment setup, the objective being to capture thawing and discharge dynamics in the early and late thawing season. The equation was used in cubic feet per second and later converted to cubic meter per second. Due to the 60 seconds interval, discharge was multiplied by 60 to cubic meter per minute after Skogerboe et al. (1972; Figure 8):

$$Q = \frac{c_s(h_u - h_d)^{n_f}}{\left(-\log \frac{h_d}{h_u}\right)^{n_s}} = \frac{c_s(h_u - (h_u * S_t))^{n_f}}{(-\log S_t)^{n_s}}$$

and

$$c_s = K_s * W^{1.025}$$

Q	discharge		$[m^3 s^{-1}]$
c_s	submerged flow coefficient	1.79	[feet]
h_u	upstream flow depth		[feet]
h_d	downstream flow depth = h_u*S_t		[feet]
n_f	free flow exponent	1.93	
n_s	submerged flow exponent	1.54	
S_t	transition submergence (0.635)	63.5	[%]
K_s	submerged flow flume length coefficient	2.75	

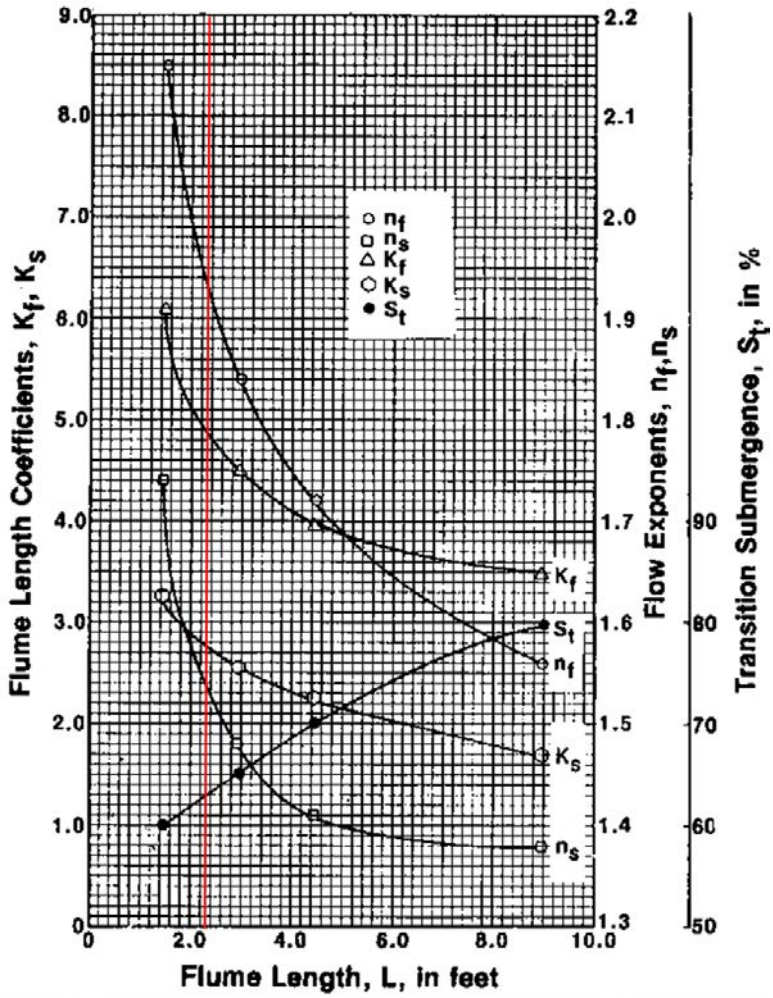

Figure 8. The nomogram describes the correlation of various coefficients in the Skogerboe equation. The red line shows the accurate coefficient values for the flume length of 2.3 feet as it was used in Slump D. The specific variables regarding the flume length (L=2.3 feet, red line) are: free flow exponent (n_f = 1.93), submerged flow exponent (n_s = 1.54), transition submergence (S_t = 63.5 %) and submerged flow flume length coefficient (K_s = 2.75); After Walker and Skogerboe (1987).

4.1.6. Multiple Regression-Statistical Relationships between Micrometeorological Variables and Discharge

Discharge was regressed against climate data (incoming solar radiation, air temperature, and wind speed) to analyse the correlation between discharge dynamics and climatic forcing. On the basis of the fit of the multiple regression, empirical values of discharge were calculated and projected into the future using climate change scenarios. The calculation was performed by the statistic program R (Version Rx64 2.15.0).

4.1.7. Sampling

Sediment-meltwater of the upper northern headwall of Slump D was sampled with an automatic water sampler up to once per hour in the middle outflow just downstream from the cut-throat flume (50 m before entering the near shore zone). In total, 82 sediment-meltwater samples were taken in July 2013 and 81 sediment-meltwater samples in August 2012. Samples were taken at 03:00, 09:00, 15:00, and 21:00 in order to capture the minimum incoming solar radiation time around 03:00 and the maximum incoming solar radiation around 15:00. Due to sedimentation in the outflow channel obstructing the sampling hose, gaps occurred in the sampling cycle. In August 2012, two denser sampling periods of 24 hours were conducted with an attempt at sampling once every hour. In July 2013, one 24-hour sampling period was performed with hourly sampling. In both years, gaps in the sampling occurred due to device failure. Samples were taken with the automatic water sampler ISCO 3700 Full-size Portable Sampler and stored in its tank for up to 4 days in 1 L polypropylene bottles. The automatic water sampler ISCO 3700 sampled with a strainer of 5 mm sieve. Samples were taken out of the tank as often as weather conditions allowed us to go to the field site. The samples were shaken upside down and decanted immediately in 250 ml high density polyethylene (HDPE) bottles. In addition, sample bottles were filled just with distilled water, to test for contamination from the sampling bottles throughout the process. All 163 sediment-meltwater samples went through hydrochemical analyses (water content, electrical conductivity, pH, dissolved (in-) organic carbon). In total, 43 sedimentological analyses were conducted to determine sediment content, grain size distribution, total carbon, total organic carbon, total nitrogen and δ13C.

All 163 outflow samples (82 in July 2013 and 81 in August 2012) were frozen at about -6°C in the ice house on Herschel Island (four meter deep subterranean chamber built in permafrost). In Inuvik, samples were stored at the Aurora Research Institute at -20 °C and transported frozen in thermally isolated boxes to the laboratory of the Alfred Wegener Institute in Potsdam, Germany. There they were stored at -20°C in the institute freezer until laboratory analyses started.

4.2. Laboratory Analyses

All samples were analysed in the laboratory of the Alfred Wegener Institute Helmholtz Centre for Polar and Marine Research in Potsdam except for the δ13C measurements. The latter analysis was performed at the German Research Centre of Geosciences (GFZ) in Potsdam, German.

All 163 sediment-meltwater samples of Slump D were analysed hydrochemically and quantification of the sediment content was conducted (Figure 9). Sedimentological analyses were conducted only on selected samples. In July 2013, of the 82 samples, 78 samples were analysed for sedimentology to see if there were any intra- and inter-diurnal variations. For August 2012, 81 sediment-meltwater samples were analysed for sedimentology to see if there were any additional seasonal variations.

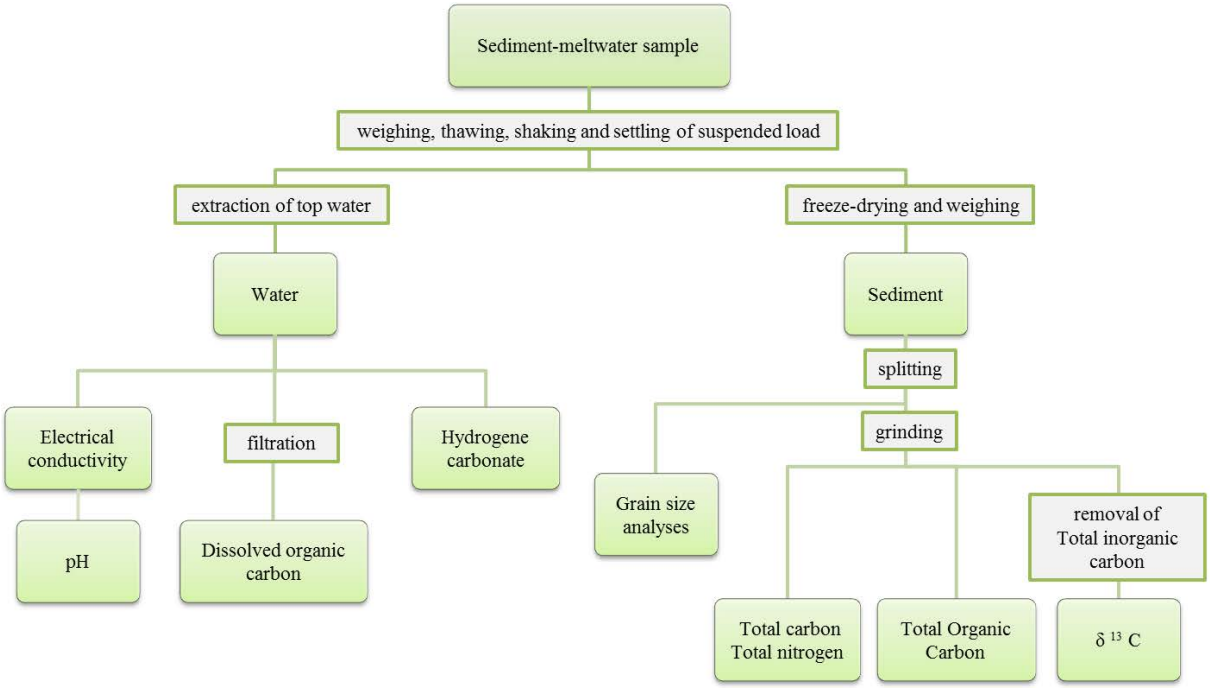

Figure 9. Flow diagram showing the work flow for the laboratory analysis performed on the sediment-meltwater samples. Supernatant water was analysed for electrical conductivity, pH, dissolved organic carbon and hydrogen carbonate. The rest of the sample was freeze-dried and analysed for grain size, total nitrogen, total carbon, total organic carbon and $\delta^{13}C$. All 163 sediment-meltwater samples from the outflow channel were analysed for hydrochemistry and 43 of them underwent additional sedimentological analyses.

4.2.1. Sedimentological Analyses

4.2.1.1. Sediment, Water and Volumetric Ice Content

The 163 sediment-meltwater samples were weighed in the 250 ml HDPE bottles. After thawing, shaking and settling of the suspended material, water was extracted for hydrochemical analyses. The remaining part of the sample with the settled sediment was freeze-dried (Zirbus Technology, Sublimator 3-4-5) and afterwards weighed again. The known bottle weight was subtracted from the total weight and resulted in the sediment weight per 250 ml and multiplied four times to sediment weight (g l^{-1}). The sediment weight was divided by the assumed density of quartzite 2.65 g cm^{-1} to sediment volume (ml l^{-1}). This allowed estimating the water volume (ml l^{-1}) in the sediment-meltwater sample.

4.2.1.2. Grain Size

Grain size distribution provides information about environmental and energetic conditions of the sediment during transportation and deposition and is one of the analyses in this study.

The samples were prepared for the analyses by filling 100 ml 3 % hydrogen peroxide (H_2O_2) to 5-12 g sample in a 400 ml beaker. Organic components were removed by adding 10 ml 35 % hydrogen peroxide three times a week and shaking the sample continuously for about 5 weeks on a platform shaker (New Brunswick Scientific, Innova 2300 platform shaker). During this period, pH was controlled and kept stable between 6-8 by adding acetic acid (CH_3COOH) or ammonia (NH_3*H2O).

Afterwards the organic free samples were diluted three times, washed-off and centrifuged to neutral pH values (10 minutes Heraeus Cryofuge 8500i Centrifuge, Thermo Scientific with 5050 rotation per minute). In the next step samples were further centrifuged to reduce their volume from about 200 ml to fit in 65 ml centrifuge tubes. Samples were centrifuged two to five times to achieve this (15 minutes Heraeus, Multifuge 3s with 4000 rotations per minute) and afterwards freeze-dried (Zirbus Technology, Sublimator 3-4-5) and homogenized.

In the next step, 2 g of the sample were added to 1 liter 0.3 ppm ammonia solution (NH3) to avoid algal formation and 1 g dispersing agent (Na4P2O7 · 10 H2O) to prevent conglomeration for twelve hours and were continuously shaken (Gerhard, laboshake). Finally, the samples were filled into a rotary sample divider (laborette 27) with a sieve size of 1 mm

and split into eight homogenous subsamples. Two subsamples of each sample were analysed and averaged with a laser particle sizer (Beckmann, Colder LS 200). Grain size distribution < 1 mm was measured and analysed with the GRADISTAT software (Blott and Pye, 2001; Table 1). The grain size was defined after Blott and Pye (2001) and plotted in a triangle after Shepard (1954).

Grain size		Descriptive terminology (Blott and Pye, 2001)	
phi	mm/µm		
< -11	< 2048 mm	Very large	
< -10	< 1024	Large	
< -9	< 512	Medium	Boulders
< -8	< 256	Small	
< -7	< 128	Very small	
< -6	< 64	Very coarse	
< -5	< 32	Coarse	
< -4	< 16	Medium	Gravel
< -3	< 8	Fine	
< -2	< 4	Very fine	
< -1	< 2	Very coarse	
< 0	< 1	Coarse	
< 1	< 500 µm	Medium	Sand
< 2	< 250	Fine	
< 3	< 125	Very fine	
< 4	< 63	Very coarse	
< 5	< 31	Coarse	
< 6	< 16	Medium	Silt
< 7	< 8	Fine	
< 8	< 4	Very fine	
< 9	< 2		Clay

Table 1. The grain size distribution with descriptive terminology defined by Blott and Pye (2001). Grain size was described by phi and mm/µm with the descriptive terminology of clay, silt, gravel and boulders subdivided from very fine to very coarse.

4.2.1.3. Total Organic Carbon, Total Inorganic Carbon, and Total Nitrogen

Total carbon, total organic carbon and total nitrogen provide information about organic matter components, their sources, and degradation (Meyers, 1994). Samples were analysed to determine their geochemical properties. From the freeze dried main samples, 12.5 ml subsamples were taken. They were finely ground and homogenized with a planetary mill (Fritsch, Pulverisette 5 classic line) to include coarser organic fragments.

For total carbon and total nitrogen analyses, two sets of eight ml of each sample was weighed. They were packed in tin capsules with tungsten trioxide (WO3) to accelerate the combustion at 1150 °C. Total carbon and total nitrogen were measured with an elemental analyser (Elementar, Vario EL III).

For total organic carbon analyses, the weight of samples taken depended on the total carbon content and was for the sample series between 65 and 100 mg. The samples were duplicated and filled in iron crucible and burnt at 850 °C. Total organic carbon samples were determined with an elemental analyser (Elementar, Vario MAX). Total organic carbon amounts were later estimated to be equivalent to the particular organic carbon amounts, due to the low dissolved organic carbon values (see results chapter 5.2).

The amount of total inorganic carbon of a sample was quantified by subtracting the total organic carbon amount from the total carbon amount.

In the measurement series, blank capsules and reference samples were analysed for background detection, calibration, and control standards every 15 samples (thirtieth capsule). All values are given in weight percent (wt %, equivalent to g 100g-1) with detection limit > 0.1 wt % and standard deviations of < 5 % between each repeated determination.

4.2.1.4. $\delta^{13}C$ and TOC/TN Ratio

$\delta^{13}C$ values can provide information about the origin of organic matter. Photosynthetic plants prefer to incorporate the lighter atmospheric carbon ^{12}C. Consequently all plants have relatively less ^{13}C than the atmosphere. The $\delta^{13}C$ value expresses the difference between the $^{13}C/^{12}C$ ratio of the sample relative to the standard which is carbon dioxide from Pee Dee belemnite in per mil (Craig, 1957; Bender, 1970).

$$\delta^{13}C\ [‰] = \frac{(\frac{^{13}C}{^{12}C}\,\text{sample} - \frac{^{13}C}{^{12}C}\,\text{standard})}{\frac{^{13}C}{^{12}C}\,\text{standard}} * 1000$$

The more negative the value $\delta^{13}C$ is, the lighter the sample as it contains less ^{13}C than the standard (Craig, 1953). Photosynthetic plants produced from atmospheric CO_2 using the C_3

pathway have lower $\delta^{13}C$ values (~-27 ‰) whereas others using the C_4 pathway of ~-14 ‰ (VPDB; Meyers, 1994). $\delta^{13}C$ values from organic matter cannot distinguish between C_3 land plants and algae, but between C_4 plants with heavier isotopic values (Meyers and Ishiwatari, 1995).

The TOC/TN ratio and the isotopic $\delta^{13}C$ composition can help to distinguish the origin of organic matter and hence the environmental condition during that period of growth (Meyers, 1994; Figure 10). The TOC/TN ratio is the quotient of total organic carbon (wt %) and total nitrogen (wt %). It is utilized to differ organic matter between freshwater and marine algae (4-10) and continental plants (<20).

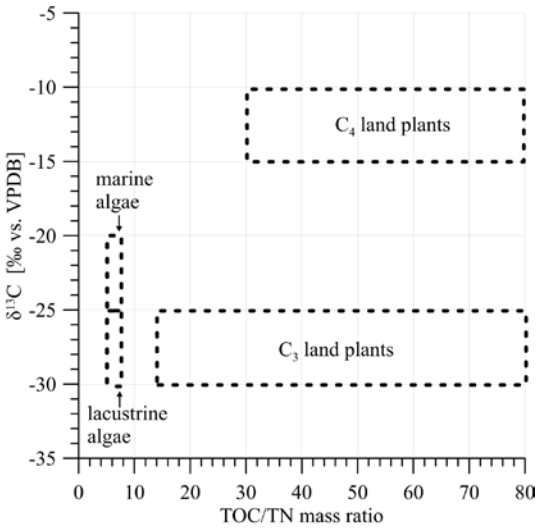

Figure 10. The diagram shows the total organic carbon and total nitrogen ratio (TOC/TN) compared to δ13C [‰ vs. VPDB]. The ratio values can indicate the origin of samples as marine and lacustrine algae, as well as C_3 and C_4 land plants. The classification is modified to TOC/TN mass ratio (modified after TOC/TN atomic ratio Meyers (1994) and (2003)).

Sediment samples were analysed for $\delta^{13}C$ stable isotopes and C/N ratio. Samples for $\delta^{13}C$ analyses were prepared by using 0.2- 2.0 g of the grinded and homogenized samples. They were cooked at 97 °C for three hours with 20 ml hydrochloric acid (w = 4 %) to remove carbonate. The samples were washed three times (chlorine free), filtered, dried at 50 °C, and homogenized with a pestle and mortar. The prepared $\delta^{13}C$ samples were packed in tin capsules with a sample weight calculated using the following equation:

$$\text{sample [g]} = \frac{20}{\text{TOC}}$$

Stable carbon isotopes of total organic carbon ($\delta^{13}C$) were analysed with a mass spectrometer (Delta Plus XL, Finnigan) combined with an elemental analyser (Carlo-Erba NC2500). For

the analyses, excess oxygen was used to burn the samples and combustion gases were identified in the isotope ratio mass spectrometer. The stable isotope data was expressed in delta per mil notation (δ, ‰) relative to the Vienna Pee Dee Belemnite (VPDB) standard. The analysis was calibrated with a certified elemental standard (Urea), isotopic standards (USGS24, CH-7) and a soil reference sample (Boden 2). The analytical precision was better than 0.2 ‰ for $\delta^{13}C$ relative to VPDB. Blank and reference samples were measured at the beginning and the end of the sample series, and after every eights sediment sample to control the analyses.

4.2.2. Hydrochemical Analyses

All sample bottles were weighed empty, and reweighed before and after freeze-dry to quantify the sediment and moisture content. Hydrochemical analyses were performed after thawing the samples. The samples were shaken to avoid bonding. Due to the high sediment load and high clay content, filtration could not be performed immediately and samples were left overnight to wait for the suspended matter to settle before water was extracted. Hydrochemical analyses were performed on all 163 sediment-meltwatere samples from August 2012 and July 2012.

4.2.2.1. Electrical Conductivity

Electrical conductivity is defined as a measure of the ability of a solution to conduct an electrical current. The current is carried by cations and anions and an increase in concentration of ions leads to higher values (WTW, 2003). Electrical conductivity is temperature dependent. A reference temperature of 25°C is used in this study. Measurements were done on 8 ml sample solution and afterwards used for pH measurements. All 163 unfiltered samples were measured with a MulitLab 540, WTW and recorded in µS/cm.

4.2.2.2. pH Value

The pH value is defined as the negative logarithm of the hydrogen ion activity in a solution. It indicates the acidity or alkalinity in a range between 0 and 14 in a sample (Covington et al., 1985). The pH values were determined with a MultiLab 540, WTW.

4.2.2.3. Dissolved Organic Carbon

Dissolved organic carbon is highly bioavailable and an important element for the sensitive Arctic ecosystem and the regional and global carbon cycle (Fritz et al., 2015). Dissolved organic carbon content was measured on sediment-meltwater samples from the flume at the outlet of Slump D.

163 subsamples were taken from the sediment-meltwater samples after the suspended material settled and water from the top could be extracted. The subsamples were prepared by using a gum-free syringe with a pore size of 0.7 µm glass fiber filter (Whatman). The first 20 ml of each filtration were dismissed to prevent dissolved organic carbon contamination from the filter. The following 20 ml were filled into headspace glasses preserved to pH < 2 with 20 µl 30 % suprapur hydrochloric acid (HCl-) to avoid bacterial activity and closed with crimp caps with Butyl-Polytetrafluoroethylene-septum. These prepared subsamples were stored maximum of two weeks at 4 °C in the fridge. Quality control standards (LGC-Promochem: HURON-98, Perade-20, US-QC-Standard I and II) and blanks (ultrapure water) were used after each tenth measurement of samples to validate the analytical measurements. Two empty 250 ml high density polyethylene bottles (HDPE) and two 1 L polypropylene bottles from the automatic water sampler followed the same process of transport, freezing and thawing until the return at the AWI laboratory. They were filled with ultrapure water in Potsdam. They were analysed as blanks to exclude potential release of organic carbon compounds from the plastic bottles. The Shimadzu, TOC-VCPH total organic analyser measured the dissolved organic carbon concentration with the non-purgeable-organic-carbon-method at high-temperature of 680 °C. All samples were automatically analysed as single runs with 3-5 internal measurements. Certified reference standards showed recovery and measurement error of ± 10 % of the measured value. A detection limit was determined of 0.5 mg l-1 of the instrument and eventually contaminations of plastic bottle and surrounding conditions defined by blank measurement.

4.2.2.4. Hydrogen Carbonate and Dissolved Inorganic Carbon

Titration is a method to measure the amount of hydrogen carbonate (HCO_3^-) in an aquatic solution. The hydrogen carbonate concentration in an aquatic solution depends on the pH value. Total carbonate dioxide occur as carbonic acid (H_2CO_3), hydrogen carbonate (HCO_3^-) and/or carbonate ions (CO_3^{2-}). Hydrogen carbonate measurements can be carried out for

samples with a pH value between 4.3 and 8.5 (at 25°C). In the solution at pH = 4.3 is almost solely carbonic acid (> 99.15 %). With an increase of pH, it is transformed to hydrogen carbonate. At a pH = 8.5, the hydrogen carbonate is 97.38 %. With a rise in pH-value, hydrogen carbonates decrease and transform to carbonate ions (Wisotzky, 2011).

In this study, hydrogen carbonate concentration was determined by titrating 2 ml subsamples with 0.01 M hydrochloric acid until all hydrogen carbonate were transferred into carbonic acid (H_2CO_3) at a pH = 4.3 using 794 Basic Titrino Metrohm. By knowing the starting pH value and the amount of hydrochloric acid added, it was possible to calculate the amount of hydrogen carbonate in the sample. Control standards were used in the beginning and end of sampling series and after each twentieth sample of 2ml of 500, 1000, 2000 µmol l^{-1} hydrogen carbonate. The analytical error was ± 10 %. The calculation from µmol l^{-1} to mg l^{-1} was calculated with the molecular weight of hydrogen carbonate (61 g mol^{-1}) by:

$$\mu\text{mol}\,\text{l}^{-1} * \frac{61}{1000} = \text{mg}\,\text{l}^{-1}$$

The molecular weight of carbon (12 g mol^{-1}) and hydrogen carbonate (61 g mol^{-1}) was used to quantify the dissolved inorganic carbon (DIC) concentration by using the molecular ratio of 12/61 (Fritz et al., 2015):

$$\text{HCO}_3^- \,[\text{mg}\,\text{l}^{-1}] * \frac{12}{61} = \text{DIC}\,[\text{mg}\,\text{l}^{-1}]$$

4.3. Fluxes of Sediment and (In-) Organic Matter

The fluxes of the total volume of sediment-meltwater released by Slump D were quantified for the 18 day field season in July 2013 and the 18 day field season in August 2012. The amounts were comprised of sediment, including total (in-) organic carbon and total nitrogen; meltwater and dissolved (in-) organic carbon.

$$\text{Total amount of organic carbon realeased via both field seasons} = \text{Average total organic carbon} \times \text{total sediment meltwater volume}$$

5. Results

The data used in this thesis was collected in August 2012 and July 2013. However, this chapter describes the seasonal progression rather than remaining to a strictly chronological order. First the July 2013 field season is covered, then the August 2012 season.

5.1. Field Work

5.1.1. Terrain Photography

On Herschel Island annual precipitation is estimated to be between 161 and 254 mm with about half of the amount falling as snow between October and May (Burn and Zhang, 2009). Snow accumulates in average to a height of 17 cm (Burn and Zhang, 2009). However, this varies strongly. A photo of Slump D taken on 26 April 2016 shows snow drift with bare soil on top of the tundra and within the slump floor, but with snow accumulations of several meter thickness along the headwall (Figure 11).

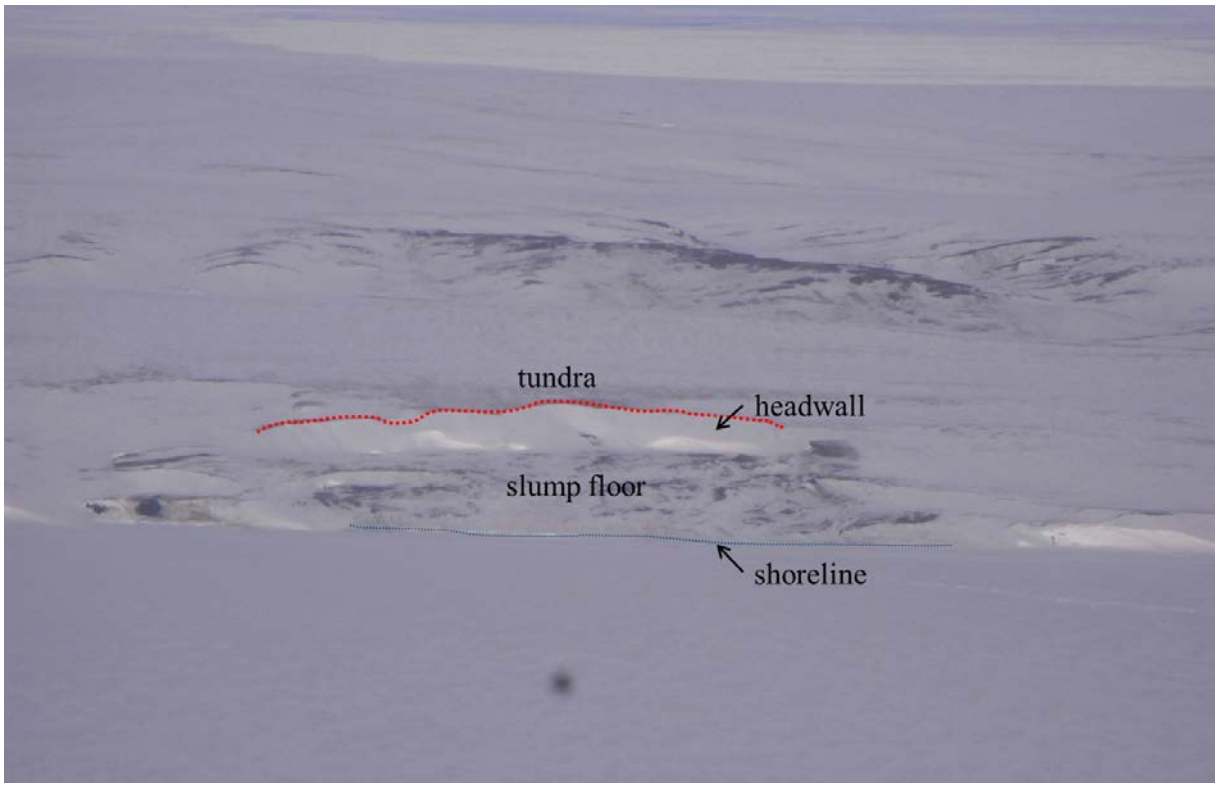

Figure 11. Aerial oblique photo taken of Slump D on 26 April 2009. It shows strong variations of snow accumulation with bare soil on the tundra and in the slump floor and large snow accumulation of several meter thickness along the headwall.

Snowbanks along the headwall are reducing throughout the thawing season. In the beginning of the thawing season they shield the ice-rich permafrost headwall from direct sunlight and warm surface air temperatures, thus delaying the thawing of the headwall (Balser et al., 2014). The retreat of snowbanks can vary considerably between years. For example, on 12 August 2012 just a few snow patches were left in the middle section of the upper headwall (Figure 12), while in contrast, on 19 August 2013, at least 25 % of the headwall was still shielded by snow and debris (Figure 13).

Figure 12. Aerial oblique photo of Slump D on 12 August 2012. Just a few snow patches (outlined in white) were left at the bottom of the upper northern headwall, highlighting the negligible contribution of snow to discharge in late summer.

Figure 13. Aerial oblique photo of Slump D taken, on 19 August 2013 (i.e. one year later than Figure 11). The remaining snow protected about 25 % of the upper northern headwall from thawing. There was more snow remaining than at the same time a year before (Figure 12). This image was taken after the field season, which ended on 25 July 2013 (photo credit: Donald Gibson-Canadian Coast Guard).

Snowmelt can occur at a fast pace, within just a matter of days. On 5 July 2013 snowbanks covered about 90 % of the headwall (Figure 14), with just the top few meters of the upper headwall being free of snow where the headwall was vertical or overhanging. Two days later, on 7 July 2013, snowbanks covered only 60-70 % of the upper northern headwall (Figure 15). The middle and right sides of the headwall were not fully exposed, as the surface of the snowbank was partially covered by dry organic material. This material consisted of a layer of grass that was blown with the snow by strong winds in winter, and which remained on top of the snowbanks during much of the thawing season (Figure 16).

Figure 14. Aerial oblique photo taken of Slump D on 5 July 2013. Snowbanks covered more than 90 % of the headwall and only the top few meters of the headwall were snow free, where the headwall was vertical or overhanging. Thawed material started to erode from the top of the headwall on top of the snowbanks. The white frame indicates the picture section for comparison with a similar photo taken two days later on 7 July 2013 (Figure 15).

Figure 15. Photo of Slump D on 7 July 2013. The headwall was up to 16 m high and 60-70 % covered by snow. The comparison with Figure 14 highlights the rapid melting of snow cover within just two days. In the mid-section of the headwall and on the far right, snow was covered partly by debris.

As the thawing season proceeded, snowbanks were covered by dry organic material such as grass or thick muddy debris. The mud originates from the already-exposed top of the ice-rich permafrost headwall and slides down over the remaining snowbank (Figure 17). Exposed thawing ice-rich permafrost liquefies the lower headwall and thus can induce new debris flows (Lewkowicz, 1985). Thick debris layers can shield the snow and ice underneath it from radiation and therefore decrease thawing, while thin debris cover can lead to continuous ablation underneath it and thus increase thawing considerably (Lewkowicz, 1985).

Snow banks remained longer on gentle slopes than on steeper sections (Figure 13). On the flat-angled headwall, the sliding-down debris partially sedimented on top of the snow or formed erosion gullies through the snowbank (Figure 14 and Figure 17). On steep cliffs erosion was faster and sliding-down debris eroded directly into the mud pool (Figure 13). The centre of the upper headwall was northeast facing and had the longest remaining snowbank (Figure 12 and Figure 13).

Figure 16. Photo of the front of the Slump D headwall (top left, person for scale). A layer of grass lies on top of the snowbank. The grass was blown, together with snow, by wind from the open tundra to the wind shadow of the headwall, where it accumulated. The layer of grass remained on top of the melting snow for the entire field season. Mud flows coming from the thawing, ice-poor permafrost at the very top of the headwall were funnelled into gullies or flowed freely over the snowbank.

Figure 17. Two images of the headwall taken on 13 and 23 July 2013 with an automatic timelapse camera (orange-clothed person for scale). Debris from the upper headwall was deposited on top of the snowbanks, which both protect the ice-rich permafrost headwall from thawing.

In addition to snow bank observations, terrain photography was used to visualize the erosion rates of exposed permafrost. Repeated photography of single headwall sections indicated rapid retreat rates (Figure 18). Figure 17 A and B focus on the same isolated permafrost headwall section but from two different directions. This permafrost headwall, exposed like an isolated island, had a maximum diameter of about 30 m and a height of about 8 m. The images from 7 and 23 July 2013 were compared and show a complete disappearance of this ice-rich permafrost island within 16 days.

Figure 17 C shows two pictures of the middle outflow channel taken on 9 and 25 July 2013 (16 days). The sediment-meltwater channel cut an erosion front in the slump floor that grew about 6 m landwards.

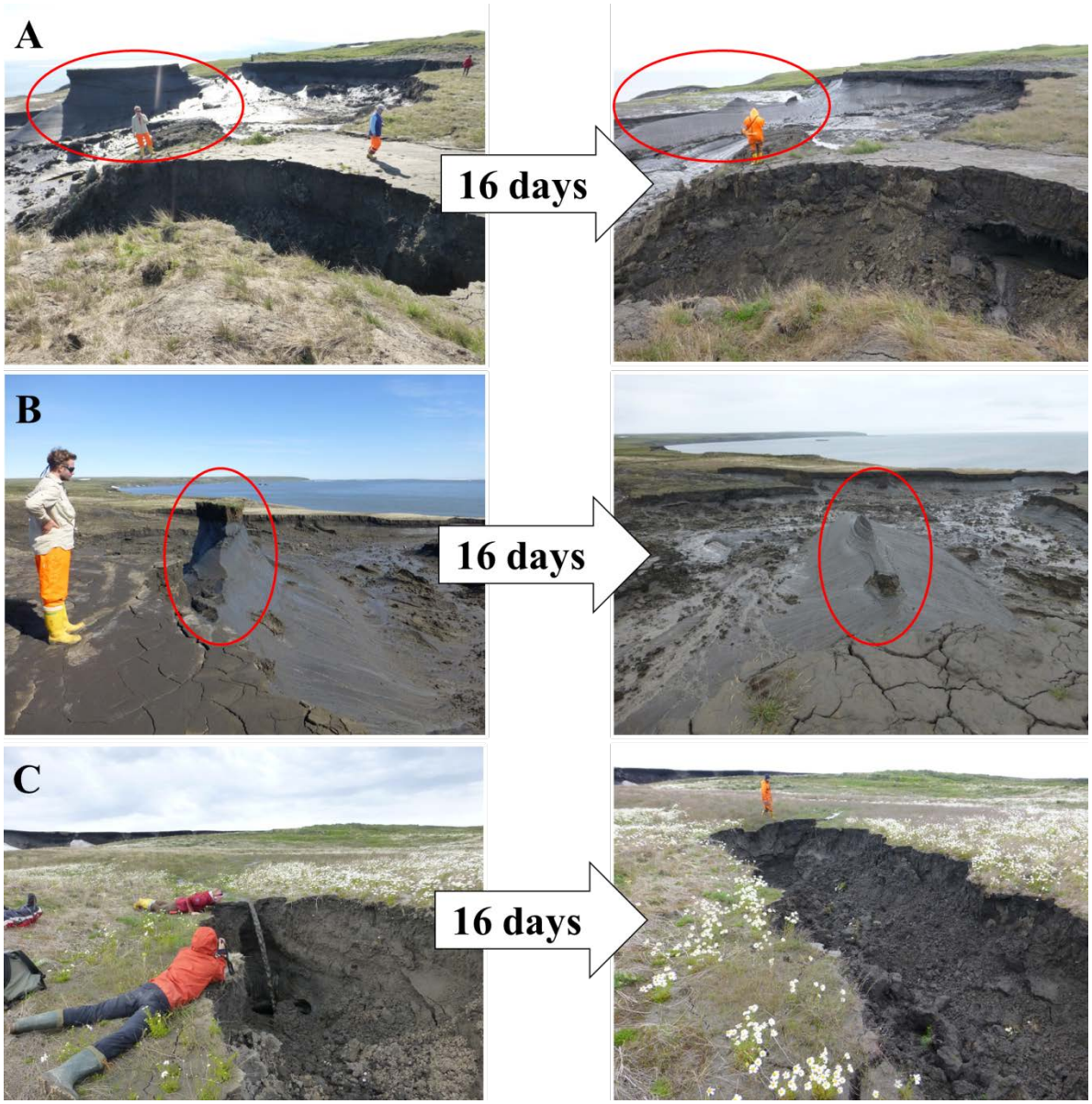

Figure 18. Photos of erosion in Slump D from 7 July (left) and 23 July (right) (i.e. a period of 16 days). Figure A and B are from the same location but taken from two different angles. They show the complete erosion of an ”island-like”, ice-rich permafrost headwall with a maximum diameter of about 30 m and a height of 8 m. Figure C shows landward erosion of the middle outflow channel into the slump floor, with about 6 m eroding over 16 days (from 9-25 July 2013).

5.1.2. Differential Global Positioning System (DGPS)

Figure 19 shows differential global positioning system (DGPS) measurements of the headwall outline from 2013 and 2014 overlain with a GeoEye satellite image from 2011. The upper headwall of Slump D was estimated to be 16 m high in July 2013. The headwall position was measured in 2013 and 2014 and showed a maximum retreat rate of up to 9 m per year. In July 2013, the upper northern headwall was up to 473 m from the shoreline.

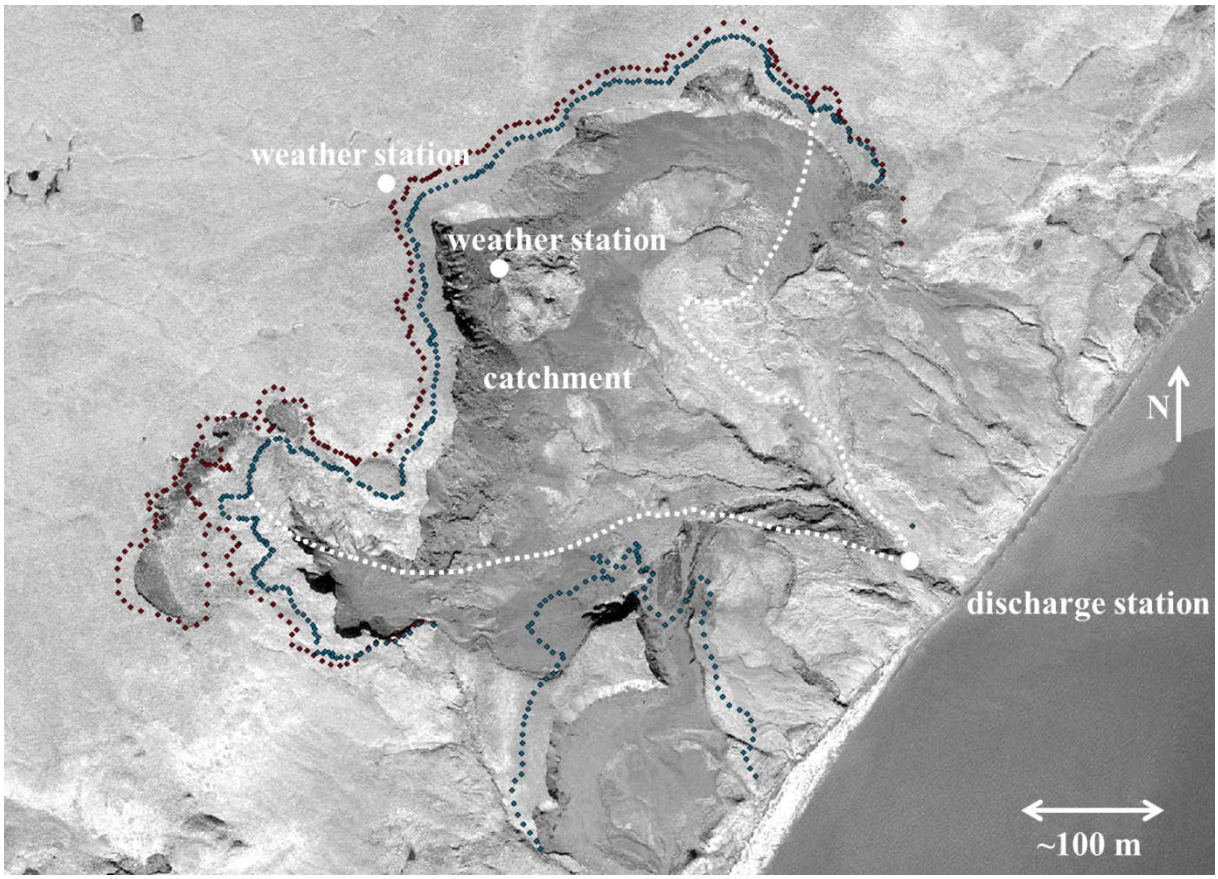

Figure 19. Geo Eye satellite image of Slump D in 2011 with DGPS measurements of the headwall position in 2013 (blue) and 2014 (red). The headwall position retreated up to 9 m from one year to the next. In 2013, the distance of the upper headwall to the shoreline was 473 m and the distance of the discharge station to the shoreline 50 m. The part of the catchment of the slump eroding into the outflow channel where the discharge station was located is shown with white dots. About 88 % of the total headwall surface eroded into the middle outflow channel.

5.1.3. Light Detecting And Ranging (LiDAR) and Digital Elevation Model (DEM)

The Light Detecting And Ranging (LiDAR) and Digital Elevation Model (DEM) from 2013 was used to extract basic geometric parameters for Slump D. The complete upper northern headwall was about 500m wide. Due to its uneven surface, the upper headwall was 1.255 m long on top and 1.163 m at the bottom of the cliff. The upper headwall eroded along 889 m and 88% of its surface eroded into the middle outflow channel (Figure 5 and Figure 19). The rest of the southern headwall eroded into the southern outflow channel, which was not equipped with a discharge station. The surface area of the total upper headwall was 26.712 m² whereof 23 617 m² eroded through the discharge station (Figure 19 and Appendix 0). The angle of the upper headwall was on average 24°.

The catchment eroding into the middle outflow channel included the undisturbed tundra behind the headwall, the headwall, the mud pool as well as the slump floor and was at least 136 000 m² (81 300 m² without the undisturbed tundra, Appendix 0) (Obu et al., 2016b).

5.1.4. Micrometeorology

5.1.4.1. Incoming Solar Radiation

Long-term Records:

Herschel Island is situated 69 °N of the Arctic Circle and has continuous daylight between 19 May and 25 July. Solar radiation reaches its daily minimum at around 03.00 am Inuvik time (UTC-6h; Figure 23).

Field Data July (2013)/August (2012):

Incoming solar radiation varied depending on the season, time of day and cloud cover. During the field seasons the average mean daily incoming solar radiation was 225 Wm^{-2} in the early thawing season of July 2013 and 157 Wm^{-2} in the later thawing season of August 2012. Minimum mean daily incoming solar radiation was 77 Wm^{-2} in July 2013 and 63 Wm^{-2} in August 2012 (Figure 20). Maximum mean daily incoming solar radiation was 336 Wm^{-2} in July 2013 and 224 Wm^{-2} in August 2012.

Peak incoming solar radiation values varied strongly depending on cloud cover (Figure 21 to Figure 23). On overcast days, incoming solar radiation reached maximum values of around 300 W m^{-2} (e.g. 9 and 24 July 2013) while on clear days without clouds maximum incoming solar radiation reach up to 711 W m^{-2} (measured at 15.22 pm on 13 July 2013, Figure 21). Partly cloudy days showed strong fluctuations of low and very high incoming solar radiation (e.g. 8 July 2013 and 8 August 2012). Extreme peaks over the maximum value of 711 W m^{-2} were observed on 10 July 2013 and are presumed to be due to additional cloud reflection (Figure 21).

Another abrupt decline of incoming solar radiation was recorded in the evenings once the angle of the sun was low and the shadow of the slump headwall hit the sensor. Good examples of this phenomenon can be observed on 21 July 2013 at 22.30 pm and on 8 August 2012 at 21.47 pm when values decreased to 9 W m^{-2} (Figure 22, Figure 23, grey bar number 4).

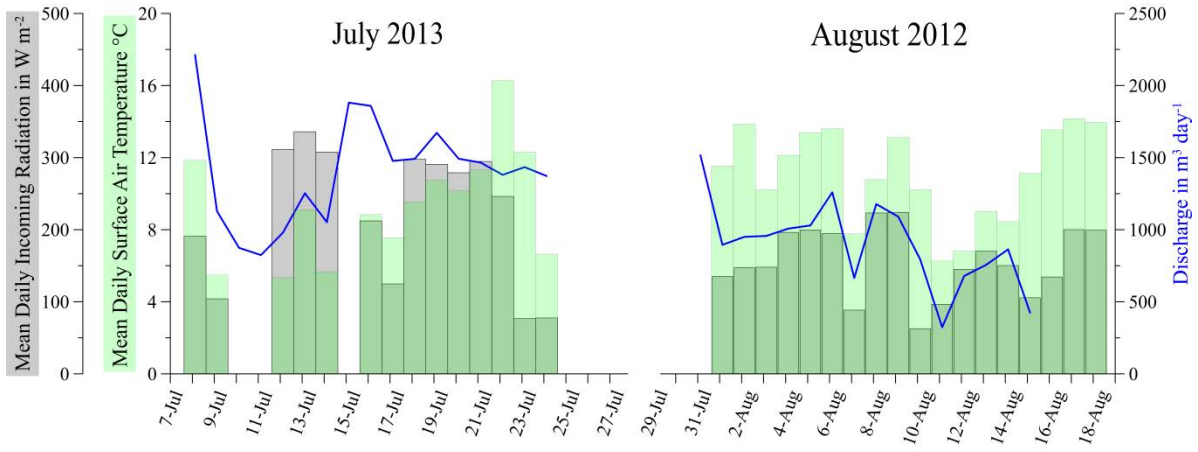

Figure 20. Seasonal evolution of mean daily incoming solar radiation (grey bars), mean daily surface air temperatures (green bars) and total daily discharge volume recorded at the slump outlet (blue line) between 8-24 July 2013 (left) and the 1-18 August 2012. Mean incoming solar radiation decreased over the season as the angle of the sun lowered. Discharge also decreased over the summer season, while air temperatures were higher in August (2012).

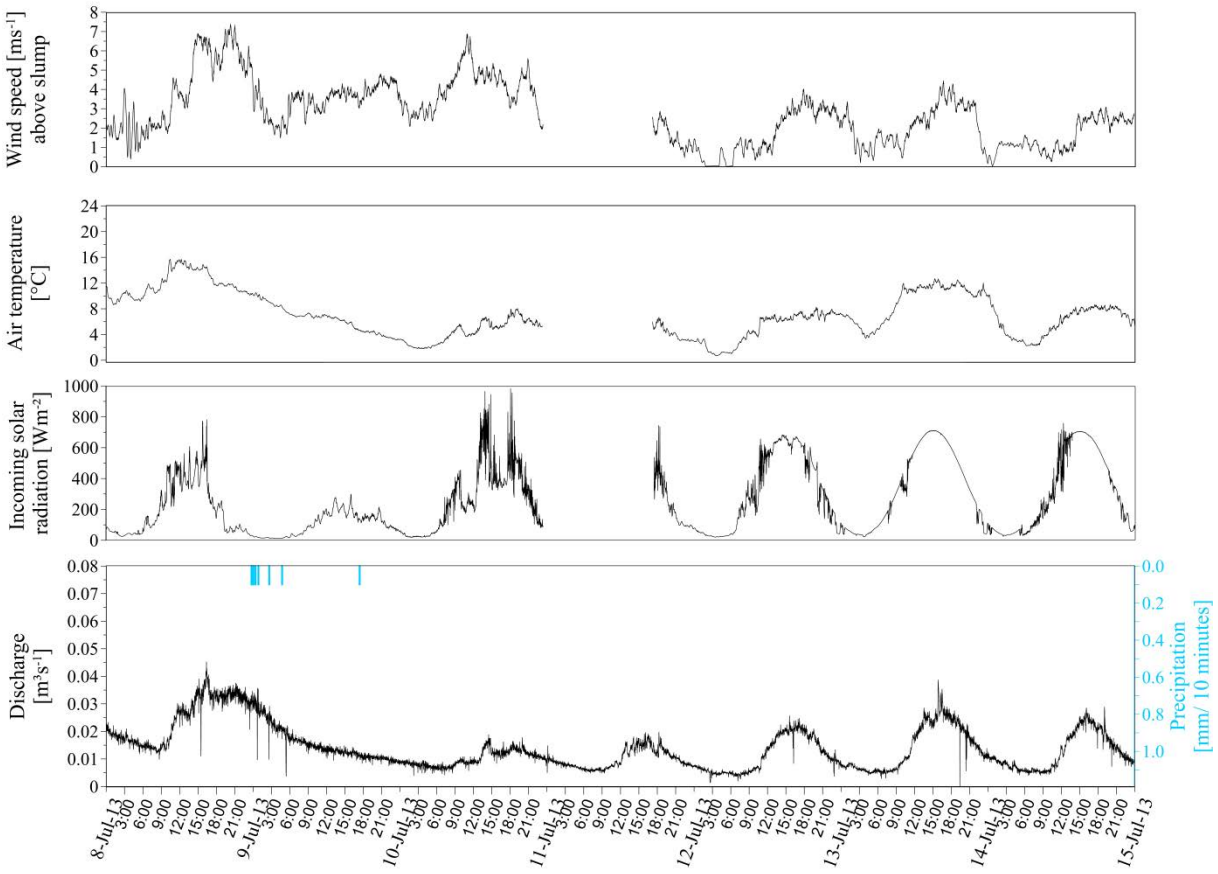

Figure 21. Meteorological and discharge records at Slump D between 8-14 July 2013. All data were recorded every minute and wind speed is displayed as 15-minute means. The diagram highlights diurnal as well as day-to-day variability. An almost optimal curve of a sunny day was recorded on 13 July 2013. On 9 July 2013 air temperatures and discharge dropped synchronously, despite incoming solar radiation reaching up to 300 W m^{-2}.

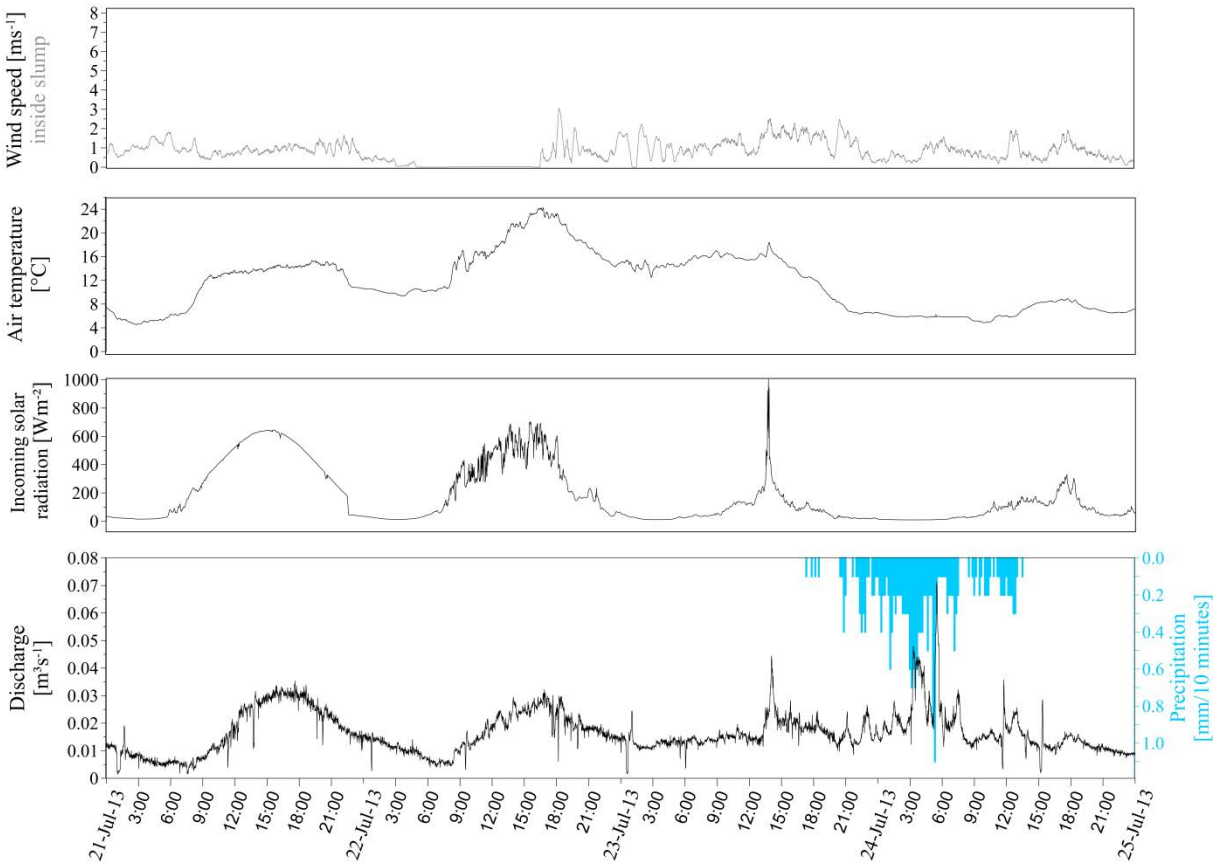

Figure 22. Meteorological and discharge records at Slump D between 21-24 July 2013. All data were recorded every minute and wind speed is displayed as 15-minute means. The diagram highlights diurnal as well as day-to-day variability. On 21 July, a sunny day, an ideal curve of incoming solar radiation was recorded until the shadow of the headwall reached the weather station at 22.30 h. In the morning of 24 July 2013 the strongest rainfall occurred and the highest discharge peak of both field seasons of 0.071 $m^3 s^{-1}$ was recorded.

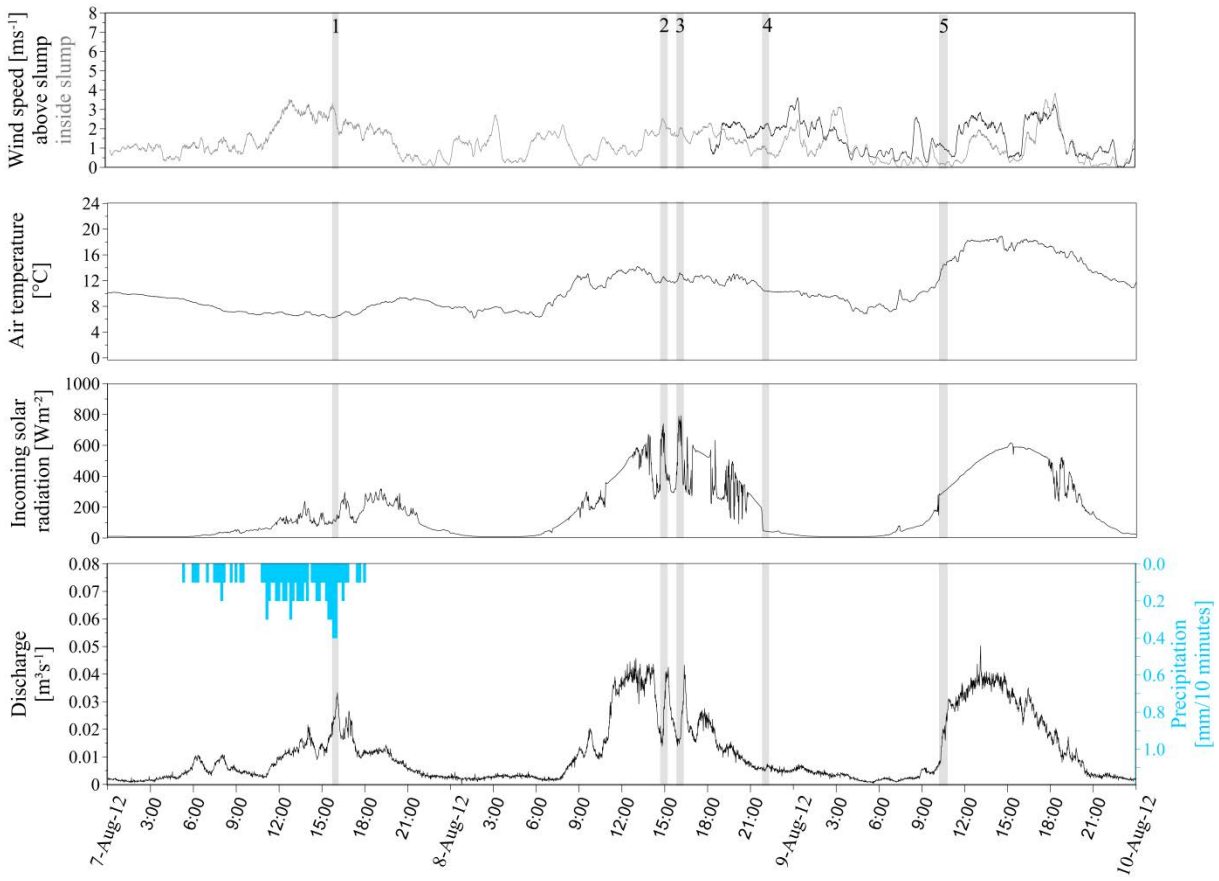

Figure 23. Meteorological and discharge records at Slump D between 7-9 August 2012. All data were recorded every minute and wind speed is displayed as 15-minute means. The chart shows the diurnal as well as day-to-day variability in the records. Bar 1 highlights a strong rainfall event followed by an increase in discharge. Bars 2 and 3 indicate the strong influence of incoming solar radiation on discharge 22 and 28 minutes after a peak value. Bar 4 shows an abrupt decrease of incoming solar radiation due to the shadow of the headwall. Bar 5 highlights an increase in incoming solar radiation and air temperature and the subsequent rise in discharge.

5.1.4.2. Surface Air Temperature

Long-term Records:

Long-term records from Environment Canada show an increase of air temperature on Herschel Island since the beginning of the twentieth century (Table 2). For the period 1900-1905, mean annual air temperatures were -12.0 °C, whereas mean annual air temperatures for the period 2009-2014 increased to -8.2 °C. Over the same time span, mean numbers of days with positive daily air temperature increased from 100 to 121, and thawing-degree days rose from 499.4 °C to 817.7 °C (Table 2). Mean daily air temperatures were commonly above zero degrees Celsius from late May to late-September, with the warmest months of the year being July and August.

Year	Mean annual temperature (°C)	July (°C)	August (°C)	Number of days with positive daily air temperature	Thawing degree days (°C)	Mean annual temperature (°C)	Mean number of days with positive daily air temperature	Mean annual thawing degree days (°C)
1900	-12.2	6.0	4.1	96	492.6			
1901	-12.6	7.3	5.4	102	517.8			
1902	-11.2	8.5	7.6	126	683.5	-12.0	100	499.4 °C
1903	-12.2	5.2	5.3	98	421.5			
1904	-12.1	7.0	4.5	81	436.2			
1905	-11.7	6.2	4.2	95	444.9			
1917	-12.1	4.7	4.9	95	401.6			
1974		5.6	4.5					
1994			7.8					
1995	-9.0	15.2	16.2	137	708.9			
1996	-10.1	7.7	7.2	98	537.8	-9.2	122	710.9
1997	-8.5	5.8	4.9	131	885.9			
2002	-8.1	8.4	6.6	129	520.6			
2003	-9.0	5.2	7.3	114	504.5	-9.3	120	591.9
2004	-10. 9	8.5	7.6	117	750.5			
2009	-8.2	8.2	6.1	117	615.3			
2010	-7.9	10.0	9.3	119	831.0			
2011	-9.1	9.9	8.7	126	786.2	-8.2	121	817.7 °C
2012	-7.6	15.0	11.8	125	1233.4			
2013	-9.1	8.6	8.9	112	736.4			
2014	-7.2	8.9	6.8	126	703.9			
2015								
2016		9.6	7,6	142	827.7			

Table 2. Surface air temperatures recorded on Herschel Island since 1899 with interruptions. The table highlights the air temperature increase between the period 1900-1905 and 2009-2014 with mean annual air temperatures rising from -12 °C to -8.2 °C, mean number of days with positive daily air temperature from 100 to 121, and mean annual thawing degree days from 499.4 °C to 817.7 °C (Environment Canada data are available from http://climate.weather.gc.ca/); Last update 20th October 2016).

Field Data July (2013)/August (2012):

Mean daily surface air temperatures on Herschel Island were above zero degrees Celsius from 6 June to 8 October 2012 and 26 May to 27 September 2013. In long-term records, July showed generally higher air temperatures than August (Table 2). However, 2012 was an exceptionally warm summer and August 2012 had a higher mean monthly temperature than July 2013. During the field season the mean surface air temperature was 9.3 °C in July 2013 and 11.1 °C in August 2012. The minimum mean daily surface air temperatures were 5.3 °C in July 2013 and 6.3 °C in August 2012 (Figure 20). The maximum mean daily surface air temperatures were 16.3 °C in July 2013 and 14.2 °C in August 2013.

Surface air temperatures fluctuated from day-to-day and varied from night to day by up to 12.0 °C. The minimum surface air temperature measured on 12 July 2013 was 0.7 °C and 4.4 °C in August 2012. The maximum surface air temperature recorded was 24.2 °C on 22 July 2013 and 19.5 °C in August 2012 (Figure 21-Figure 23).

Differences in recorded surface air temperatures between the weather station above the slump on the undisturbed tundra (weather station tundra) and inside the slump (weather station inside) in 2012 were less than ± 1.0 °C, showing the absence of a distinct microclimate inside the slump from a thermal perspective and prompting the use of a single weather station in 2013.

5.1.4.3. Precipitation

Long-term Records:

Rainfall occurs relatively infrequently on Herschel Island. Between 2006 and 2013, mean annual precipitation was 206 mm (recorded by the WMO Station on Herschel Island, Environment Canada) of which 70 % was recorded between June and October (Burn and Zhang, 2009).This is less than measured in Fort McPherson (about 350 km southeast) with a total annual precipitation of 295 mm and considerably less than values recorded on the Peel Plateau with already 200 mm in June to July (Kokelj et al., 2015).

Field Data July (2013)/August (2012):

Three rainfall events were recorded in July 2013 with 0.6 mm (over 5 hours), 5.9 mm (over 8 hours) and 22.6 mm (over 20 hours). In August 2012, three rainfall events were measured with 3.9 mm (over 12 hours), 8.4 mm (over 14 hours) and 7.5 mm (over 25 hours). In July 2013, the WMO station recorded all three events also recorded at Slump D, albeit with lower amounts (0.3/1.6/15.4 mm). Precipitation events in August 2012 were not measured at the WMO station due to technical problems.

5.1.4.4. Wind

Field Data 2012/2013:

Wind speed was the only meteorological parameter that showed differences between the weather stations located above and within the slump. In August 2012, the prevailing wind direction was from the northwest (~310°) and east/southeast (~120°; Figure 24). Wind coming from the east was recorded, with similar wind speeds at both weather stations at Slump D (14-16 August 2012; Figure 25). However, when wind came from the northwest, the headwall shielded the station located inside the slump and led to reduced wind speeds (10-13 August 2012). In July 2013, mean wind speeds were measured, with 2.8 m s^{-1} on the top of the Slump on the undisturbed tundra, and 1.0 m s^{-1} within Slump D. In August 2012, the mean wind speed was 2.5 m s^{-1} at the weather station on top and 1.5 m s^{-1} at the weather station inside Slump D. The wind was close to 0 m s^{-1} most nights but stronger during the day. In July 2013 the maximum wind gusts reached 9.3 m s^{-1} on top and 7.4 m s^{-1} inside Slump D. In August 2012 maximum measured gusts reached 12.4 m s^{-1} on top of the tundra and 8.8 ms^{-1} inside the slump at the same time.

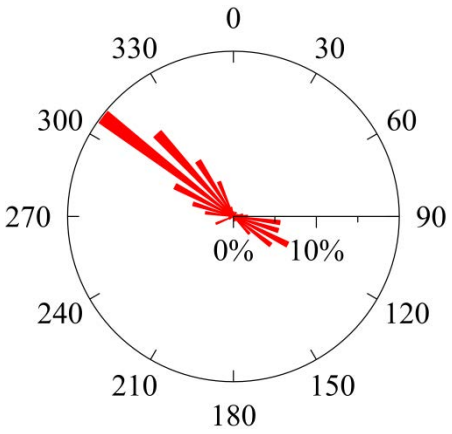

Figure 24. Wind diagram illustrating the wind direction of maximum gusts measured once an hour at the WMO Station on the east Spit of Herschel Island, 4 km away from Slump D. It recorded prevailing winds from the northwest (~310°) and east/southeast (~120°).

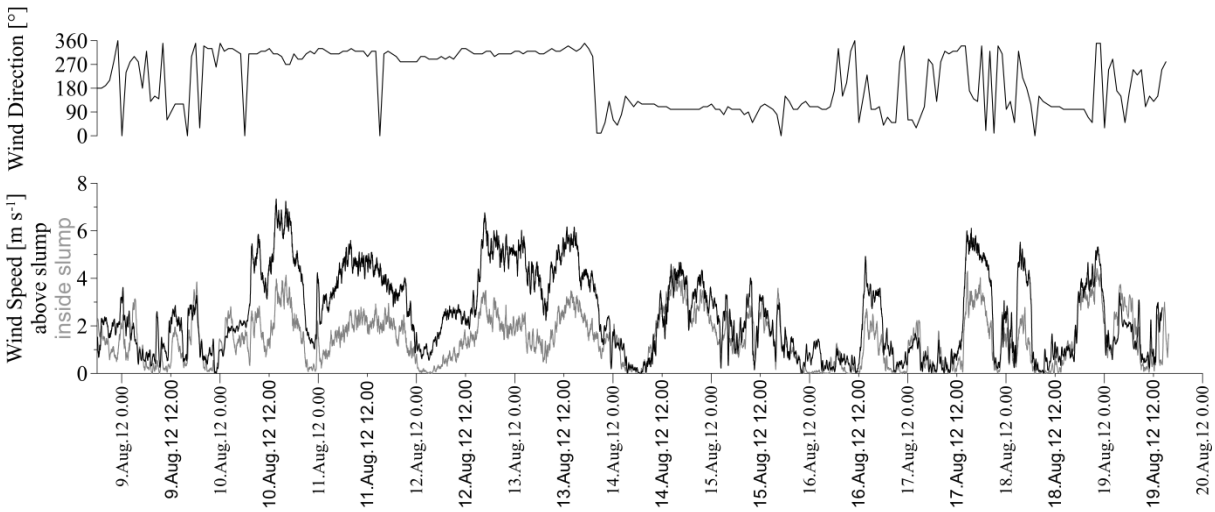

Figure 25. Wind direction measured at the WMO station 4 km away from Slump D (upper diagram) and simultaneously at Slump D both at the top and inside the slump (lower diagram). The data were recorded once a minute and displayed as 15-minute means. The diagram highlights the difference in wind speed between the two stations at Slump D when wind came from northwest (~310°) - wind speed was higher at the weather station above Slump D, on the undisturbed tundra (black), than inside Slump D, close to the shielding headwall (grey).

5.1.5. Discharge

The water ablated from the upper headwall was released via the cut-throat flume into the near shore zone and discharge showed diurnal, day-to-day, and seasonal (i.e. monthly) variability (Figure 21 to Figure 23). Seasonal variability was observed with mean daily discharge between 0.016 $m^3 s^{-1}$ and 1403 $m^3 day^{-1}$ in July 2013 compared to values between 0.010 $m^3 s^{-1}$ and 899 $m^3 day^{-1}$ in August 2012. In both field seasons, the total volume of sediment-meltwater over 18 days were determined and resulted in 25 000 m^3 in July 2013 and 15 600 m^3 in August 2012.

Discharge was also characterized by strong day-to-day variability. In July 2013, the early thawing season with lots of snowmelt, daily discharge was higher and varied between 824 $m^3 day^{-1}$ and 2212 $m^3 day^{-1}$ (Figure 20). In August 2012, daily discharge was lower and varied between 324 $m^3 day^{-1}$ and 1516 $m^3 day^{-1}$.

Diurnal fluctuations were characterized by maximum peak discharge in the afternoon and minimum flow at night. In July 2013, the discharge did not drop below 0.004 $m^3 s^{-1}$, whereas in August 2012 night time discharge dropped below 0.002 $m^3 s^{-1}$ (Figure 28). The highest measured discharge occurred after a rainfall event with 0.071 $m^3 s^{-1}$ during the night of 23/24 July 2013 (Figure 26).

The following sections describe the discharge fluctuations in more detail, in particular in response to the recorded microclimate.

5.1.5.1. Incoming Solar Radiation

An increase of discharge was observed at the outflow channel when incoming solar radiation reached values above 300 W m^{-2} (Figure 22 and Figure 23). In August, the response times ranged from 22 to 28 minutes (Figure 23, bar 2, 3). This time offset of around 25 minutes was due to the distance the eroding sediment-meltwater had to cover between the headwall and the discharge station (minimum of 423 m). For example on 9 July 2013 and 7 August 2012 incoming solar radiation values stayed below 300 W m^{-2} and discharge showed no response to smaller peaks of incoming solar radiation (Figure 23 and Figure 22).

On the cloudy day of 23 July 2013 incoming solar radiation was below 300 W m^{-2}. However, when sun came out from 13:32 pm to 14:07 pm incoming solar radiation reached values of 1004 W m^{-2} due to cloud reflection, which were higher than the measured 711 W m^{-2} on a clear day (Figure 22). Surface air temperatures were constantly high averaging around 15.7 °C before rising shortly to 18.4 °C. This 35-minute peak in incoming solar radiation had strong effects on discharge, with discharge volumes increasing within 32 minutes from 0.020 m^3 s^{-1} to 0.044 m^3 s^{-1}.

At night the gradual setting of the sun was reflected in an abrupt decrease in incoming solar radiation when the shadow of the headwall struck the weather station (Figure 23, bar 4). However, this did not lead to an abrupt decrease in discharge as the shadow gently reached the east facing upper headwall before that and incoming solar radiation was already below 300 W m^{-2} (21 July 2013 and 8 August 2012).

5.1.5.2. Surface Air Temperature

Surface air temperatures had a substantial impact on discharge volume. This was particularly visible when incoming solar radiation stayed under 300 W m^{-2}. For example, this effect could be seen on the overcast day of 9 July 2013 (Figure 21 and Figure 26, grey). Air temperature fell throughout the night and the day, from 9.0 °C to 2.0 °C, and discharge synchronously decreased from 0.025 m^3s^{-1} to 0.005 m^3s^{-1}. However, discharge volume dropped faster at night and more slowly during the day, when incoming solar radiation began to increase at 6:06 am to its maximum in the afternoon of 298 W m^{-2}.

Examples from three sunny days illustrate how the impacts of incoming solar radiation and air temperatures on discharge volume are difficult to separate.

The first example is from 13 July 2013 (Figure 27, yellow), which was a clear day with discharge volumes increasing as solar radiation increased. For the same incoming solar radiation values, the afternoon discharge values were higher than morning values (anticlockwise arrow Figure 27). Air temperatures during the day increased up to 13.0 °C, also resulting in an increase in discharge. However falling air temperatures in the afternoon were then followed by a decrease in discharge, although the level of discharge remained higher than in the morning (anticlockwise arrow Figure 27).

The second example is from the mostly sunny day of 21 July 2013 (Figure 27, blue). Discharge increased with rising incoming solar radiation and surface air temperatures until the afternoon. Thereafter, discharge subsequently decreased with decreasing incoming solar radiation (anticlockwise arrow Figure 27). However, discharge decreased before surface air temperatures reached their maximum and despite the fact that surface air temperatures continued to rise up to 15 °C. in the early evening This resulted in an 8-shaped curve of air temperature versus discharge (blue arrow, Figure 27).

The third example is from 9 August 2012, a clear day with little cloud cover (Figure 26 and Figure 27, red). Incoming solar radiation increased (excluding extreme peaks) up to around 570 W m^{-2} while air temperature rose to a maximum of 19.0 °C and remained high throughout the afternoon. Measured discharge reached very high values of up to 0.05 m^3s^{-1}, but discharge volume dropped in the afternoon before the maximum in incoming solar radiation was reached or before surface air temperature had started to drop. Thus higher discharge volumes were observed in the morning and lower discharges volumes in the afternoon (clockwise).

Comparing the three sunny days, discharge responded more strongly to high surface air temperatures than incoming solar radiation (Figure 27). The warmer the daily maximum is, the higher the peak discharge volume. This occurred despite the fact that maximum daily incoming solar radiation was lower. However, looking at all surface air temperature data from July 2013 and August 2012 and comparing them with discharge, there is no obvious direct correlation (Figure 28). The coefficient of determination between surface air temperatures and discharge was smaller than that between incoming solar radiation and discharge.

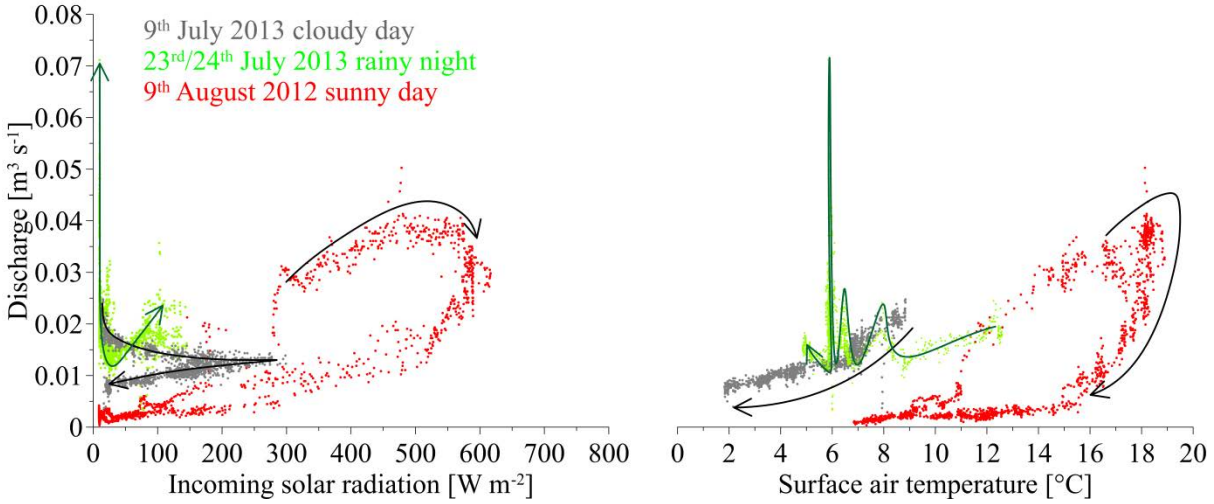

Figure 26. Relationship between incoming solar radiation and discharge (left) and surface air temperature and discharge (right) for three days from the two seasons of observations made at Slump D. The data are displayed for every minute. 9 August 2012 (3.00 am to 2.59 am) was a very warm and sunny day with an increase in incoming solar radiation and air temperature resulting in high discharge volumes. 9 July 2013 (3.00 am to 2.59 am) was an overcast day and incoming solar radiation reached a maximum of just 300 Wm^{-2} while air temperatures dropped during the day. On 23/24 July 2013 (17:18 pm to 13:13pm) the night was rainy and incoming solar radiation dropped in the evening and increased again in the morning. Temperature decreased continuously. Rain had the only impact on discharge resulting in a peak volume of 0.071 $m^3 s^{-1}$.

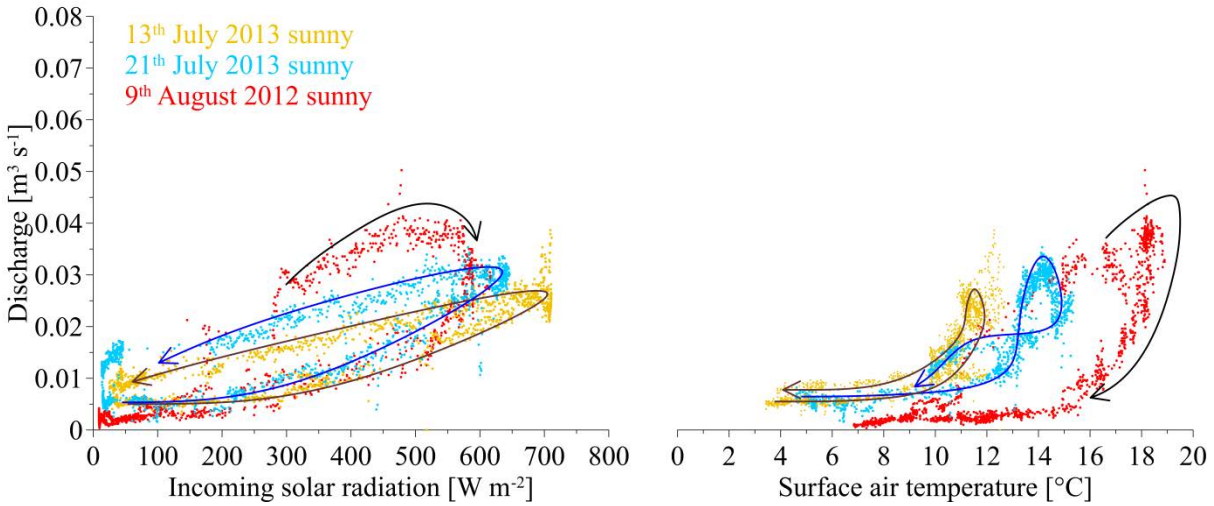

Figure 27. The relationship between incoming solar radiation and discharge (left) and surface air temperature and discharge (right). Three clear days (3.00 am to 2.59 am) are displayed, with observations from every minute plotted. Increasing incoming solar radiation was followed by an increase in discharge volume. On 13 and 21 July incoming solar radiation and discharge volume showed a clockwise trajectory while on 9 August the trajectory was anticlockwise. Comparing the three days, the maximum of discharge volume was higher with warmer air temperatures and lower incoming solar radiation. It highlights that both parameters are coupled to discharge volumes and difficult to separate.

Increasing incoming solar radiation and air temperatures led to an increase in discharge. More than 50 000 minutes of data from both field seasons show that higher incoming solar radiation and air temperatures led to increases in discharge volume (Figure 28).

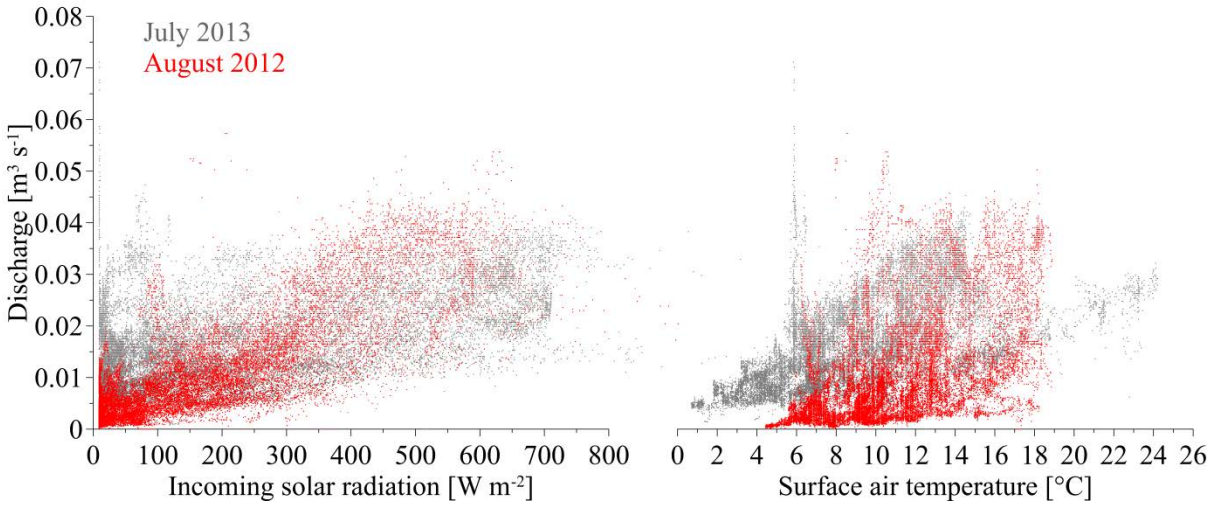

Figure 28. Incoming solar radiation (left) and surface air temperature (right) versus discharge volume. They illustrate more than 50 000 minutes of data from July 2013 (black) and August 2012 (red). Discharge volumes increased with both an increase in incoming solar radiation and air temperature. Interestingly, in July 2013 air temperatures were lower but discharge volume was higher.

5.1.5.3. Precipitation

Rain events also greatly modify the discharge volume, independently of air temperature or incoming solar radiation. Rain events characterized by accumulated precipitation greater than 0.2 mm over 10 minutes led to an increase in discharge within 10-26 minutes (23/24 July 2013 and 7 August 2012; Figure 22 and Figure 23 respectively). For instance, in the night from 23 to 24 July 2013, the highest rainfall event was recorded, with 22.6 mm of precipitation falling into the retrogressive thaw slump over 20 hours (Figure 26, green). At the time of the event, incoming solar radiation was below 300 W m^{-2} and air temperatures ranged between 4.5 °C and 13.0 °C. In the morning a "major" rain shower of 2 mm fell within 17 minutes. The discharge increased from 0.018 m^3 s^{-1} to a maximum of 0.071 m^3 s^{-1} 26 minutes after the heavy rainfall started. Discharge then went back to values around 0.012 m^3 s^{-1} 49 minutes after that heavy rainfall stopped. During the 20 hours of rainfall, discharge fluctuated strongly depending on the intensity of rain, however, it did not reach the maximum peak of 0.071 m^3 s^{-1} a second time.

The total amount of rain falling into the catchment of 136 000 m^2 was calculated and compared to the amount of discharge measured in the outflow channel during these rain events (Table 3). The aim was to verify if there was any additional mobilization of debris or an increase in the evacuation rate within the slump floor was observable.

The rain event on 3 August 2012 indicated that 3.9 l m^{-2} fell, resulting in 530 m^3 of precipitation falling into the catchment of Slump D. Over the same period of 11.5 hours, 406 m^3 was detected in the discharge station. If it is assumed that in the same period no ablation added to the discharge, 77 % of the rain passed through the outflow channel.

The same calculation was carried out for the other five rain events (Table 3) and showed that rainfall made up between 27 and 78 % of what passed through the outflow channel (again assumming no additional ablation or mobilization of debris). The rain event of 8 July was not included in further estimastions due to the minimal amount of precipitation that occurred (0.6 l m^{-2}).

In July 2013 minimum average discharge rarely went below 0.012 m^3 s^{-1}, and is here termed "basal flow" (Figure 29). Minimum discharge/basal flow before, during and after the rain period on 17 July was higher (0.020 m^3 s^{-1}) than on 23 July (0.012 m^3 s^{-1}). This basal flow was substracted from the discharge for these periods.

The rain event on 17 July 2013 was considered more precisely to calculate the amount of rain passing through the discharge station (Figure 29). The event can be characterized as a strong rainfall event, with 5.5 mm of precipitation falling in 98 minutes. The discharge increased 24 minutes after the rain started and returned to normal levels 27 minutes after rainfall stopped. An estimated 748 m^3 of precipitation fell into the catchment area (totaling 136 000 m^2). However, the discharge measured during the rainfall period was just 199 m^3 (27 %). When compared to the discharge measured before the rain event (0.02 m^3 s^{-1}, summing up to 118 m^3), i.e. the "base flow", this means that only 11 % of the rain was detected in the discharge station and 89 % penetrated into the tundra or the soil or evaporated.

The values presented in Table 3 indicate the maximum amount of rain detected in the discharge during precipitation events, however it is likely less rainfall actually reached the outflow channel since additional discharge, from e.g. ablation, can also be expected. In Slump D it was not possible to identify whether additional evacuation of slump material occurred, as observed in retrogressive thaw slumps on the Peal Plateau in Northwest Canada (Kokelj et al., 2015; Lacelle et al., 2010).

rain period	duration	rain in periode [l m^{-2}]	rain in total in 136 000 m² catchment [m³]	discharge in periode [m³]	maximum rain measured in flume [%]	basal flow in period [m³]	maximum rain measured in flume excluding basal flow [%]
08.07.2013 23:44 09.07.2013 04:44	300 min	0.6	82	459	rain amount too little		
17.07.2013 14:27 17.07.2013 22:05	450 min	5.9	802	556	69	540	2
17.07.2013 14:27 17.07.2013 16:04	98 min	5.5	748	199	27	118	11
23.07.2013 17:18 24.07.2013 13:13	1200 min	22.6	3074	1424	46	864	18
03.08.2012 03:31 03.08.2012 15:01	690 min	3.9	530	406	77		
07.08.2012 04:00 07.08.2012 17:44	825 min	8.4	1142	474	41		
10.08.2012 10:16 11.08.2012 10:46	1470 min	7.5	1020	793	78		

Table 3. The amount of precipitation that fell into the catchment compared to the amount of discharge detected in the cut-throat flume. Six rain events were recorded, with detailed observations taken on 17 July 2013. The shortest rainfall event occurred on this day, with 5.5 l m^{-2} of rain falling within 98 minutes, resulting in a maximum volume of 748 m³ falling on to the cathment area. In July 2013 minimum discharge was always greater than 0.012 m^3 s^{-1} and here is called “basal flow”. The basal flow was included in the estimation of how much rain was detected at the discharge station during each precipitation event.

5.1.5.4. Wind

Incoming solar radiation, surface air temperature and rainfall increase have a direct impact on discharge volumes (Figure 21 to Figure 23). By comparing the prevailing wind conditions and discharge it is not immediately obvious whether wind direction or wind speed have an impact on discharge volume.

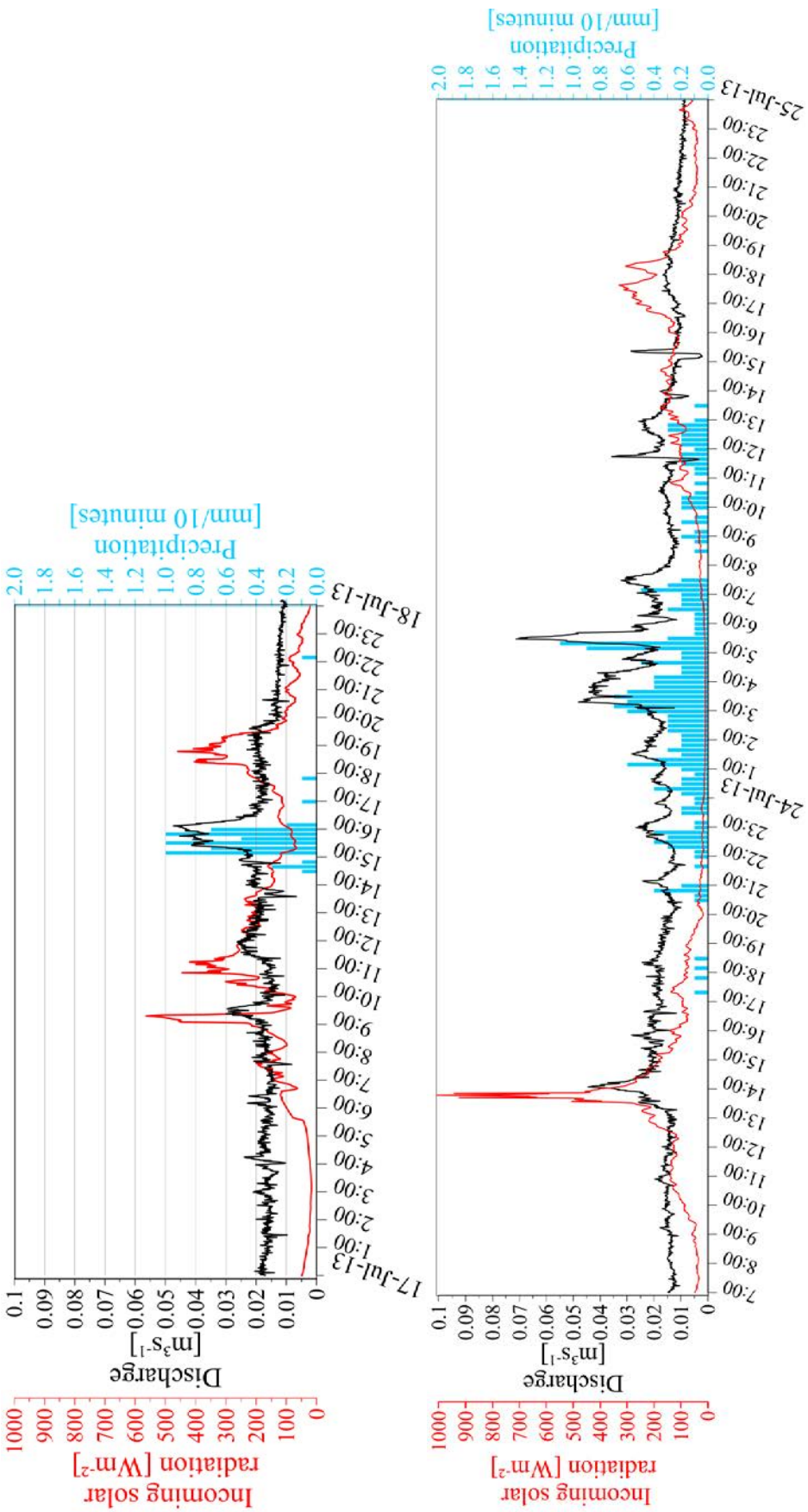

Figure 29. Hourly evolution of precipitation events on 17 and 23 July 2013. The plots also show incoming solar radiation and discharge volume for the same days. 5.5 l m^{-2} of rain occurred within 98 minutes during the rain event on 17 July. This lead to an increase in discharge volume 24 minutes after and decreased again to the level before 27 minutes after. This short and intense rain period gives the best approach to estimate the maximum amount of rain captured in the cut-throat flume measuring the discharge volume. On 23 July 2013 at 13:32 incoming solar radiation increased for about 35 minutes, and this was followed by a peak in discharge at 14:04. During the night of 23 July, 22.6 l m^{-2} of rain was recorded, and lead to the maximum peak of discharge volume measured on that day (0.071 m^3 s^{-1}).

5.1.6. Multiple Regression - Statistical Relationships between Micrometeorology and Discharge

Plotting the data on a daily basis, as done here, does not indicate any correlation between microclimatic parameters and discharge. Therefore a multiple regression was undertaken in the next step.

Several multiple regressions were conducted to test for statistically significant relationships between discharge and the following meteorological drivers: incoming solar radiation, surface air temperature and wind speed. The minute-resolution data were modified to account for the time lag of 22-28 minutes between peak incoming solar radiation measured at the meteorological station and the resulting peak discharge volume. This lag was determined to be 25 minutes, based on data from 8 August 2012, when peaks in radiation and discharge could clearly be identified (Figure 23). Precipitation events (three hours before and after) were not included in the multiple regression. The multiple regression identifies coefficients for the expression:

$$Q = a\,Q{\downarrow} + b\,T + c\,u_z - d$$

where Q is discharge ($m^3\ s^{-1}$), Q↓ incoming solar radiation ($W\ m^{-2}$), T surface air temperature (°C), and u_z wind speed ($m\ s^{-1}$). The multiple regression analyses were performed on three datasets, one with all the data (45 452 minutes, equation 1), one for the data record from July 2013 (21 947 minutes, equation 2) and one for August 2012 (23 505 minutes, equation 3). The following coefficients were retrieved from the regression with the statistical program R:

(1) $$Q = ((0.00003008) * Q{\downarrow}) + ((0.00059710) * T) + ((0.00101500) * u_z) - 0.00086970$$

(2) $$Q_{2013} = \left((0.00001718) * Q{\downarrow}_{2013}\right) + \left((0.00096170) * T_{2013}\right) + \left((0.00094180) * u_{z2013}\right) + 0.00112000$$

(3) $$Q_{2012} = \left((0.00004418) * Q{\downarrow}_{2012}\right) + \left((0.00037240) * T_{2012}\right) + \left((0.00105100) * u_{z2012}\right) - 0.00294100$$

For Equation 1 the p-value was $< 2.2*10^{-16}$. The partial correlation coefficient of the multiple regression was calculated to determine the respective statistical influence of meteorological variables on the discharge volume. The strongest impact was that of incoming solar radiation (0.66), followed by surface air temperature (0.32) and wind speed (0.21).

The aim of these calculations was to reconstruct discharge over the two field seasons just using the meteorological data. Ideally, this would allow an estimation of discharge volumes for the complete thawing season from June to September using the meteorological record. Equation 1 was used and the measured meteorological data were inserted to reconstruct discharge (Figure 30, red), which is compared to the measured discharge (Figure 30, black).

Daily fluctuations are well represented in the reconstructed discharge (Figure 30). For example, small but distinct variations in discharges were seen on 1 August 2012, with a minor discharge peak at noon and a more major peak occurring in the evening, both of which are well captured by the reconstruction. The reconstruction was, however, less successful at predicting the range of minimum and maximum discharge. In July 2013 the night discharge was high (over 0.03 $m^3 s^{-1}$) but the reconstructed discharge was too low, while in August 2012, when night discharge was almost zero, the reconstructed minimum discharge was too high.

To improve the reconstructed discharge, both field seasons were analysed separately. The multiple regression applied only to the data of July 2013 resulted in equation 2, and that applied only to data from August 2012 in equation 3. The p-values were $< 2.2*10^{-16}$ and significant in both cases. These two equations were used independently to reconstruct the discharge for July 2013 (dark blue; Figure 30) and August 2012 (light blue; Figure 30). These equations are better at predicting discharge than equation 1. In particular, the night discharge volumes were reconstructed more accurately by equations 2 and 3, but the daily maximum discharge volumes still differed by up to $\pm$ 0.015 $m^3 s^{-1}$ (+ 170 %) from the values measured at the discharge station. Actual peak discharge above 0.03 $m^3 s^{-1}$ was underestimated by all three equations. The adjusted R-squared values improved compared to the true measured discharge for the two the seasons separately (0.63 for July 2013 and 0.74 for August 2012).

Multiple regressions were also performed for selected single days characterized by clear-sky conditions. These regressions were conducted for 13 and 21 July 2013 and 9 August 2012 from 03:00 am to 2:59 am the following day (Figure 27). The multiple regressions had p-values of $< 2.2*10^{-16}$ and thus were significant. The adjusted R-squared values were 0.85 (13 July 2013), 0.80 (21 July 2013), and 0.78 (9 August 2012) and were higher than the ones calculated for the full field seasons of August 2012 and July 2013. The highest R-squared value was calculated for 13 July 2013, a day with very high incoming solar radiation values and lower air temperatures than for the other days.

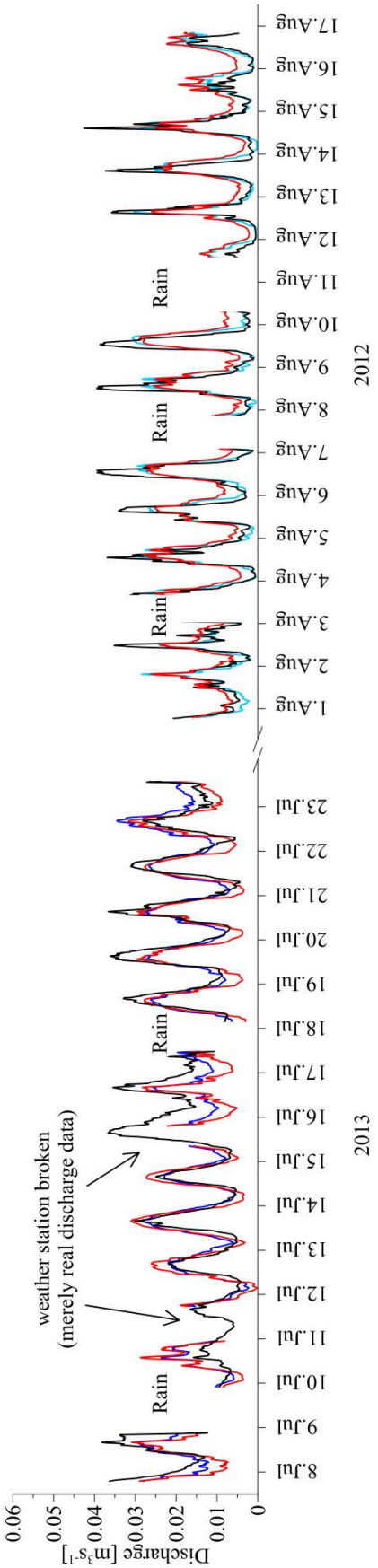

Figure 30. Measured discharge during the July 2013 and August 2012 field seasons (black). Missing records are caused by wildlife disturbances (11 and 15 July 2013) and manually excluded rain events (three hours before and after the rain event, on 9, 17 and 23 July 2012, and 3, 7 and 10 August 2012). Reconstructed discharge volume for the same seasons is also shown. The discharge volume was reconstructed using a multiple linear regression and minute-resolution meteorological records of discharge volume, incoming solar radiation, air temperature and wind speed. Three variations of the reconstructions are shown (August 2012 and July 2013 in red, July 2013 in dark blue, and August 2012 in light blue), with a running average of 59 minutes. Reconstructed discharge volumes reflect diurnal variations well, however, maximum discharge volumes above were generally underestimated.

5.2. Laboratory Analyses

5.2.1. Sedimentological Analyses

Discharge volume was not the only parameter that showed diurnal and seasonal variations. Sediment-meltwater samples were taken in the middle outflow channel of Slump D several times per day in July 2013 and August 2012. They showed fluctuations in the sedimentological and hydrochemical composition on diurnal and weekly scales, especially between the early and late thawing seasons (Figure 31). In total 78 samples from July 2013 and 81 samples from August 2012 were analysed to get a range of these fluctuations.

5.2.1.1. Sediment Content

Sediment concentrations varied similarly to discharge on diurnal and weekly timescales (Figure 31, yellow). A rise in discharge was nearly always paralleled by an increase of sediment concentrations. In July 2013 sediment concentrations varied between 16 and 253 g l^{-1} (median concentration of 82 g l^{-1}). In August 2012 the sediment content varied between a minimum of 29 g l^{-1} at night and a maximum of 457 g l^{-1} during the day (Table 4), while the median sediment content was higher than in July 2013 (196 g l^{-1}). Sediment concentrations in July 2013 did not reach the same maximum sediment concentrations during the day due to the additional contribution of snowmelt in the sediment-meltwater.

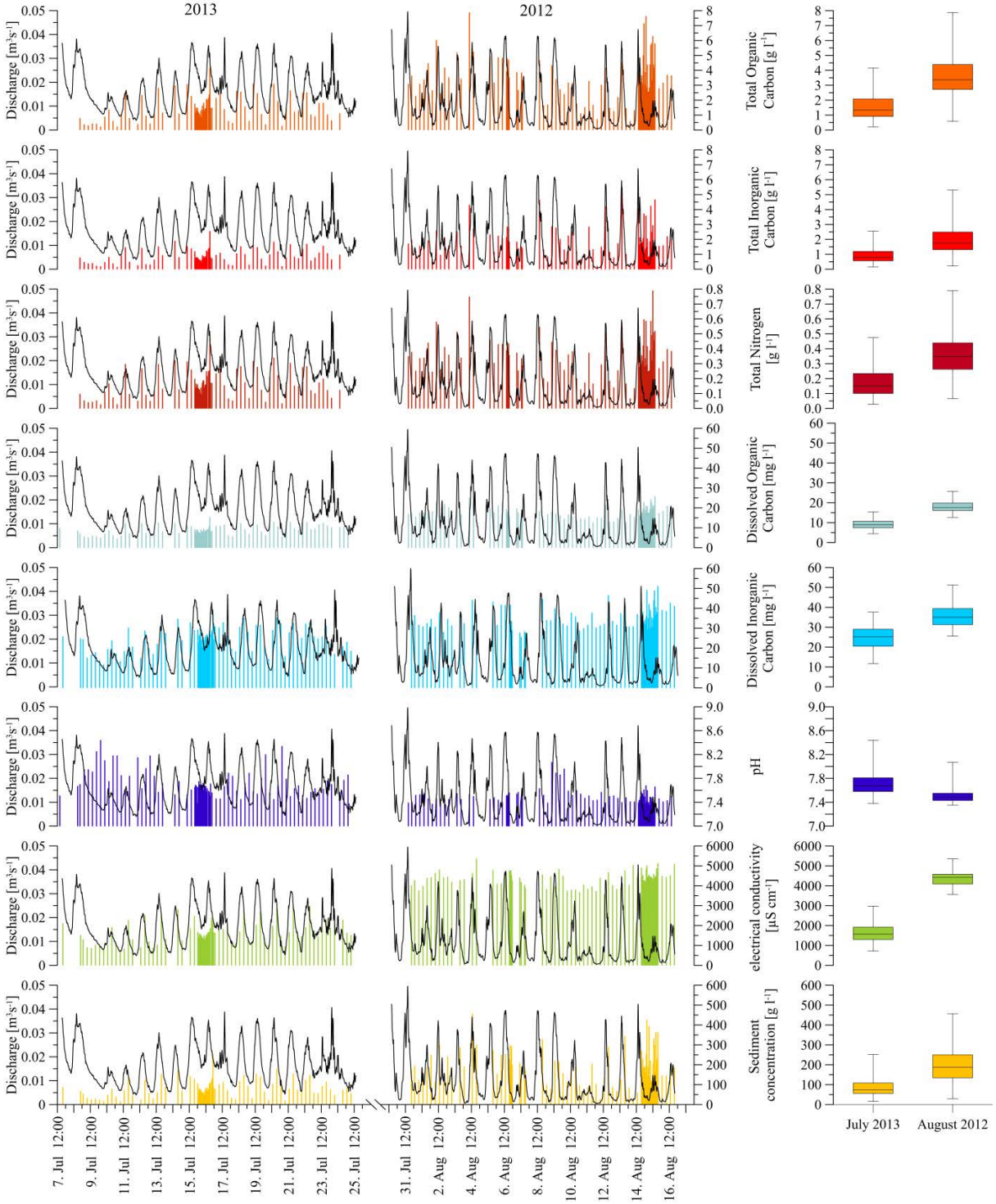

Figure 31. Diurnal variations of discharge and sediment-meltwater composition [g l^{-1}] during the field season of July-August 2013 (left). The box plots (right) show the seasonal variations of the sediment-meltwater samples between July 2013 and August 2012. Discharge (black curve) was measured every minute during both field season and samples taken at least every six hours. The data show fluctuations in sediment concentration, electrical conductivity, pH, dissolved (in-) organic carbon, total nitrogen and total (in-) organic carbon in g l^{-1}. The box plots show the median, minima, maxima, upper and lower quantiles of the hydrochemical and sedimentological data from July 2013 and August 2012.

5.2.1.2. Grain Size

Sediment-meltwater samples showed grain size distributions that fell into the range of sandy and clayey silt (Figure 32). However, it has to be considered that strainer porosity was below 5 mm and gravel and boulders were observed in the sediment-meltwater channel. Grain size distribution was analysed for 10 samples from July 2013 and 33 samples from August 2012. The distribution of clay was between 17 and 35 wt % and silt between 49 and 75 wt % during both seasons. Sand fractions of between 0 to 34 wt % were also detected. The median grain size from all samples was between 3.5 and 8.4 µm (Folk and Ward method, 1957).

Differences between the field season of August 2012 and 2013 are not noticeable (Figure 32 and Figure 33). In the vol % distribution, all samples showed peaks in the range of fine silt, with some samples showing an additional peak in the range of medium-sized silt and fine sand (bimodal, Figure 32). The samples were plotted in the sediment triangle diagram following Shepard (1954) and showed a distribution with a cluster in the range of clayey/sandy silt (Figure 32). The median grain size was 5.3 µm in July 2013 and 4.2 µm in August 2012. The difference in the median grain size may be an artificial effect due to the different number of samples taken in July 2013 and August 2012 (Figure 33).

Grain size distributions did not change with changing discharge volumes (Figure 34). Grain size samples were separated according to discharge volumes of <0.01 m^3 s^{-1}, >0.01 m^3 s^{-1}, >0.02 m^3 s^{-1}, and >0.03 m^3 s^{-1}. In the vol % distribution, all samples showed a peak in the fine silt range as well as a partial peak in the fine sand range. No clear relation is seen with discharge volume in the Shepard triangle.

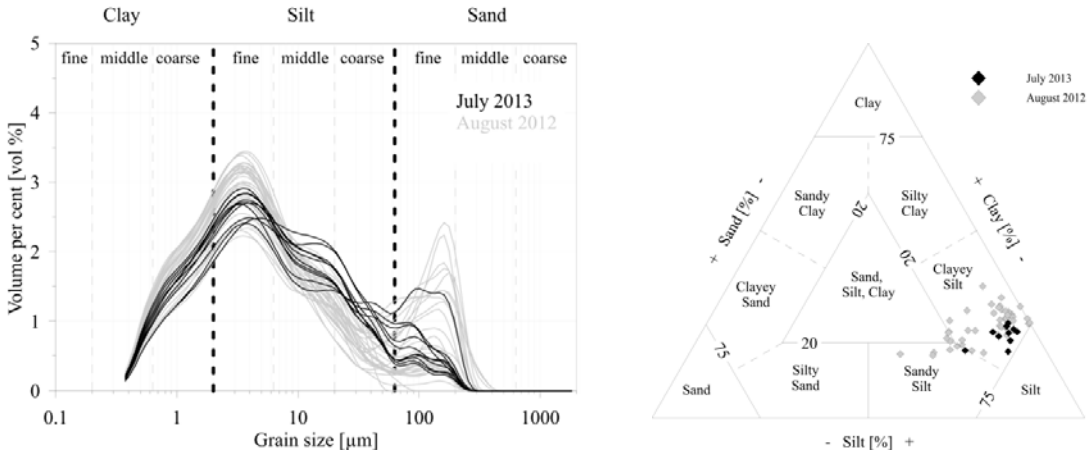

Figure 32. Grain size distribution versus volumetric per cent from 10 sediment-meltwater samples from July 2013 (black) and 33 samples from August 2012 (grey). Samples were taken through a strainer with a 5 mm sieve and were measured and analysed with a Gradistat (Blott and Pye, 2001) and plotted in the sediment triangle (right, after Shepard (1954). They are defined as clayey / sandy silt and do not show differences between the two seasons.

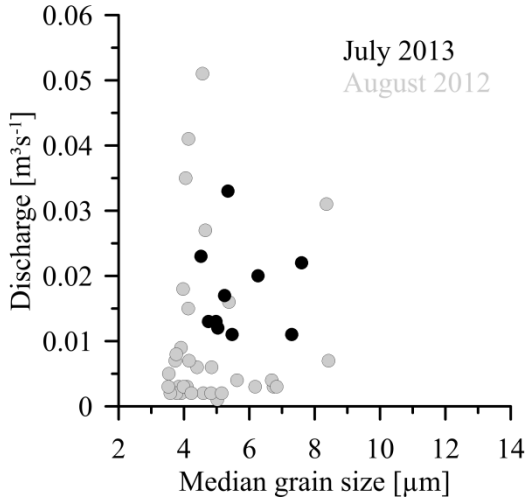

Figure 33. Median grain size versus discharge volumes of the samples taken in July 2013 and August 2012. No dependency between grain size and discharge volume is evident. Minimum discharge volume was higher in July 2013, while median grain size was 5.3 µm and therefore higher than that in August 2012 (4.2 µm). However, the limited number of samples and strainer porosity of 5 mm makes these estimates somewhat uncertain.

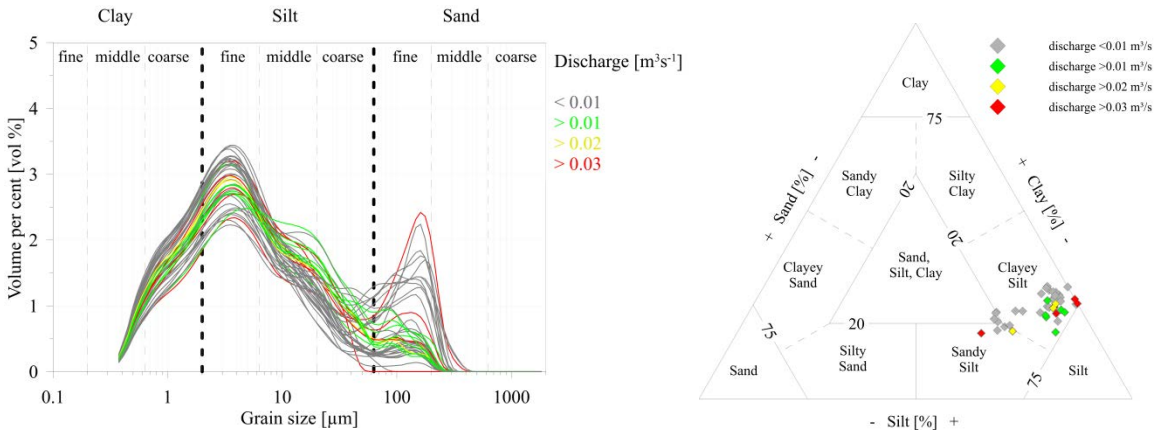

Figure 34. Grain size distribution versus per cent volume (left). The distribution of the sample between clay, silt and sand is visualised in the sediment triangle after Shepard (1954, right). Samples were divided into categories as per the discharge volume at the time when they were taken (< 0.01 m^3 s^{-1} (grey), >0.01 m^3 s^{-1} (green), >0.02 m^3 s^{-1} (yellow), and > 0.03 m^3 s^{-1}(red)). Grain size was evenly distributed into all four discharge volume categories.

5.2.1.3. Total Organic Carbon, Total Inorganic Carbon, and Total Nitrogen

Total Organic Carbon:

Sediment-meltwater samples were freeze-dried and the sediment was analysed for concentrations of total nitrogen, total carbon and total organic carbon. The total organic carbon in the sediment varied between 1.2 and 2.2 wt % (median of 1.8 wt %) in July 2013 and between 1.3 and 2.5 wt % (median of 1.8 wt %) in August 2012 (Figure 35 and Table 4). Due to distinct fluctuations in sediment concentrations, the total organic carbon concentration in grams per liter increased with increasing discharge (Figure 31, orange). In July 2013 organic carbon concentrations ranged from 0.219 to 4.159 g l^{-1} (median of 1.334 g l^{-1}). In August 2012 higher sediment concentrations led to more than double the amount of total organic carbon, with values between 0.576 and 7.876 g l^{-1} (median of 3.367 g l^{-1}).

Total Inorganic Carbon:

Samples from both field seasons showed similar values of total inorganic carbon in terms of weight per cent, however in July 2013 values were lower in terms of grams per liter. In July 2013, total inorganic carbon varied between 0.6 wt % and 1.5 wt % (median of 1.0 wt %). In August 2012 similar values were recorded, ranging between 0.6 and 1.5 wt %, with a median of 0.9 wt % (Figure 35 and Table 4). The inorganic concentration in the sediment varied

between 0.155 to 2.545 g l^{-1} (median of 0.790 g l^{-1}) in July 2013. In contrast, the higher sediment concentrations in August 2012 resulted in more than double the amount of total inorganic carbon (Figure 31, red), ranging between 0.213 to 5.315 g l^{-1} (median of 1.734 g l^{-1}).

Total Nitrogen:

Sediment samples showed that total nitrogen concentrations varied between 0.15 wt % and 0.27 wt % (median of 0.20 wt %) in July 2013 but were a little lower in August 2012, ranging between 0.14 wt % and 0.24 wt % (median value of 0.19 wt %; Figure 35 and Table 4). The increase in sediment concentration from July to August resulted in an increase in total nitrogen concentrations in terms of grams per liter (Figure 31, dark red). In July 2013, total nitrogen concentrations ranged from 0.028-0.475 g l^{-1} (median of 0.153 g l^{-1}), while in August 2012 values were more than twice as high, and ranged between 0.065 g l^{-1} and 0.789 g l^{-1} (median concentration of 0.349 g l^{-1}).

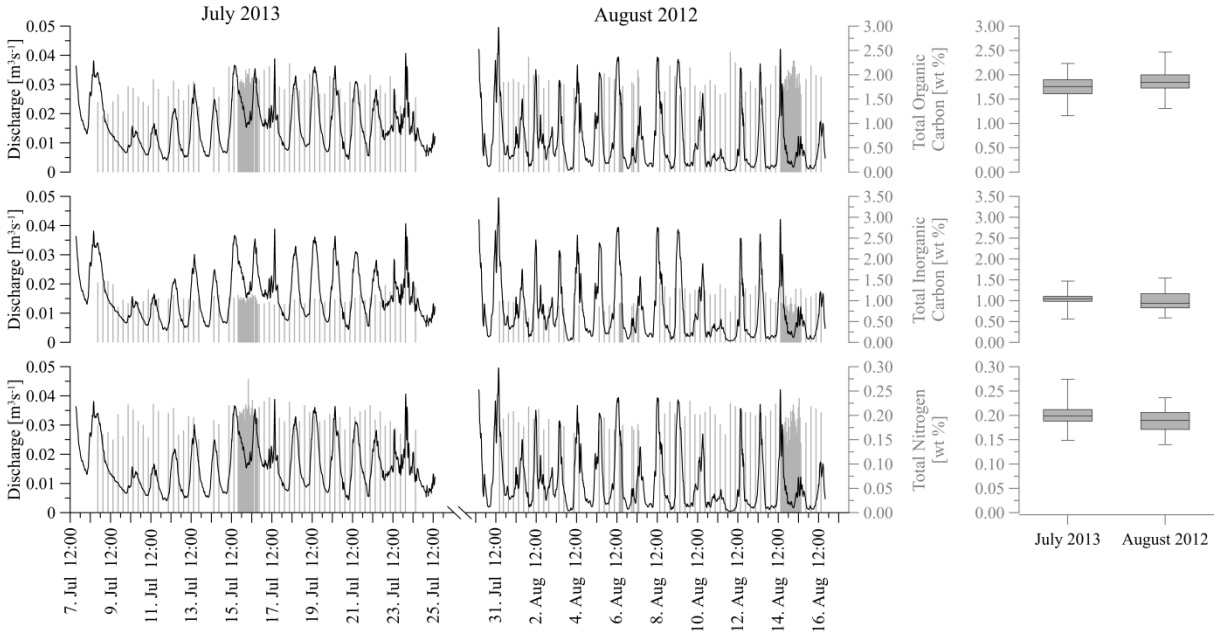

Figure 35. Diurnal variability of discharge and sediment-meltwater composition [wt %] during the field seasons of July 2013 and August 2013 (left). The box plots (right) show the seasonal variability in the sediment-meltwater samples (comparison of values from July 2013 and August 2012). Discharge (black curve) was measured every minute during both field season, while samples were taken on average every six hours. The data show fluctuations in total (in-) organic carbon and total nitrogen in wt %. The box plots show the median, minima, maxima, upper and lower quantiles values of the hydrochemical and sedimentological data from July 2013 and August 2012.

5.2.1.4. $\delta^{13}C$ and TOC / TN Ratio

Sediment-meltwater samples were analysed for $\delta^{13}C$ values in combination with TOC/TN mass ratios to provide additional information about the origin of the organic material (Figure 36). Samples had $\delta^{13}C$ values ranging between -28.5 and -26.1 ‰ (median of -26.4 ‰) and values formed a cluster with just one $\delta^{13}C$ outlier of 28.5 ‰. The TOC/TN mass ratio varied between 7.2 and 13.0 (median of 9.1). The samples were associated with lacustrine algae organic matter but also with a tendency to the C_3 land plants category (Meyers, 1994, 2003).

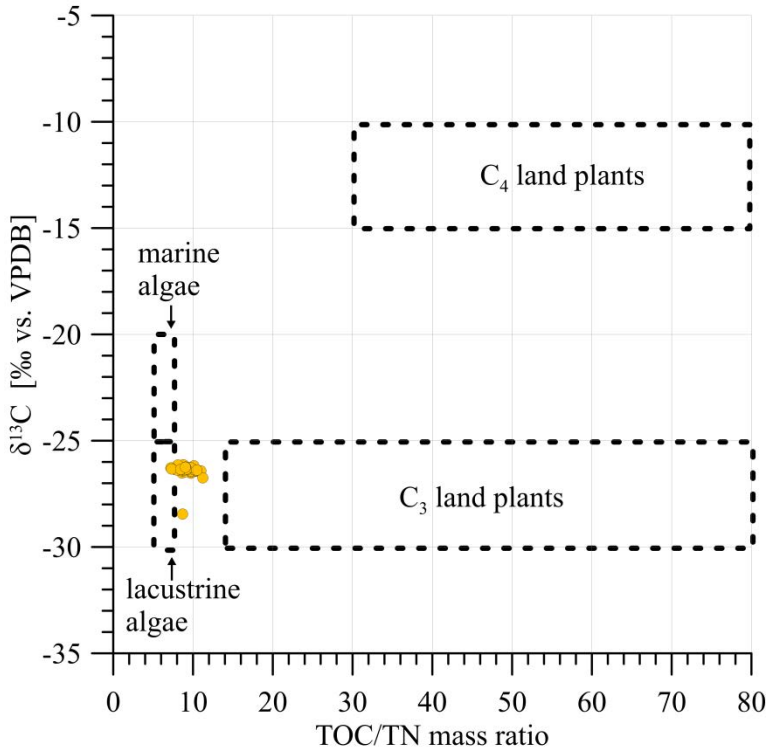

Figure 36. Total organic carbon and total nitrogen mass ratios (TOC/TN) compared to δ13C [‰ vs. VPDB]. Values indicate that the origin of the organic matter from the outflow samples of Slump D (orange dots) is lacustrine algae or C_3 land plants. Marine and lacustrine algae as well as C_3 and C_4 land plant classifications are modified to the TOC/TN mass ratio (modified after the TOC/TN atomic ratio; Meyers (1994) and (2003)).

5.2.2. Hydrochemical Analyses

5.2.2.1. Electrical Conductivity

Electrical conductivity is an indicator of the concentration of anions and ions in a sample. In July 2013, when snowmelt contributed considerably to sediment-meltwater, samples had electrical conductivity values that were three times lower than in August 2012 (Figure 31, green and Table 4). The two snow samples from July 2013 had electrical conductivities of 4 and 10 µS cm^{-1}. Sediment-meltwater samples from July 2013 showed distinct electrical conductivity fluctuations, with minimum values occurring at night when discharge values were low (as low as 718 µS cm^{-1}), while maximum values were observed during the day when discharge was high (up to 2975 µS cm^{-1}). The July 2013 median electrical conductivity value was 1566 µS cm^{-1}. In August 2012, electrical conductivity ranged between 3560 and 5360 µS cm^{-1}. The median value (4420 µS cm^{-1}) was three times higher than that in July 2013, and showed only little diurnal fluctuation.

	July 2013 (18 days)				August 2012 (18 days)				Both field seasons
	Min	Max	Median	Total	Min	Max	Median	Total	Median
Discharge [m^3 s^{-1}]			0.016	25000 m^3			0.010	15600 m^3	
Daily Discharge Volume [m^3]	824	2212	1403		324	1516	899		
Sediment Content [g l^{-1}]	16	253	82	2050 t	29	457	196	3058 t	121
Total organic carbon [wt %]	1.2	2.2	1.8		1.3	2.5	1.8		1.8
Total inorganic carbon [wt %]	0.6	1.5	1.0		0.6	1.5	0.9		1
Total nitrogen [wt %]	0.15	0.27	0.20		0.14	0.24	0.19		0.20
Total organic carbon [g l^{-1}]	0.219	4.159	1.334	33 t	0.576	7.876	3.367	53 t	2.437
Total inorganic carbon [g l^{-1}]	0.155	2.545	0.790	20 t	0.213	5.315	1.734	27 t	1.305
Total nitrogen [g l^{-1}]	0.028	0.475	0.153	4 t	0.065	0.789	0.349	5 t	0.253
Water content [%]	90	99	97	24250 m^3	83	99	93	14508 m^3	0.95
Dissolved organic carbon [mg l^{-1}]	4	15	9	225 kg	13	26	18	281 kg	13
Dissolved inorganic carbon [mg l^{-1}]	12	38	26	650 kg	26	51	35	546 kg	31
Electrical conductivity [µS cm^{-1}]	718	2975	1566		3560	5360	4420		3560
pH	7.4	8.4	7.7		7.4	8.1	7.5		7.6

Table 4. Minimum, maximum, median, and total amount of discharge volume and sediment-meltwater from samples taken in July 2013 and August 2012. Discharge was measured every minute and samples were taken every six hours. There are considerable seasonal fluctuations in discharge amount and sediment content.

5.2.2.2. pH Value

The pH-value is an indicator of the hydrogen ion activity in sediment-meltwater samples. In both field seasons, pH varied very little, ranging between 7.4 and 8.4 in July 2013 and between 7.4 and 8.1 in August 2012 (Figure 31, dark blue and Table 4). The median pH value in July 2013 was higher (7.7) than in August 2012 (7.5). In July 2013 distinct pH peaks were

detected in samples during periods with low discharge (pH up to 8.4), whereas the pH value dropped in samples with higher discharge amounts. In August 2012 pH values were in the same range but these strong fluctuations were not seen. Snow samples had a much lower pH of 6.4 and 6.5 in July 2013.

5.2.2.3. Dissolved Organic Carbon

Sediment-meltwater samples contained only half the dissolved organic carbon concentrations in July 2013 compared to August 2013 (Figure 31, light blue and Table 4). In July, dissolved organic carbon concentrations of 4 to 15 mg l^{-1} were measured (median of 9 mg l^{-1}). Values showed diurnal fluctuations, with higher concentrations observed during the day when discharge was higher. In August 2012, dissolved organic carbon content was higher and varied between 13 and 26 mg l^{-1} (median of 18 mg l^{-1}) and did not show distinct diurnal variability. The lower values in July are most likely due to the additional contribution of snow to sediment-meltwater.

Snow samples had dissolved organic carbon concentrations ranging of 0.4 and 0.5 mg l^{-1} in July 2013, which is much lower than the values recorded for sediment-meltwater and contributed to lower the values recorded at the discharge station in July.

5.2.2.4. Dissolved Inorganic Carbon

Just as dissolved organic carbon, showed dissolved inorganic carbon lower values in the early thawing season compared to higher values in the late thawing season (Figure 31, blue and Table 4). In July 2013, sediment-meltwater had high dissolved inorganic carbon values when discharge was high during the day and lower concentrations with lower discharge volumes at night. The values fluctuated between 12 and 38 mg l^{-1}, with a median value of 26 mg l^{-1}. Higher concentrations were measured in August 2012, with dissolved inorganic carbon between 26 and 51 mg l^{-1}, with a median of 35 mg l^{-1}.

The two snow samples taken in July 2013 had much lower dissolved inorganic carbon concentrations of 0.1 and 0.2 mg l^{-1}, indicating that snow melt resulted in a reduced dissolved inorganic carbon concentration in sediment-meltwater samples.

5.3. Fluxes of Sediment-meltwater

The values mentioned in the previous section were used to estimate fluxes to the near-shore zone. During each field season discharge was quantified over almost 18 days. In the early thawing season of July 2013 a total discharge of 25 000m³ was recorded, while in the late thawing season of August 2012 a total discharge of 15 600m³ was recorded (Table 4).

In July 2013 a sediment concentration of 82 g l^{-1} was measured, resulting in a total amount of 2050 t of sediment eroding into the near-shore zone. In August 2012 the sediment concentration was almost double (196 g l^{-1}), resulting in 3058 t of sediment being eroded into the near-shore zone.

Sediment included total (in-) organic carbon and total nitrogen. Total organic carbon concentrations of 1.334 g l^{-1} and 3.367 g l^{-1} were measured in July 2013 and August 2012, respectively. In total, therefore, 33 t of organic carbon was transported to the near-shore zone during the early thawing season, while 53 t as transported in the late thawing season. The total inorganic carbon concentration was slightly lower, with 20 t (0.790 g l^{-1}) being measured in July 2013 and 27 t (1.734 g l^{-1}) in August 2012. In July 2013 a total nitrogen concentration of 0.153 g l^{-1} were measured, resulting in a total of 4 t being eroded over the field season. In August 2013, the total nitrogen concentration was 0.349 g l^{-1} and therefore 5 t of total nitrogen was released into the near shore zone.

Sediment-meltwater showed very high sediment concentration. However, this should not mislead and assume that meltwater release was small. Looking at the sediment density, it becomes clear that meltwater is the major contributor in sediment-meltwater. The water volume in the discharge was quantified using the sediment concentration with a quartz density of 2.65 g l^{-1}. In July 2013, the headwall was covered with snowbanks and the water volume was 90 to 99 vol %, with a median of 97 vol %. In August there was no dilution of sediment-meltwater by snow. The sediment-meltwater had lower water volumes, ranging between 83 and 99 vol %, with a median value of 93 vol %. In a total, the discharge contained 24 250 m³ and 14 508 m³ of water in the 18-day field seasons of July 2013 and August 2012, respectively.

Finally, the eroding water volumes also contained dissolved (in-) organic carbon. In July 2013, 9 mg l^{-1} of dissolved organic carbon was measured, resulting in an erosion of 225 kg to the nearshore zone. August 2012 had a similar volume of 281 kg due to a lower discharge volumes and a higher concentration of 18 mg l^{-1}. In July 2013 650 kg (26 mg l^{-1}) and in

August 2012 546 kg (35 mg l^{-1}) of dissolved inorganic carbon eroded into the near shore zone in front of Slump D.

6. Discussion

6.1. Microclimatological and Geomorphological Factors Controlling Discharge

6.1.1. Diurnal Variations

Headwall ablation in retrogressive thaw slumps has been shown to respond directly to changes in incoming solar radiation, surface air temperature, wind speed and precipitation elsewhere in the Arctic (Grom and Pollard, 2008; Kokelj et al., 2015; Lewkowicz, 1985, 1986, 1987). However, this study shows that discharge at the slump outlet is not directly linked to ablation of the slump headwall. Rather, it is driven by additional parameters such as snow melt, infiltration and evaporation. This has large consequences for the pace at which sediment-meltwater is released from the slump.

Erosion of retrogressive thaw slumps varies substantially on a diurnal basis. On Banks Island, Lewkowicz (1986) described diurnal variations of ablation following net radiation fluxes. The diurnal cycles were most marked on sunny days. Similarly, Kokelj et al. (2013) observed that streams affected by retrogressive thaw slumps on Peel Plateau had diurnal variations of turbidity lagging 2-3 hours after the maximum in incoming solar radiation (Kokelj et al., 2013).

Various climatological factors control diurnal variations of discharge. At Slump D, where the outflow volume can differ by up to a factor of 4 between night and day, incoming solar radiation has the strongest microclimatological impact on discharge and was the main driver during both field seasons (partial correlation coefficient 0.66, chapter 5.1.6). Lewkowicz (1986) describes that at least 60 % of the ablation in a retrogressive thaw slumps are generated from net radiation.

Incoming solar radiation is obviously strongly connected with surface air temperature (partial correlation coefficient 0.32). Together they are the main climatic driver of discharge. This becomes clear particularly when looking at individual days (Figure 27). The 13 and 21 of July 2013 showed an increase in incoming solar radiation followed by an increase in discharge volume. Incoming solar radiation was higher on 13 July 2013 with 711 W m^{-2} compared with 646 W m^{-2} on 21 July 2013. However, on 21 July surface air temperatures were higher and led

to higher peak discharge. This demonstrates the importance of both incoming solar radiation and surface air temperature on discharge volume.

Interestingly, discharge volume can decrease before incoming solar radiation or surfaces air temperature reach their maximum. For example, on 9 August 2012 discharge volume decreased before incoming solar radiation and surface air temperatures reached their maximum. This suggests that there may be other geomorphological factors that affect discharge such as additional accumulation of sediment-meltwater and delayed release thereof. This additional storage, which possibly is in the mud pool, replenishes slower than the release of water from the slump outlet (Figure 27).

This behavior suggests a “storage effect” in the slump catchment. It can be hypothesized that this effect is associated with fluctuating storage of water in the area located between the headwall and the outflow channel, including the slump floor and mud pools (Lantuit and Pollard, 2005, 2008; Lewkowicz, 1986). It can be assumed that this reservoir may become exhausted on clear and warm days and recharge throughout the night (6, 8, 9 and 13August 2012).

The storage effect explains the occurrence of sporadic massive mud flows in retrogressive thaw slumps, such as the ones described by Lacelle et al. (2010) and Kokelj et al. (2013). At Slump D, the occurrence of a mudflow was observed on 16 August 2012. The mudflow transported blocks of sediment weighing an estimated 150 kg and was able to move boulders exceeding 80 cm in diameter. The total volume of sediment carried by this extreme event is unknown, yet observations indicate that the mudflow led to a change in the diameter of the flow in the slump outlet from 20 to 150 cm. Mudflows with velocities higher than walking speed were also observed on the lower southern headwall of Slump D. Mudflows are therefore believed to release considerable volumes of water and sediment over short periods of time.

Rainfall can also contribute to modify discharge. Rainfall is not included in the multiple regression, because of its infrequent occurrence in the study area, but it clearly contributes to increase discharge drastically (Figure 22, Figure 23, Figure 29). On the Peel Plateau, where slump discharge is known to be intrinsically linked to rainfall, precipitation of 200 mm was measured from June to July (Kokelj et al., 2015). On Herschel Island, precipitation is much lower. In July 2013, 34.6 mm was measured and in August 2012, 19.8 mm. The contribution of rainfall to the annual discharge is virtually insignificant, but it could have indirect effects in

terms of redistributing material at the surface of the catchment and facilitating further entrainment of sediment by subsequent mudflows or mass movements. Kokelj et al. (2013) describe mass movement of eroding material caused by strong rainfall events, clearing of accumulated materials and exposure of new ground ice (Kokelj et al., 2013; Kokelj et al., 2015; Lacelle et al., 2010). At Slump D, rainfall does not lead to an increase in sediment content in the water at the outlet, but it could have an indirect effect on sediment mobilization in the slump catchment by increasing the moisture content of the sediment.

During rainfall events, the discharge measured at the outlet is substantially lower than that expected from the amount of water that falls into the catchment. The watershed of the sediment-meltwater channel contained undisturbed tundra and slump floor over 136 000m². On 10/11 August a rain event of 7.5 l m^{-2} in 24.5 hours occurred. Assuming there was no additional discharge due to thawing of the headwall, 78 % of the total rainfall was detected in the cut-throat flume (Table 3). This indicates that 22 % of the rainfall either evaporated or percolated into the ground. However, on that day, incoming solar radiation and relatively high surface air temperatures (up to 11.3 °C) probably caused thawing of the permafrost headwall and also had an impact on the volume of sediment-meltwater released through the outlet. It is not possible to calculate the proportion of discharge from rain or from thawing of the permafrost headwall.

A short and intense rainfall event showed that major amounts of rain do not flow through the sediment-meltwater channel. For example, on 17 July 2013 5.5 mm of rain fell in 98 minutes. This led to a total rain volume in the watershed of 748 m³, however just 199 m³ was recorded in the cut-throat flume (27 %). Furthermore, given that these observations were made in July, a constant basal flow of 0.02 m^3s^{-1} leading to a volume of 118 m³ in this rain period had to be subtracted (Table 3). Hence, only 81 m³ (11 %) of rainwater discharge may have arrived in the cut-throat flume. The remaining 89 % percent is likely lost through evaporation and infiltration.

Evaporation and infiltration are not quantified in this study and probably are spatially very heterogeneous, given the high variability in terrain characteristics within the catchment, ranging from completely vegetated to non-vegetated. However, these processes may play an important role in lowering the amount of water being transported to the outlet.

Evaporation may lead to loss of water and soil moisture in the slump catchment. This fact was only recognized after the field campaigns were completed and therefore no specific

measurements of evaporation were made. However, the photo in Figure 37 shows extensive evaporation along the northwest coast of Herschel Island. This terrain is similar to Slump D, which is, made of water-saturated clayey sediments (see also Figure 38). No evaporation can be seen from the dry surface, but there is considerable evaporation from the fresh eroding moist surface (Figure 39). This is in accordance with observations from Priestley and Taylor (1972) who showed that bare soils show reduced rates of evaporation. The surface drying effect is also mentioned by Woo et al. (1992). In the Arctic evaporation is higher than precipitation and is predicted to increase with warming temperatures (Woo et al., 1992).

Figure 37. Photo from 8 August 2016 at 1 pm on the West Coast of Herschel Island. Evaporation can observed from the slump floor and is likely to occur in a similar manner from Slump D.

Figure 38. Picture shows evapo-transipiration observed in a slump floor along the West Coast of Herschel Island on the 8 August 2016. The sediments maling up this slump are clayey and water saturated, similarly to Slump D.

Figure 39. Evaporation observed on the West Coast of Herschel Island. Bare soil forms a dry crust after a few days leading to reduced evaporation (left). However, water-saturated freshly thawed permafrost shows strong evaporation (right).

Subsurface conduits may be another major cause for the loss of rain water from thaw slumps. In July 2013, several subsurface conduits, about 2 m below the dry stabilized old slump floor, were observed releasing water into the slump outlet (Figure 40). There are several possibilities explaining the presence of these conduits: 1) The conduits may flow a few decimeters to meters below the slump floor through freshly accumulated debris. 2) Water from surface runoff can penetrate through cracks in the dried surface and into the ground (Figure 41). 3.) Conduits can form along the water-saturated mud pool, erode underneath the surface and flow at the permafrost table. It is likely that more subsurface conduits were present in the slump floor but no others were detected.

Figure 40. Conduit that transported sediment-water below the surface and entered the outflow channel of Slump D. It is possible that the conduit meandered at the permafrost table in the debris accumulated on the slump floor, coming out just at the frozen-unfrozen boundary.

Figure 41. Conduits flowing into the sediment-meltwater channel. Similar to Figure 40, these conduits could have meandered through the slump debris at the permafrost table, being fed by surface water trickling down through dried cracks.

In summary, discharge is characterized by strong diurnal fluctuations. Unlike other locations in the Arctic, at Slump D it is largely not affected by precipitation rather it is primarily driven by incoming solar radiation and air temperature. Incoming solar radiation and surface air temperature drive both ablation and discharge. However, other factors such as precipitation and evaporation also affect discharge.

6.1.2. Seasonal Variations

Seasonal variations in discharge were due to large amounts of snow remaining along the headwall in July 2013. In July 2013 sediment-meltwater volumes were a total of 25 000 m^3. In August 2012, on the other hand, with no additional snow contribution, only 15.600 m^3 were released.

Although, on Herschel Island snow generally accumulates on flat tundra only to a height of approximately 17 cm (Burn and Zhang, 2009), higher snow accumulations of at least 3 m were observed due to snowdrifts along the headwall of the retrogressive thaw slump. The snowbanks protect the ice-rich permafrost from thawing (Balser et al., 2014) and therefore delay headwall ablation.

In the beginning of the July 2013 field season, the top parts of the permafrost headwall were partially exposed while lower parts were still covered with thick snowbanks. The area of snow coverage then decreased during the season, from about 90 % to about 35 % late in July 2013 (Figure 14). The exposed top part of the headwall made up of permafrost, which thawed and slid down on to the snowbank. The sediment-meltwater from this permafrost then infiltrated through the porous structure of the snowbank, leaving a layer of debris (Figure 16, Figure 17). Occasionally, thawed permafrost was observed to slide immediately into the mud pool rather than accumulating on the snowbank.

August had negligible snow patches (Figure 12) and the thawed permafrost material could glide over the smooth, slightly thawed headwall underneath, with no pores for the sediment-meltwater to infiltrate through. Instead the thawed permafrost could erode directly into the mud pool.

The temporal offset between surface snowmelt and runoff depends on the snowpack thickness and can take up to several days (Marsh and Woo, 1984; Pohl and Marsh, 2006). In Slump D, the response time between forcing from incoming solar radiation and subsequent variations in

discharge varied considerable throughout the season (Figure 42). The 16-day average from each year showed incoming solar radiation increased above 25 W m^{-2} at 4:34 am in July and at 6:36 am in August. Discharge increased around 8:28 am in July and around 7:21 am in August. In the morning, the time lag of discharge in the sediment-meltwater channel is therefore about 4 hours in July while in August it is only about 45 minutes. The longer July response time is caused by thawed permafrost and meltwater taking more time to infiltrate and erode through the snowbanks, while in August negligible snow is present. Furthermore, the response time to the midday peak in incoming solar radiation varies from July to August. In July the response time is around 2 hours (for example, the July 2013 average maximum incoming solar radiation peaks at 13:41 pm and the maximum in discharge occurs around 15:50 pm). In August, in comparison, the response time is much faster, ranging between 22-28 minutes. The difference between morning and afternoon response times is likely due to the lower amount of energy available in the morning (Lewkowicz and Young, 1990). In addition, in July the discharge decreased only very slowly during the night and never reached zero (Figure 42). This demonstrates the additional time the meltwater needs to percolate through the snowfield, taking more than 9.5 hours, before the next day's incoming solar radiation starts to increase again.

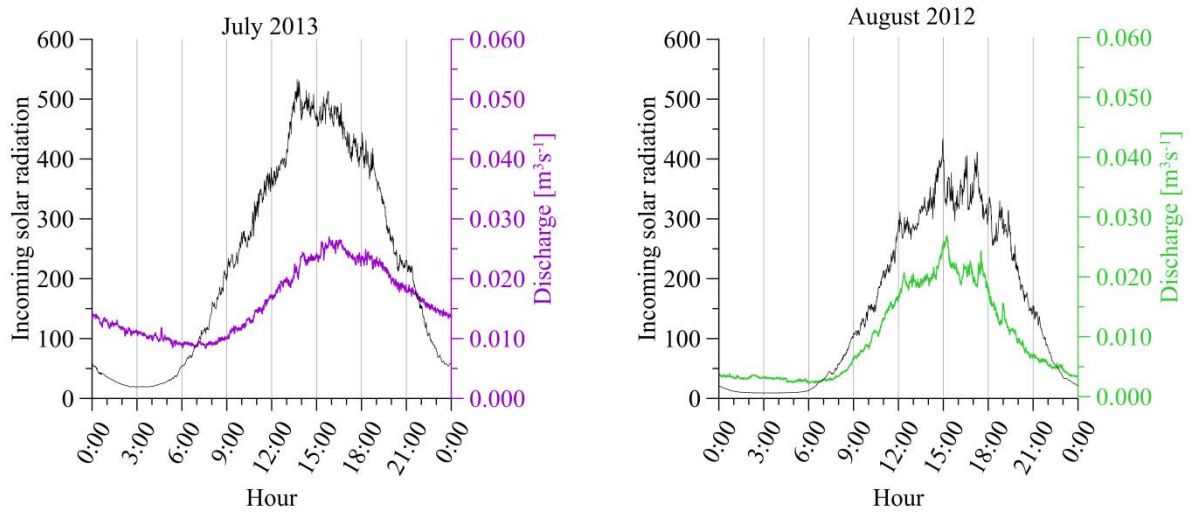

Figure 42. Incoming solar radiation and discharge volumes averaged over the 16-day observational periods of 2012 and 2013. July 2013 shows higher incoming solar radiation than August 2012. Similarly, discharge volumes are higher in July than August. The response time between an increase in incoming solar radiation and an increase in discharge volumes is slower in July 2013 than in August 2012. This is caused by the occurrence of snow in July and near absence of snow in August. In July meltwater has to infiltrate through the thick snowbanks before entering the sediment-meltwater channel leading to a longer erosion time. However, in August with the absence of snow, thawed permafrost can erode directly into the mud pool running into to the outflow channel.

In July, the early season, with considerable snowbanks, higher basal flow was observed at night. In August, in comparison, there was almost zero basal flow at night (Figure 42). Based on this observation it can be assumed that the snow banks continuously released meltwater during the night in July (Figure 43).

In July, discharge responded faster to increasing incoming solar radiation in the morning than to decreasing incoming solar radiation in the evening (Figure 43). Later in the season, in August, discharge responded faster than in July and there was little difference in the response times between morning and evening. Interestingly, on specific days (6, 8, 9, and 13 August 2012) the peak discharge occurred prior to the maximum incoming solar radiation (Figure 27).

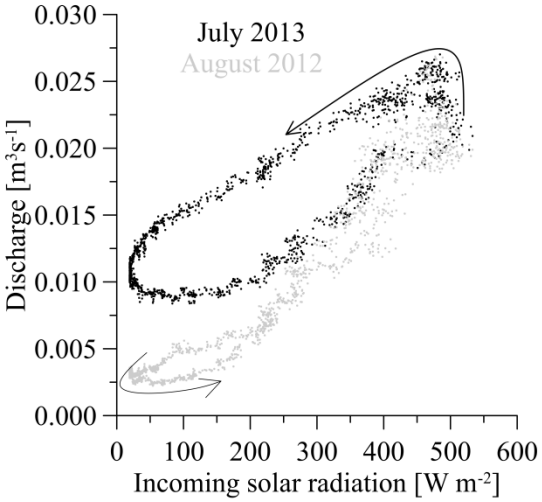

Figure 43. Discharge versus incoming solar radiation for the two field season:s July 2013 (black) and August 2012 (light grey). The 16-day averages show that discharge was higher in July 2013 than in August 2013. In July, the increase in incoming solar radiation in the morning led to increasing discharge and in the afternoon the discharge response was delayed due to the slower response of meltwater infiltration through the snowbanks. In August 2012, with negligible snowmelt, the data show a direct response of discharge to incoming solar radiation.

The seasonal influence of snowmelt on discharge is also reflected in the dissolution of the sediment-meltwater in the geochemical samples. Snow has an electrical conductivity of 4 to 10 µs cm^{-1} and the discharge in July had an average electrical conductivity of 1566 µs cm^{-1}; three times lower than what was measured in August 2012 (4420 µs cm^{-1}). In July, large amounts of thawed permafrost and snow eroded during the day and because of the longer snowmelt response time, also during the night. This can be seen in the lower electrical conductivities (Figure 31). From July to August the electrical conductivity increased due to the reducing contribution of snowmelt over the season. Electrical conductivity in August 2012 had no distinct diurnal variation, indicating no snowmelt contribution but rather just the effect of thawing permafrost.

Sediment concentrations also varied throughout the thawing season. In July the sediment concentrations were lower than in August (74 g l^{-1} in July versus 187 g l^{-1} in August). This is in part due to the contribution of snowmelt in July leading to higher discharge volumes, but also due to the growing contribution of thawing permafrost, which becomes more dominant in August. The lower values of dissolved organic and inorganic carbon in July show the effect of dissolution in snow meltwater. However, in terms of wt %, the total nitrogen, total inorganic carbon, and total organic carbon content in the sediment did not show obvious differences between seasons.

To reconstruct the amount of snowmelt eroded in July, two samples of the snow surface were taken in 250 ml sample bottles. The resulting meltwater volumes from both samples were 170 ml and 161 ml indicating snow densities of 68.0 % and 64.4 % water (680 kg m^{-3} and 644 kg m^{-3}). A simple estimation of the volume of water from snowmelt can be made using basic topographical information about the slump. The surface of the slump headwall that is eroding through the middle outflow channel and into the cut-throat flume is 23 617 m^2. Snow accumulation varied between 0 m, at the top of that headwall to 3 m near the bottom. By assuming an average snowpack thickness of 1.5 m and a density of 66 % water, one can estimate the volume of snowmelt. During the observational period, snow cover on the headwall decreased by 55 % from 90 % to 35 %. Therefore the following equation can be used to compute the volume of snowmelt:

$$\text{snowmelt volume} = \text{area} \times \text{snow thickness} \times \text{snow density} \times \text{snow retreat}$$

Snowmelt contributed about 12 859 m^3 in water volume to the outflow channel. While the estimation of this volume is not extremely accurate it puts into perspective the contribution of snow compared to that of the headwall. Hence, in July, snowmelt contributed more than half (56 %) of the total volume of 25 000 m^3 eroded, with the remaining contribution coming from ablation of the permafrost headwall (12 141 m^3). However, in August the total volume eroded was 15 600 m^3 and due only to thawing permafrost. This is in contrast to Lewkowicz (1987) who observed higher ablation values in August than in July on Banks Island in the Northwest Territories. His observations, however, were made only on exposed headwalls, not taking into account the influence of any snowbanks.

Discharge is therefore driven by snowmelt, thawed permafrost of the headwall (mostly melted ground ice) and rain. Based on the observations made over the two seasons of fieldwork, a few lessons can be drawn for the overall seasonal evolution of discharge in slump systems. A

schematic illustration showing the evolution and highlighting the contribution of snowmelt, thawed permafrost and rain is presented in Figure 44. Melted snow and thawed permafrost are overall the main contributors to discharge, although their contributions vary strongly over the thawing season. Rain only makes a minor contribution to sediment-meltwater discharge since it occurs infrequently, and when so not much rain falls (thin blue line at the bottom of Figure 44). Similarly, Lewkowicz and Young (1990) concluded that precipitation contributed less to discharge than the diurnal melt of the snowbank.

Based on the observations made, a best approach was established to estimate the evolution of the discharge volume over the June to mid-September thawing season (Figure 44). Up to now there are no records for the yearly start or end of sediment-meltwater release at Slump D. The thawing season in 2012 was from 6 June to 8 October and that of 2013 from 26 May to 27 September (Environment Canada). It is expected that snowmelt starts immediately or shortly after temperatures rise above 0 °C as observed at other locations in the Canadian Arctic (Lamoureux and Lafrenière, 2009, 2014). Snowmelt contributed largely to sediment-meltwater discharge. However, in August 2012 it can be assumed that there is only thawed permafrost of the headwall eroding into the sediment-meltwater channel. Highest discharge volume was measured on 8 July 2013 (2212 m^3 day^{-1}) and decreased throughout the season until 14 August (864 m^3 day^{-1}) (Figure 44). In the early thawing season discharge is largely caused by melting snow, with snowmelt contributing about half the water volume released in July 2013. Aerial oblique photography shows that the snow coverage of the headwall decreased from about 90 % on 5 July to about 35 % on 23 July 2013 (see Figure 14). In the later thawing season, in August, thawing permafrost becomes the main contributor to discharge (Figure 35).

Although no data are available for the end of the thawing season at Slump D, the evolution of climatic variables and past visual observations suggest that the thawing season ends in mid-September. Kerfoot (1969) observed that more than 80 % of the headwall retreat took place during July and August, meaning that less than 20 % of headwall ablation occurred after August. A photo of Slump D from 23 September 2003 taken after 6 days of air temperature at or below -1 °C (Environment Canada) shows no visible discharge (Figure 48). One can likely conclude that less than 20 % erodes after August and, based on climatic records, it can be reasonably assumed that the thawing season ends in mid-September, linked to the decrease in air temperatures and incoming solar radiation. This agrees with the assessment of Kerfoot (1969) who found that headwall retreat stops when temperatures reach below 0 °C.

Based on this information, a conceptual diagram was introduced showing the pace of discharge over the entire thawing season and the contribution of the different units to the outlet. Although this diagram was built with data from Herschel Island, it can be applied to any slump system, bearing in mind that the contribution of the different units may vary strongly based on the local and regional physical setting.

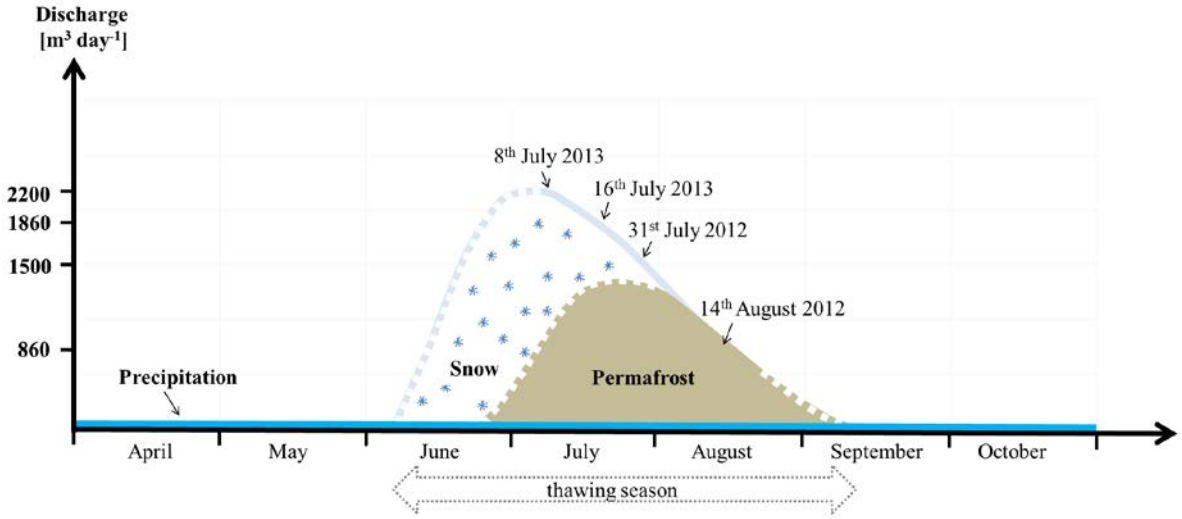

Figure 44. Schematic evolution of discharge during the thawing season at Slump D. Discharge likely starts in early-June with snowmelt (white) dominating the sediment-meltwater early in the season, while thawed permafrost (brown) dominates the sediment-meltwater from about the end of July onwards. The thawing season ends around mid-September. In July 2013, more than half of the released discharge volume originated from melting snowbanks, while in August of the same year the discharge volume consisted only of thawed permafrost. Throughout the season there is a constant but small contribution from precipitation (blue).

6.2. Contribution of Retrogressive Thaw Slumps to the Sediment Budget of the Yukon Coast

6.2.1. Origin of Outflow Material

Sediment-meltwater originates from the thawed permafrost headwall and snowmelt. The properties of the released material observed in this thesis are very similar to the ones published by other authors in the area.

Several samples of the headwall in Slump D were taken over the past eight years. In 2008, a complete profile of the headwall was analysed by Fritz et al. (2012). In 2012, samples were taken from the ice-rich permafrost in the head wall (Appendix 8.1.1). In August 2012, samples from the massive ground ice were taken by (Tanski, 2013; Table 5). In addition, snow samples were collected from snowbanks protecting the headwall in July 2013 (chapter 5.2.2).

These headwall samples varied greatly in ice content, electrical conductivity and dissolved organic carbon content (Table 5). The sediment-rich headwall samples were characterised by lower ice content (≥ 30 wt %) and very high electrical conductivity (< 14.610 µS cm^{-1}; Table 5). The massive ground ice samples were characterised by very high ice content (98 vol %), lower electrical conductivity (213 µS cm^{-1}) and low dissolved organic carbon content (2 mg l^{-1}).

The water content at the slump outlet was higher in the early thawing season (July), than in the late thawing season (August). Sediment-meltwater in July contained 96.6 % water and 92.6 % in August. This higher water content in the early thawing season is likely due to the additional snow contribution in July. In August, snow banks are already melted, which leads to lower water content. Nevertheless, even in August, water content was high, which indicates that a large portion of the water in both seasons derives from massive ground ice.

The geochemical characteristics of headwall (permafrost) samples were similar to the ones of the sediment-meltwater sampled at the slump outlet, though some isolated headwall samples showed much higher total organic carbon content. The headwall samples had an organic carbon content between 0.6 and up to 28.7 wt % (Table 5). The outflow samples had a total organic carbon content between 1.2 and 2.5 wt % (Figure 35). Total inorganic carbon samples of the headwall were between 0.5 and 2.2 wt %, and therefore similar to 0.6 to 1.5 wt % in the outflow. Organic-rich samples taken along the headwall had a total nitrogen range between

0.1 and up to 1.4 wt %, whichis in the range of 0.14 and 0.27 wt % measured in the outflow. In addition, $\delta^{13}C$ were -27.8 to -25.9 ‰ along the headwall and -26.3 and -26.4 ‰ in the outflow.

The snow present on the headwall led to dilution of eroding headwall material, which, in turn, led to a decrease in sediment concentration in the sediment-meltwater at the outflow (Figure 31 and Table 5). The contents of total organic carbon and total nitrogen in the sediment fraction were quite similar between seasons, but the contribution of snow led to reduced amounts of total organic carbon and total nitrogen in a given volume of sediment-meltwater in July 2013.

	Ice content	Electrical conductivity [µS cm^{-1}]	pH	Dissolved organic carbon [mg l^{-1}]	Dissolved inorganic carbon [mgl^{-1}]	organic carbon [wt %]	inorganic carbon [wt %]	nitrogen[wt %]	$\delta^{13}C$ [‰]	TOC/TN
snow July 2013	100%	4 and 10	6.4 and 6.5	0.4 and 0.5	0.1 and 0.2					
northern headwall August 2012	62-93 %					1.3 to 28.7	0.5 to 2.2	0.1 to 1.4	-27.8 to-25.9	10 to 22
headwall Fritz et al., 2012	≥ 30 wt %	136 to 14610				0.6 to 17.0		0.1	-26.6 to -25.9	11 to 23
massive ground ice Tanski, 2013	98 vol %	213	7.7	2						
outflow July 2013	97 % water	1566	7.7	9	25	1.8	1.0	0.2	-26.3	9
outflow August 2012	93 % water	4420	7.5	18	35	1.8	0.9	0.2	-26.4	10

Table 5. Geochemical characteristics of snow, headwall and outflow samples taken from 2008-2013. Outflow samples mainly result from headwall samples with ice- and organic-rich permafrost. Snow samples and massive ground ice indicate a dilution of outflow.

6.2.2. Slump D in the Regional Context

The headwall samples taken at Slump D and the ones from four other retrogressive thaw slumps along the Yukon Coast showed geochemical and sedimentological values in the same range (Figure 45 and Appendix 8.2). For the four other slumps, organic carbon varied between 1.0 and 13.8 wt %, total inorganic carbon between 0.6 and 3.1 wt %, and total nitrogen content between 0.1 and 1.9 wt %. Samples with total organic carbon greater than 4.2 wt % and total nitrogen greater than 0.3 wt % were located in the top organic-rich layer immediately below the tundra surface. The ice-rich permafrost underneath this layer had lower values of total nitrogen and total organic carbon. TOC/TN values of all thaw slumps were between 7.3 and 15, and $\delta^{13}C$ values between -28.0 and -25.8 ‰, very similar to the values observed at Slump D. This indicates that all samples originate from C_3 land plants and lacustrine algae (Figure 46). Grain size for the four thaw slumps is similar to the one of Slump D with sandy silt and clayey silt (Figure 47). The volumetric ice content of the ice-rich

permafrost samples was between 30 and 99 % (Figure 45). Organic-rich material (associated with organic carbon greater than 1.6 wt %) was only present in the top few (centi-) meters of the headwalls and made only a minor part of the exposed headwall. This is in accordance with observations at Slump D and shows that the knowledge gained in this thesis on the cryostratigraphy can be generalized at the regional scale and help to build regional budgets for the outflow of sediment-meltwater from slumps.

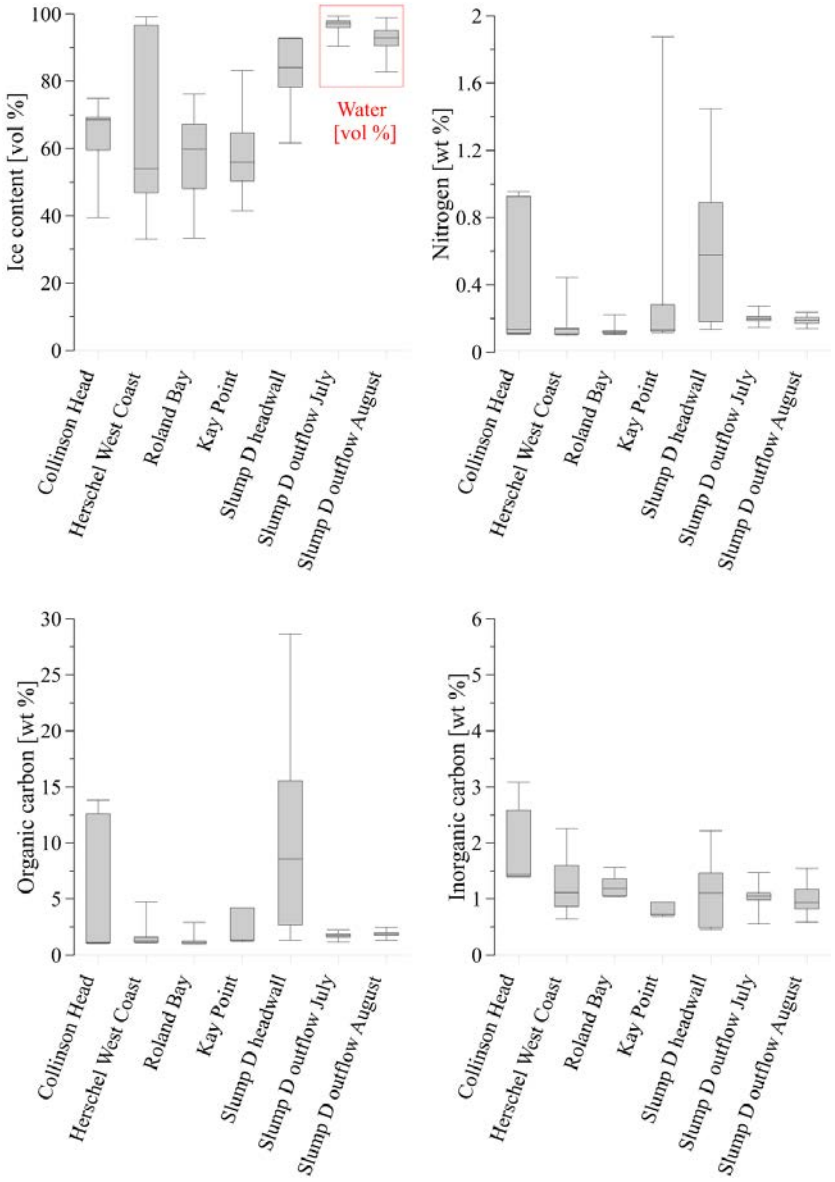

Figure 45. Ice content, total nitrogen, and total (in-) organic carbon content of five thaw slump headwalls compared to the sediment-meltwater of Slump D. The headwall samples were all taken in August 2012 and are from Collinson Head slump, Herschel Island West Coast slump, Roland Bay slump and Kay Point slump as well as the northern headwall of Slump D (Appendix 8.1). Volumetric ice contents of the five thaw slumps were greater than 33 vol %, total nitrogen reached up to 1.9 wt %, total organic carbon up to 28.7 wt % and total inorganic carbon up to 3.1 wt %. In both seasons sediment-meltwater samples of the Slump D outflow was in the range of these headwall samples.

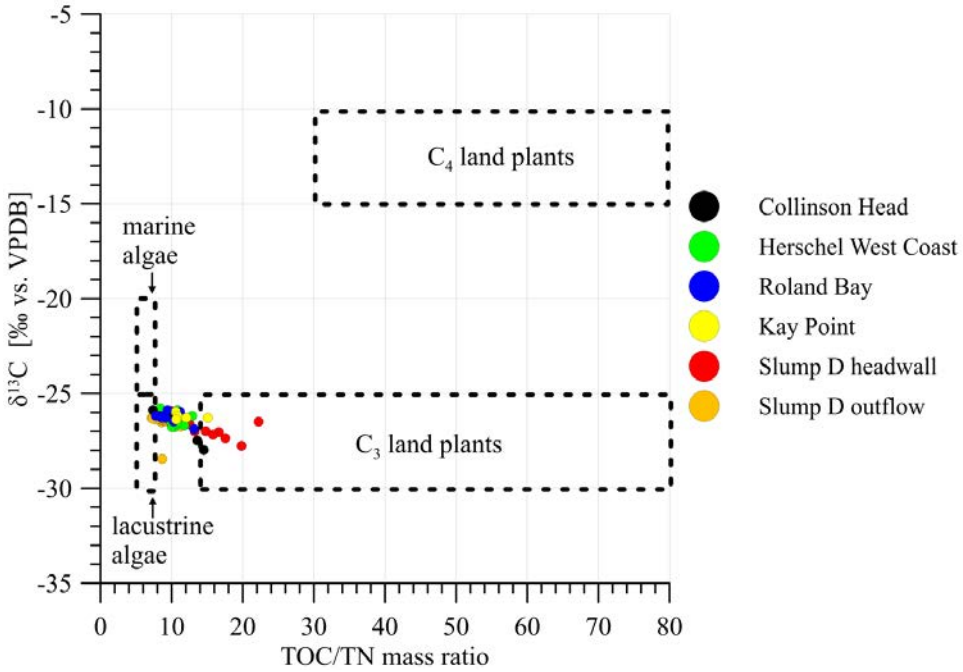

Figure 46. Total organic carbon and total nitrogen ratio (TOC/TN) compared to δ13C [‰ vs. VPDB] values. Samples were taken from the headwalls of Collinson Head slump, Herschel Island West Coast slump, Roland Bay slump, Kay Point slump, Slump D and Slump D´s outflow. The values indicate that the organic matter originates from lacustrine algae/C_3 land plants. Marine and lacustrine algae as well as C3 and C4 land plant classification are modified to TOC/TN mass ratio (modified after TOC/TN atomic ratio (Meyers, 1994) and Meyers (2003).

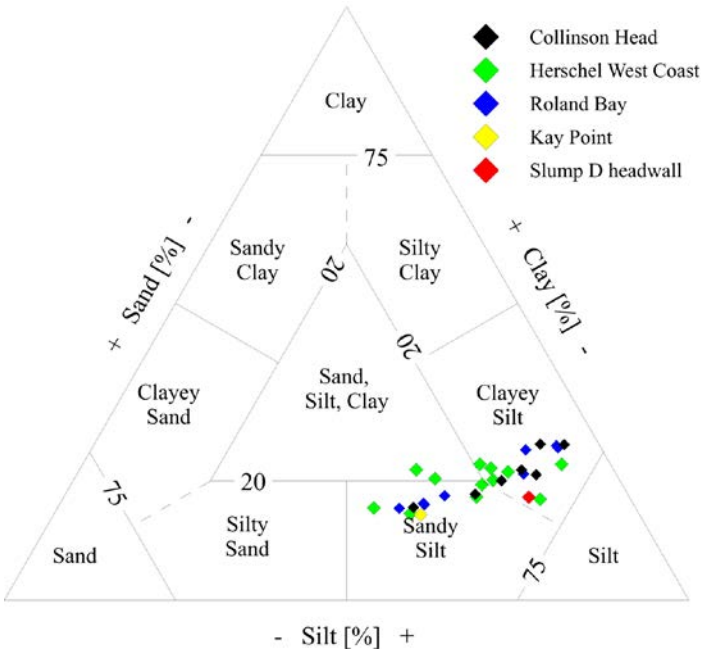

Figure 47. The sediment triangle after Shepard (1954) shows the grain size distribution between clay, silt and sand. Samples taken from the headwalls of Collinson Head slump, Herschel Island West Coast slump, Roland Bay slump, Kay Point slump and Slump D highlight a cluster in Clayey Silt and Sandy Silt. They show the same grain size distribution as the outflow samples of Slump D (**Figure 32**).

6.2.3. Seasonal Sediment Budget Compilation for Slump D

The data collected in this thesis is based on 36 days of measurements over two seasons. These measurements are used as a basis to compile outflow rates and quantities for the thawing season (early June-mid September). At Slump D, 25 000 m³ of sediment-meltwater were released over 18 days in late July (2013), and early August (2012) 15 600 m³ over 18 days, totaling a volume of 40 600 m³ over 36 days. The volume released is unknown beyond these two seasons. In order to compile outflow rates and volumes for the thawing season, the measurements were upscaled for the two months of July and August (62 days). June was not used for upscaling due to large uncertainties in terms of the start of the thawing season and ratio of snowmelt to thawed permafrost. September was also not included in the estimation due to very low air temperatures and unknown quantities of sediment-meltwater. In the upscaling of July and August, it was assumed that there was no diurnal or intra-seasonal variation. The two field seasons were combined and a daily average was calculated for the thawing season from 1 July to 31 August (Equation 1).

Equation1:

$$\text{outflow volume} = \frac{40600\text{m}^3}{36\ \text{days}} = 1127.8\ \text{m}^3\ \text{day}^{-1}$$

$$\text{outflow volume}_{(\text{July}-\text{Augst})} = 1127.8\ \text{m}^3\ \text{day}^{-1}\ \text{x}\ 62\ \text{days} = 69\,922\ \text{m}^3$$

An estimated daily average of 1128 m³ of sediment-meltwater was computed using this equation. This includes 141.9 t of sediment, 1.5 t of total inorganic carbon, 2.6 t of organic carbon, 0.27 t of total nitrogen, and 1072.1 t of meltwater with 14 kg of dissolved organic carbon (Table 6). The total sediment-meltwater volume for the entire July-August season was estimated to be 69 922 m². This amounts to 8796 t sediment including 91 t total inorganic carbon, 159 t organic carbon and 17 t total nitrogen released over 62 days. The water volume eroding in 62 days would then be 66470 m³, including 871 kg of dissolved organic carbon (Table 6). It is assumed that further sediment-meltwater is generated in June and mid-September. However, this was not recorded and therefore a minimum value for 1 July to 31 August is calculated.

	Outflow volume	Sediment concentration	Organic carbon	Inorganic carbon	Nitrogen	Water volume	Dissolved organic carbon
Mean 18 days July	0.016 m^3 s^{-2}	82 g l^{-1}	1.481 g l^{-1}	0.886 g l^{-1}	0.166 g l^{-1}	966 g l^{-1}	0.009 g l^{-1}
Total 18 days July [t]	25000 m^3	2050	37	22	4.14	24150	0.23
Mean 18 days August	0.010 m^3 s^{-2}	196 g l^{-1}	3.561 g l^{-1}	1.967 g l^{-1}	0.357 g l^{-1}	926 g l^{-1}	0.018 g l^{-1}
Total 18 days August [t]	15600 m^3	3058	56	31	5.57	14446	0.28
Slump D 36 days [t]	40600 m^3	5108	93	53	9.71	38596	0.51
Mean per day [t]	1128 m^3	142	3	1	0.27	1072	0.01
Slump D 62 days [t]	69922 m^3	8796	159	91	16.72	66470	0.87
Thaw slumps Yukon Coast [t]	1367674 m^3	172058	3119	1779	327	1300157	17

Table 6. Sediment-meltwater composition of Slump D with mean and total values of both field seasons upscaled to 62 days (July and August), and for all thaw slumps along the Yukon Coast. The outflow volume was calculated with the sediment concentration including total (in-) organic carbon and total nitrogen. In addition, a water volume with dissolved organic carbon was determined.

6.2.4. Retrogressive Thaw Slump Occurrence along the Yukon Coast

Slump D is similar to other thaw slumps along the Yukon Coast from a cryostratigraphical and geochemical perspective (chapter 6.2.2). In this section, a simple spatial upscaling approach is used to generalize the slump outflow observations from Slump D to the Yukon Coast. Using several remote sensing datasets spanning several decades, J. Ramage (2016, personal communication) generated spatial statistics on retrogressive thaw slumps along the Yukon Coast. This dataset is used in the upscaling calculation.

Thaw slumps cover approximately 4 % of the Yukon Coast and have been increasing in number since 1952. In 2011, 229 thaw slumps were active along the Yukon Coast with a median area of 0.15 ha and a total area of 159 ha. Slump D is the largest thaw slump along the Yukon Coast, with the northern upper headwall and southern lower headwall totalling a size of 20.8 ha (2016, personal communication J. Ramage). Slump D is therefore 138 times larger than the median thaw slump size for the Yukon Coast. The catchment of Slump D is 8.13 ha (Obu et al., 2016b), which alone represents about 5.11 % of the total area of active thaw slumps along the Yukon Coast.

Ideally one would use the surface area of the thaw slump headwalls to accurately upscale the sediment-meltwater release for the Yukon Coast. However, only the total surface area exists of the active slumps (159 ha) and therefore the value was upscaled from Slump D (8.13 ha) to obtain a regional estimate. In total the Yukon Coast thaw slumps erode about 20 times the outflow of Slump D during the July-August thawing period (62 days). This results in a total erosion of 1 367 674 m^3 sediment-meltwater (Table 6), containing 172 058 t of sediment including 1 779 t of total inorganic carbon, 3 119 t of total organic carbon and 327 t of total

nitrogen. The total outflow would include 1 300 157 m³ of water with 17 t dissolved organic carbon.

6.2.5. Input to the Beaufort Sea

Most sediment and geochemical budgets for the Beaufort Sea include the contribution from rivers and coastal erosion but have failed to include retrogressive thaw slumps. This section aims to highlight the contribution of thaw slumps to the Beaufort Sea system.

Mackenzie River

The largest contribution of freshwater and sediment to the Beaufort Sea comes from the Mackenzie River (Hill et al., 1991). The Mackenzie River, with a basin area of 1.78 Mio km², has a discharge of approximately $3.3 \cdot 10^{11}$ m³ a^{-1} and an annual inorganic sediment supply of $127 \cdot 10^{6}$ t a^{-1}. The estimate of particulate organic carbon is $2.1 \cdot 10^{6}$ t a^{-1} and dissolved organic carbon is $1.3 \cdot 10^{6}$ t a^{-1} (Macdonald et al., 1998). On the Canadian Beaufort Sea shelf, 95 % of the sediment supply originates from the Mackenzie River. Other rivers along the Yukon coast contribute about $1.45 \cdot 10^{6}$ t a^{-1} of sediment (Hill et al., 1991). Macdonald et al. (1998) estimate $0.02 \cdot 10^{6}$ t a^{-1} of organic carbon input from other rivers.

The sediment-meltwater release from Slump D is very small in comparison to the annual outflow volume of the Mackenzie River. The ratio between the two is greater than 1:8Mio and 1: 2.5 Mio for dissolved organic carbon (Table 7). The ratio for sediment is smaller (1:25 000), which can be explained by the very large sediment content observed in thaw slump meltwater (up to 457 g l^{-1} in Slump D). The ratio for organic carbon is also smaller (1:23 000), because most of it is in particulate form and therefore bound to the sediment.

	Slump D (36 days)	Mackenzie River	Ratio
Outflow volume	40600 m³	$3.3 \cdot 10^{11}$ m³	1:8128079
Sediment	5107.60 t	$127 \cdot 10^{6}$ t	1:24863
Organic carbon	92.58 t	$2.1 \cdot 10^{6}$ t	1:22581
Nitrogen	9.71 t		
Dissolved organic carbon	0.51 t	$1.3 \cdot 10^{6}$ t	1:2549020

Table 7. Ratio between the annual outflow volume of the Mackenzie River and the 36-day observations from Slump D. The area of the Mackenzie River basin is 1.78 Mio km², whereas the catchment of Slump D is only 0.136 km². The ratios illustrate the large outflow volumes from the Mackenzie River compared to Slump D. Sediment and organic carbon ratios are smaller, highlighting the high sediment concentration of Slump D´s sediment-meltwater.

Slump D represents only 5.11 % of the total thaw slump area of 159 ha along the Yukon Coast. However, when comparing the total of all thaw slumps with the Mackenzie River, their contribution is very small (Table 8). The outflow volume of the Mackenzie River is still more than 73 000 times larger. Additionally, the sediment and organic carbon ratios are still 1:738 and 1:673.

	Slumps Yukon Coast	Mackenzie River	Ratio
Outflow volume	1367674 m^3	$3.3 \cdot 10^{11}$ m^3	1:73117
Sediment	172058 t	$127 \cdot 10^6$ t	1:738
Organic carbon	3119 t	$2.1 \cdot 10^6$ t	1:673
Nitrogen	327 t		
Dissolved organic carbon	17 t	$1.3 \cdot 10^6$ t	1:76471

Table 8. Ratios of outflow and geochemical composition of all thaw slumps along the Yukon Coast and their contribution from 1 July to 31 August compared to the annual values of the Mackenzie River. The Mackenzie Riverinput is considerably larger compared to the contributions from the thaw slumps.

Kuparuk River

Even for a smaller river such as the Alaskan Kuparuk River, which has a basin area of 8 000 km^2, the outflow volume and the dissolved organic carbon from Slump D is about 30 000 times smaller (Table 9). However, with an organic carbon ratio of only 1:19, the impact of Slump D is large compared to the Kuparuk River (McGuire et al., 2009).

	Slump D (36 days)	Kuparuk River	Ratio
Outflow volume	40600 m^3	$1.2 \cdot 10^9$ m^3	1:29557
Sediment	5107.60 t		
Organic carbon	92.58 t	1800 t	1:19
Nitrogen	9.71 t		
Dissolved organic carbon	0.51 t	14000 t	1:27451

Table 9. Ratio between the 36-day outflow volume from Slump D and the annual outflow from the Kuparuk River, Alaska. The area of the Kuparuk River basin is 8 000 km^2 and therefore is much larger compared to Slump D (catchment area of 0.136 km^2). However, the high sediment concentration of the sediment-meltwater of Slump D leads to an organic carbon ratio of only 1:19.

The outflow volume from the Kuparuk River is 877 times larger than the total of all thaw slumps (Table 10). However, the Yukon Coast thaw slumps contribute twice as much organic carbon to the Beaufort Sea than the Kuparuk River.

	Slumps Yukon Coast	Kuparuk River	Ratio
Outflow volume	1367674 m^3	$1.2 \cdot 10^9$ m^3	1:877
Sediment	172058 t		
Organic carbon	3119 t	1800 t	2:1
Nitrogen	327 t		
Dissolved organic carbon	17 t	14000 t	1:824

Table 10. Ratios between the Yukon Coast thaw slumps and the Kuparuk River. The outflow volume and dissolved organic carbon ratios are very high. However, the organic carbon ratio shows that the Yukon Coast thaw slumps contribute twice organic carbon from [t] July to 31 August compared even to the annual total from the Kuparuk River.

Yukon Coast Erosion

The sediment release from Slump D is also small in comparison to coastal erosion along the Yukon Coast (Table 11). In 1991, Hill *et al.* reported that erosion along the Canadian Yukon Coast supplies $5.62 \cdot 10^6$ t a^{-1} of sediment to the Beaufort Sea (Hill et al., 1991). The coast is also thought to release $0.04 \cdot 10^6$ t a^{-1} of soil organic carbon (Couture, 2010) and a minimum of 54.9 t a^{-1} of dissolved organic carbon solely from massive ground ice (Tanski et al., 2016). Furthermore, these numbers may have increased as erosion rates have increased. On Herschel Island, the rates were 0.61 m a^{-1} from 1952-1970 and 0.45 m a^{-1} from 1970-2000 (Lantuit and Pollard, 2008). Obu et al. (2016a) showed a 50 % increase of coastal erosion for the period 2000-2011. The ratio between annual mean erosion from the Yukon Coast and that from the 36-day observational period from Slump D is 1:1000, while the ratio for total organic carbon ratio is smaller at 1:430 (Table 11). The ratio of 1:108 for dissolved organic carbon is most likely bigger, since the value of 54.9 t is obtained just from the massive ground ice and does not include the contribution from the organic-rich permafrost (Tanski et al., 2016), which would increase the ratio further.

	Slump D (36 days)	Yukon Coast erosion	Ratio
Outflow volume	40600 m^3		
Sediment	5107.60 t	$5.62 \cdot 10^6$ t	1:1100
Organic carbon	92.58 t	$0.04 \cdot 10^6$ t	1:430
Nitrogen	9.71 t		
Dissolved organic carbon	0.51 t	54.90 t	1:108

Table 11. Ratios between Slump D in 36 days and the annual erosion rates from the Yukon Coast. The ratio of dissolved organic carbon is likely much larger as the value of the Yukon Coast of 54.90 t is solely from massive ground ice and does not include organic rich permafrost.

It becomes even clearer that thaw slumps matter when comparing their total contribution with that from the entire Yukon Coast (Table 12). Thaw slumps contribute an additional 172 058 t (3 %) of sediment and 3119 t (8 %) of organic carbon to the Canadian Beaufort Sea. The 55 t of dissolved organic carbon from the Yukon Coast is likely an underestimate, again because the contribution from organic-rich Permafrost is not taken into account. This would thus increase the ratio considerably.

	Slumps Yukon Coast	Yukon Coast erosion	Ratio
Outflow volume	1367674 m^3		
Sediment	172058 t	$5.62 \cdot 10^6$ t	1:33
Organic carbon	3119 t	$0.04 \cdot 10^6$ t	1:13
Nitrogen	327 t		
Dissolved organic carbon	17 t	55 t	1:3

Table 12. Ratios between the Yukon Coast thaw slumps and erosion from the Yukon Coast illustrate the large contribution from thaw slumps. The slumps contribute an additional 172058 t of sediment (3 %) and 3119 t of organic carbon (8 %) into the ocean, while 17 t of dissolved organic carbon are released into the nearshore zone. The ratio is likely larger since the 55 t dissolved organic carbon from coastal erosion is estimated just from the massive ground ice and does not include the contribution from organic-rich permafrost.

West River

The West River at Cape Bounty, Canada, which has a watershed of 8 km^2, generates discharge only when snow melts, usually from mid-June to mid-July (Favaro and Lamoureux, 2014; Lamoureux and Lafrenière, 2014). Although the area of the West River is 100 times larger than Slump D, the discharge is just 20 times larger. Sediment yield, total organic carbon, and total nitrogen from the West River are 27, 47, and 33 times smaller than from Slump D, respectively (Table 13). The impact of Slump D over the 36-day observational period is thus considerable compared to the West River at Cape Bounty.

	Slump D (36 days)	West River	Ratio
Outflow volume	40600 m^3	831200 m^3	1:20
Sediment	5107.60 t	184.00 t	27:1
Organic carbon	92.58 t	2.19 t	47:1
Nitrogen	9.71 t	0.29 t	33:1
Dissolved organic carbon	0.51 t		

Table 13. Ratio of outflow volume and sediment release between Slump D and West River, Cape Bounty, Canada. The water shed of West River is 8 km^2 and discharge is only recorded during snowmelt from mid-June until mid-July. The data from Slump D cover a period of 36 days in July and August, from a catchment area of just 0.136 km^2.

In summary, thaw slumps release large quantities of freshwater, sediment, organic carbon, and nitrogen. However, compared to the Mackenzie River, with a basin area of 1.78 Mio km² and which is the largest source of outflow material into the Beaufort Sea, the contribution from thaw slumps is small. Even compared to the Kuparuk River in Alaska, with a basin area of 8 000 km², the discharge and dissolved organic carbon flux is small. However, the thaw slumps along the Yukon Coast contribute twice as much organic carbon to the ocean than the Kuparuk River. Comparing small watersheds, such as the West River at Cape Bounty, it is clear that Slump D and other thaw slumps contribute large amounts of sediment, organic carbon and nitrogen locally. Their contribution may even be larger given the conservative upscaling approach used here, which does not include the contribution from the early and late thawing season (June and September).

6.3. Projected Climatic Change and its Impact on Retrogressive Thaw Slump Outflow

In the Arctic, future climate is projected to change substantially (Collins et al., 2013), potentially leading to an increase in the erosion rate of retrogressive thaw slumps (Kokelj et al., 2009; Lantuit et al., 2012b; Lantz and Kokelj, 2008). Along the Yukon Coast, changing oceanic conditions may also lead to increased coastal erosion (Lantuit et al., 2012a). This may have large consequences for the removal of thaw slump material and lead to an increase in erosion rate of retrogressive thaw slumps, particularly since the growing frequency of retrogressive slumps has already been partly be attributed to wave erosion (Lantuit and Pollard, 2008; Lantuit et al., 2012b). Future projections also show an increase in ocean temperatures and sea level rise of up to 16 mm a-1 by 2100, as well as a longer open-water season along the coast which could reinforce the effect of wave erosion on slump initiation (Church et al., 2013).

In addition, rising air temperatures may lead to an increase in the rate of ablation of the headwall in retrogressive thaw slumps. Arctic surface air temperatures have been steadily increasing over the past decades (Johannessen et al., 2004) and are projected to increase by up to 8.3 ± 1.9 °C by 2081-2100 relative to 1986-2005 (Collins et al., 2013). Along the Yukon Coast, summer temperatures (June-August) are projected to increase by 2-3 °C by 2100 (again, compared to the 1986-2005 temperatures; Collins *et al.*, 2013). On Herschel Island, a trend towards increasing temperatures is already apparent (Table 2). Burn and Zhang (2009) showed similar trends using data from neighboring weather stations. Since 1900, mean annual surface air temperatures on Herschel Island increased from -12.0°C (1900-1905) to -8.2 °C (2009-2014) with a prolonged thawing season from 100 to 121 days and an increase of thawing-degree days from 499 °C to 818 °C. The resulting input in heat to the surface of the headwall could lead to much greater ablation and hence to much greater outflows from retrogressive thaw slumps.

In order to test the impact of changing climatic conditions on slump discharge, a warming scenario was developed using field data from July 2013 and August 2012 in equation 1 (chapter 5.1.6). Future discharge was simulated under warmer surface air temperature with an increase of 2.0 °C, 3.0 °C, 4.0 °C, 6.0 °C and 8.0 °C. In these scenarios, incoming solar radiation and wind speed were kept constant to ensure that only the effect of air temperature was taken into consideration. The results show that a summer air temperature increase of 2.0 °C would lead to an increase of 109 % in total volume of sediment-meltwater released

during July and August (Table 14). Temperature increases of 3.0 °C, 4.0 °C, 6.0 °C and 8.0 °C would lead to 114 %, 118 %, 127 % or even 136 % more sediment-meltwater release from the slump, respectively (Table 14). Since projections using the IPCC RCP 4.5 scenario (Collins et al., 2013) anticipate a warming of summer air temperature in the range of 2-3 °C, one can reasonably expect an increase in outflow of 109-114 %. This projection is in accordance with the assumption by Séjourné et al. (2015) that an increase in air temperature will lead to an increase in thaw slump development. This scenario is also fairly conservative, since the months of June and September are not taken into account. A prolonged thawing season would increase the overall volume of sediment-meltwater to be released through the early loss of the protective snow cover on the slump headwall.

Mean surface air temperature of the field season July 2013 and August 2012 [°C]	+2.0	+3.0	+4.0	+6.0	+8.0
Increase in sediment-meltwater volume respectively to field season in July 2013 and August 2012 [%]	109	114	118	127	137

Table 14. Surface air temperature recorded during the field season of July 2013 and August 2012 increased by a hypothetical amount of up to 8.0 °C to calculate the increase of discharge under potential changing climatic conditions.

Of course, slump outflow not only depends on air temperature as shown in sections 5.1.5 and 5.1.6. Several other factors contribute to alter the total volume of sediment-meltwater released from slumps, including incoming solar radiation, which is one of the principal drivers of ablation and therefore also discharge. Long-term variations in incoming solar radiation are primarily associated with changes in cloud cover. However, cloud cover is challenging to predict and model projections of cloud cover changes in the Arctic remain highly uncertain. Some studies anticipate an increase in Arctic cloud cover (Vavrus et al., 2009), which would lead to a decrease in incoming solar radiation (Screen and Simmonds, 2010) and may lower the eroding discharge from the thawing ice-rich permafrost headwall, and decelerate retrogressive thaw slump progression. Nevertheless, cloud cover changes in June-August are projected to increase by just 1 % by 2081-2100 relative to 1961-1980 (Chen et al., 2011).

In order to assess the impact of a potential decrease in incoming solar radiation on the amount of sediment-meltwater released from Slump D in July and August, equation 1 was used with an input in incoming solar radiation reduced by 1 %, 2 % and 5 %. The results show that an increase in cloud cover would lead to a decrease of sediment-meltwater volume of 0.47 %,

0.95 % or even 2.40 % for the three scenarios, respectively (Table 15). This confirms the negligible role that variations in cloud cover would play in comparison to air temperature changes.

Mean incoming solar radiation of the field seasons July 2013 and August 2012 [%]	-1	-2	-5
Decrease of sediment-meltwater volume respectively to field season in July 2013 and August 2012 [%]	0.47	0.95	2.40

Table 15. Mean incoming solar radiation recorded during the field season of July 2013 and August 2012 decreased by a hypothetical amount of 1 %, 2 % and 5 % (1 % = 2.03 Wm-2). The sediment-meltwater volume is estimated to decrease by 0.47 %, 0.95 % and 2.40 %, respectively.

Precipitation is also expected to change in the Arctic and could contribute to changes in the amounts of sediment-meltwater released from thaw slumps. In summer, retrogressive thaw slumps in the lower Mackenzie and Peel Rivers are sensible to strong rainfall events, which can trigger mass mobilization of sediment and water (Kokelj et al., 2015). Slump D showed rainfall that led to heightened discharge, but sediment-meltwater samples did not have higher sediment concentrations, therefore there was little indication of additional mass mobilization as the ones observed by Kokelj et al. (2015). This may be because precipitation events are much smaller on Herschel Island. In the Arctic, precipitation is expected to increase with increasing surface air temperature (Collins et al., 2013; Rawlins et al., 2013). This could lead to an increase in occurrence and intensity of rainfall events, which may accelerate the release of sediment-meltwater at Slump D as rainfall quantities increase to resemble the ones observed at more southern locations.

In winter, an increase in precipitation may also lead to an increase in snow accumulation on Herschel Island. This increased snow accumulation may contribute to a slow-down of the headwall ablation and the release of sediment-laden meltwater early in the season. This process, however, is limited by the geometry of snow accumulation in the slump. Snow often accumulates in sinks on the tundra surface. Additional snow in winter would not necessarily result in more snow accumulation in the slump, as this “niche” along the headwall can only hold a limited amount of snow before the wind moves it away from the slump surface. This limitation is well illustrated in Figure 48, which shows large quantities of snow accumulation on the headwall, but also shows the role of wind preventing further accumulation of snow once the snow surface reaches the top of the headwall.

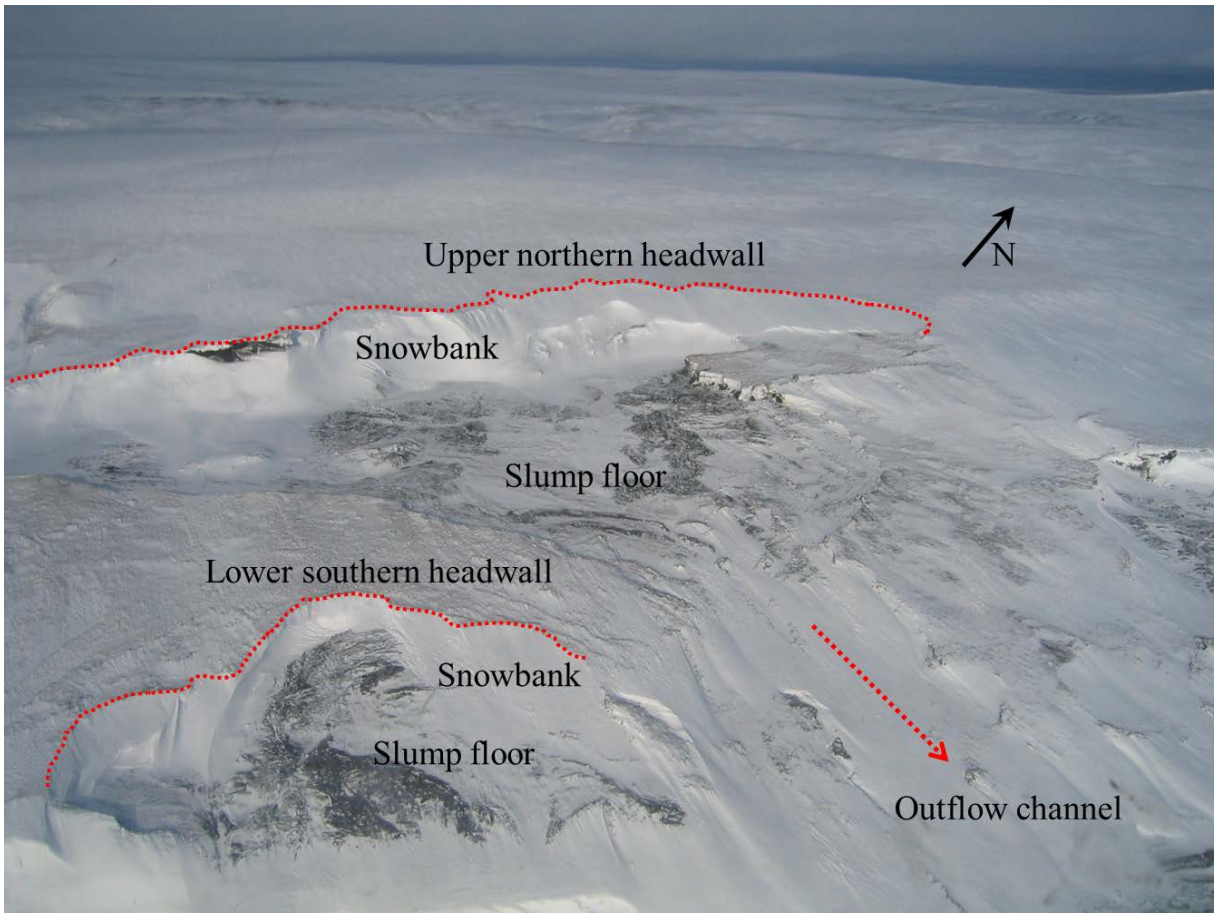

Figure 48. Aerial oblique photo of Slump D taken on 23 September 2003. Snow accumulation along the upper northern and lower southern headwall may have reached the maximum snow volume as the wind prevents further snow accumulation once the snow had reached the top of the headwall.

In summary, a future scenario with an increase in air temperature would lead to an increase in the amount of discharge primarily through the growing contribution of thawing permafrost. This scenario is presented in a schematic illustration in Figure 49. An increase of cloud cover may lead to a decrease in incoming solar radiation. However, as shown in Table 15, the resultant sediment-meltwater volume would decrease only by a negligible amount. This indicates that the main microclimatic cause for a potential future change in sediment-meltwater volume is increasing air temperatures. Warmer air temperatures may lead to an earlier onset of the thawing season and a later end of the season. The prolonged exposure of the permafrost headwall would lead to an increase in sediment-meltwater over the thawing season. It is expected that snow volumes are similar to current snow accumulation along the headwall during winter, which would lead to an earlier exposure of the permafrost headwall. In addition, an increase in air temperatures may lead to an additional increase in sediment-meltwater volume on warm summer days (Table 14). Increases in summer air temperatures of 2-3 °C may lead to an additional discharge volume increase of up to 114 % in July and

August (Table 14). However, this is a conservative approach and future total sediment-meltwater volumes are likely to be much larger over the thawing season due to the prolonged thawing season as well as the projected increase in rainfall leading to increases in mass mobilization.

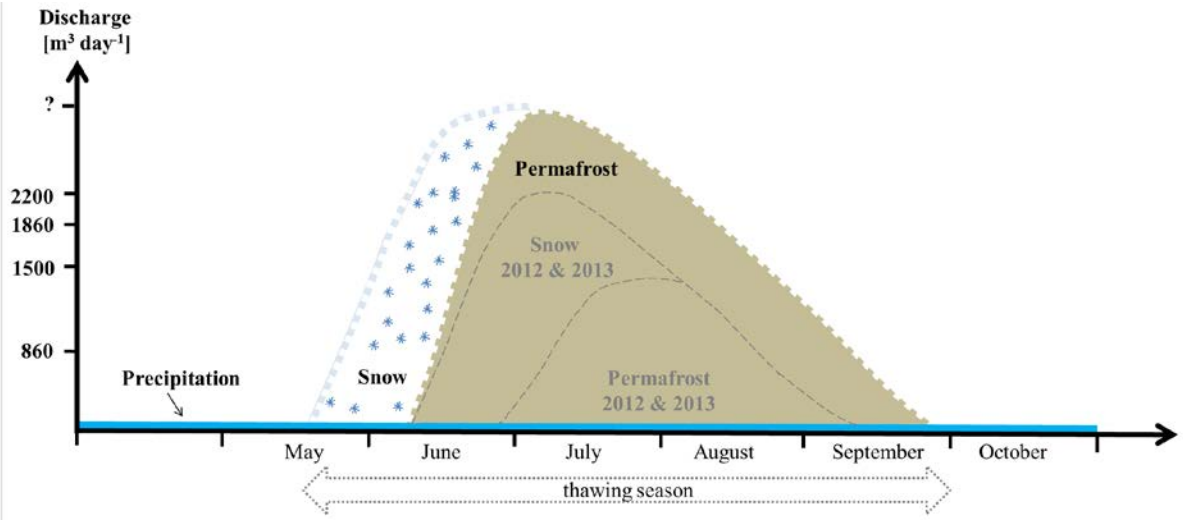

Figure 49. Schematic of future discharge volume during the thawing season at Slump D with higher air temperatures. The thawing season may start earlier, i.e. mid-May (instead of early-June) and may come to an end later, late-September (instead of early-September). Discharge volumes are dominated by snowmelt (white) in the early thawing season, while thawed permafrost (brown) dominates the sediment-meltwater from about the end of June onwards. An increase in air temperatures may lead to an increase in discharge volume of more than the maximum observed in July 2013 (2200 m³ day-1) and higher total discharge volumes over the entire thawing season. As for the historical period, there is a constant contribution from rainfall (blue) throughout the season.

6.4. Uncertainties and Limitations

One of the main uncertainties in the analyses described in the above sections relates to the incomplete coverage of the thawing season. The data used in this study to investigate the relationship between microclimatic forcing and sediment-meltwater discharge covered just 36 days. They do not capture the entire span of climatic conditions during the thawing season from early-June until mid-September, but only the core of the season in July and August. It is therefore not possible to accurately estimate the sediment-meltwater transfer over the whole season, without having a constant observational record or at least aerial oblique images from the beginning until the end of the thawing season.

As discussed in chapter 5.1.5, one of the factors controlling sediment-meltwater dynamics is air temperature. Large fluctuations in air temperatures were recorded especially between 2012 and 2013 (Table 2). Between 2009 and 2014 mean air temperatures in July varied from 8.2 °C to 10.0 °C. However, the year 2012 showed much higher temperature values in July with a mean of 15.0 °C. This allowed the snow to melt almost completely in the slump before field work was conducted in August. In addition, August 2012 was characterized by higher mean air temperatures of 11.8° C compared to the range observed from 2009-2014 (6.1 °C to 9.3 °C). The year 2012 was therefore an exceptionally warm year with a record in thawing-degree days of 1233.4 °C. This is more than 1.5 times the number of thawing-degree days usually observed over the same period. As the climatic conditions in the 2012 deviated considerably from the recorded means, constraints arise regarding the interpretability of drainage system evolution and total discharge volume during the summer season.

Another uncertainty to be taken into consideration, was the highly dynamic slump geomorphology (see chapter 5.1.1 for more details). Slump D had three sediment-meltwater channels of which only the middle one was monitored. In July 2013 and August 2012, 88 % of the upper headwall eroded into the middle outflow channel (Figure 5). However, the three sediment-meltwater channels and sub-surface channels were not stable throughout the season. The southern part of the upper headwall may also have drained into the unequipped southern outflow channel with large mud avalanches. Sediment-meltwater fluxes captured in this study may therefore be an underestimate of the total volume released throughout the field season. Nevertheless, the observations provide a minimum volume for the upper northern headwall of Slump D.

Uncertainties and limitations also stem from the instrumentation of the discharge station. The cut-throat flume designed by Skogerboe et al. (1972)was originally constructed for water. However, in this study it was used to measure water with very high sediment loads up to 457 g l^{-1}. It is not known whether this high sediment-load led to a change in coefficients in the discharge calculation (chapter 4.1.5). The same may be true for the ISCO water sampler, which is designed only for water with a suspended sediment load (4.1.7). Despite these uncertainties and challenges, the equipment used permitted the best possible measurements and sample collection.

Finally, grain size samples analysed were limited to the strainer size of 5 mm and the samples studied in the laboratory to < 1 mm. Observations identified boulders transported in the sediment-meltwater channel as well as large mass movements, such as the mud avalanche observed on 16 August 2012, which released large boulders and sediment-meltwater volumes. Moreover the volume of these mud avalanches remains completely unknown and may contribute much larger sediment-meltwater amounts than the recorded discharge volumes during the two field seasons.

6.5. Future Research

Long-term monitoring is vital to assess and fully understand the evolution of retrogressive thaw slumps. The Slump D survey record dates back to 1952, providing incredible evidence of past and current growth rates (Lantuit and Pollard, 2005). Considering projected future climate change, it is particularly important to continue long-term monitoring to understand the impact of future changes. DGPS and LiDAR measurements are recommended throughout the thawing season, not only for Slump D, but also at other thaw slumps. This would increase the accuracy of calculating the amount of the discharge volume eroding from retrogressive thaw slumps and to record their evolution under climate change.

In addition, future research should focus on the total thawing season and its sediment-meltwater release, especially at the beginning and the end of the thawing season. Currently, it is presumed that more than 80 % of ablation takes place in July and August (Kerfoot, 1969). Repeated measurements throughout the thawing season, with DGPS (2-D) for the headwall retreat or even better with LiDAR (3-D) for the headwall surface area retreat, would allow quantifying the volume of headwall ablation and accurate estimation of the seasonal evolution of ablation. Furthermore, it would enable a better understanding of sediment-meltwater transportation processes and volumes eroding from the headwall into the ocean.

Future studies should also focus on the fate of organic carbon and nitrogen after it is released from thawing permafrost. Vonk et al. (2012) showed that 66 % of the organic carbon stored in permafrost is released into the atmosphere as CO_2 upon thaw in an exposure in eastern Siberia. This estimate remains highly uncertain and requires further observational studies to confirm not only whether this is the case, but also whether such values are regionally representative. In addition, knowledge about the organic carbon lability on land and in the ocean is necessary. Studies should also consider the impact of sediment-meltwater release into the ocean, since it leads to increased loads of sediment and organic material, which may in turn have large consequences for the algae and phytoplankton populations and thus on the carbon cycle (Retamal et al., 2008). Further research on the release of sediment-meltwater from retrogressive thaw slumps should also include dissolved nitrogen measurements, as this may be an important additional source in the nitrogen cycle.

Several recent studies have measured the total area affected by retrogressive thaw slumps. However, to better put Slump D´s discharge study into perspective, it would be necessary to also know the headwall surface area of other thaw slumps. This would allow better estimation

of the sediment-meltwater release of thaw slumps into the environment. Further, additional discharge studies in other regions are necessary to compare the sediment-meltwater process of Slump D to establish how representative it is and how accurate upscaling to the regional level can be.

Retrogressive thaw slumps are increasing in number and size (Kokelj et al., 2015; Lantuit and Pollard, 2005; Lantuit et al., 2012b; Lantz and Kokelj, 2008). They are a growing threat for infrastructure, especially for roads such as the Alaskan Highway (Huscroft et al., 2004; Malenfant-Lepage et al., 2014). For example, subsidence of the road bed and cracks were observed in close vicinity to the approaching Takhini River thaw slump on the Yukon Plateau. Studies looking at how to slow down retreat rates or even to bring thaw slumps to a complete standstill, should become a focus in future. Since one of the major triggers for slumping is the thawing of the ice-rich permafrost headwall, there exist several options to protect the headwall and potential damage to expensive infrastructure such as roads. These include covering the headwall with tarpaulin and sediment or re-vegetating the headwall. Such interventions need to properly assessed to determine which are most effective in particular environments as they are likely to become more and more necessary as climate change continues to affect the Arctic region.

7. Conclusion

Retrogressive thaw slumps are sensitive to climatic conditions and are known to release large amounts of thawed permafrost to the environment. Thawed permafrost consists of meltwater and sediment including high amounts of organic carbon and nitrogen which may have a strong impact on the local ecosystem and global climate.

This study of Slump D on Herschel Island (Yukon Territory, Canada) provides data about the various factors controlling sediment-meltwater release, quantifies the amounts of sediment-meltwater (including organic carbon and nitrogen) released and estimates future projections of thaw slump evolution in a changing climate. The following results can be concluded:

- On Herschel Island, air temperature increased since 1900 when the first measurements were taken by settlers, who found that annual air temperature was -12 °C (average 1900-1905). Since 1994, air temperatures have been measured by an automatic weather station and show an increase in annual air temperature from -9.2 °C (1995-1997) to -8.2 °C (2009-2014) and an increase of mean annual thawing degree days from 711 °C to 818 °C. The year 2012 had an exceptionally warm summer, with 1233 °C thawing degree days (Table 2).

- Slump D is the largest retrogressive thaw slump along the Yukon Coast (Canada) with a lateral width of more than 500 m, a headwall height of up to 16 m, and an annual headwall retreat of up to 9 m. The upper and the lower slump floor have a total area of 20.8 ha. The surface area of the upper northern headwall eroding into the sediment-meltwater channel measured 23 617 m² (Figure 5 and Figure 19).

- Several meters of snow accumulate each winter along the ice-rich permafrost headwall. The banks of snow, together with accumulating debris on top of the snow, protect the headwall from thawing (Figure 16 and Figure 17). Snowbanks reduce throughout the thawing season, however, there are large variations in the pace of snowmelt between summer seasons (Figure 12 und Figure 13).

- Strong diurnal and day-to-day fluctuations in sediment-meltwater volume were found largely to be due to variations in incoming solar radiation and air temperature leading to ablation of the ice-rich permafrost headwall (Figure 23 and Figure 27). Furthermore, high

discharge volume led to high sediment concentration and therefore showed strong diurnal and day-to-day fluctuations in sediment-meltwater composition (Figure 31).

- In addition, rain was also observed to lead to an increase in discharge (Figure 29). However, only 10.4 % of the rain that fell into the catchment was detected at the discharge station (Table 3). The remaining 89.6 % may be lost to evaporation or percolation into the ground. No additional sediment load was recorded, which would have indicated an additional mass mobilization within the slump system (Figure 31).

- Snowmelt was the main driver for seasonal variations between July 2013, when thick banks of snow were present, and August 2012, which only had negligible snow patches. Sediment-meltwater discharge was higher in July 2013 due to the additional contribution of snowmelt. 25 000 m^3 of discharge was measured during just 18-days in July 2013, while in a similar 18-day period in August 2012 only 15 600 m^3 of discharge was observed (section 5.1.5). In July 2013, snowmelt led to a longer response time between peak incoming solar radiation and peak discharge volume due to the percolation of meltwater through the snow. This also resulted in continuous meltwater release throughout the night (basal flow, section 6.1.2 and Figure 42). In August, without snowbanks, the response time was faster, with peak discharge volume occurring just 22 to 28 minutes after peaks in incoming solar radiation (Figure 5 and Figure 23).

- In July 2013, snowmelt led to higher discharge volumes and therefore to dissolution of the eroding permafrost material. In July 2013, sediment-meltwater had only half the sediment concentration (82 g l^{-1}) of that measured in August 2012 (196 g l^{-1}) (Table **4**). In total, for both seasons of July 2013 and August 2012 (a total of 36 days), 40 600 m^3 of sediment-meltwater eroded into the near shore zone, including 506 kg dissolved organic carbon. The 5108 t of sediment also included 86 t total organic carbon and 9 t total nitrogen.

- The observations from 36-days during the field seasons at Slump D were upscaled to provide a minimal estimate of total sediment-meltwater release for the main thawing season (62 days from 1 July until 31 August) from all thaw slumps along the Yukon Coast. Slump D, with a total size of 20.8 ha, represented 5.11 % of the total area of active thaw slumps along the coast (all thaw slumps along the Yukon Coast cover an area of 159 ha). Over the thawing season from 1 July to 31 August, all thaw slumps along the Yukon Coast are estimated to release almost 1.4 Mio m^3 of sediment-meltwater containing more than 1.3 Mio. m^3 meltwater (including 17 t dissolved organic carbon) and 172 000 t of

sediment, including more than 3100 t total organic carbon and 327 t nitrogen (Table 6 and Table 12). This study shows that thaw slumps along the Yukon Coast contribute a large amount of sediment, organic carbon and nitrogen into the Arctic Ocean, especially compared to small rivers and catchments (section 6.2.5).

- Finally, this study provided several future projections of the possible evolution of thaw slumps along the Yukon Coast in a warming climate (section 0). The current major climatic driver for the release of sediment-meltwater is incoming solar radiation, which is projected to change only very little (<1 %) as cloud cover increases. This was found to lead to a negligible decrease in sediment-meltwater release (0.47 %). However, projected warming of the Arctic may lead to a prolongation of the thawing season and thus to an increase in sediment-meltwater release. Summer air temperature is projected to increase by between 2-3 °C by 2081-2100 and this may result in increases of between 109-114 % in sediment-meltwater volumes being released. Increases in precipitation in winter are not likely to result in more snow accumulation along the headwall, since the current snowdrift may have already reached the maximum headwall height. However, increasing summer rainfall may trigger additional mass mobilization of sediment and water.

In summary, sediment-meltwater release from retrogressive thaw slumps is mainly triggered by the incoming solar radiation and air temperature, but the nature of the released material is heavily depending on the snow cover. Retrogressive thaw slumps release considerable large amounts of meltwater and sediment containing organic carbon and nitrogen into the nearshore zone of the Yukon Coast. Under future projected Arctic warming headwall ablation may increase and release further sediment-meltwater with carbon that was previously stored in the frozen permafrost. This may impact the biogeochemical cycle in aquatic ecosystems and climate.

8. Appendix

8.1. Field Work

In August 2012 five retrogressive thaw slump headwalls were examined. At each slump headwall, one profile was described and sampled to compare the composition with the main field site of Slump D and its outflow channel. For specification, the top headwall surface was removed and fresh permafrost was described. The samples were quarried out with an axe, packed in a sample bag and kept frozen for examining ice content, grain size, total carbon and nitrogen, total organic carbon, and $\delta^{13}C$ in the Potsdam laboratory. Hydrological analyses were not possible due to the high sediment content and difficulties in extracting water.

8.1.1. Slump D´s northern headwall profile

A headwall profile of Slump D was taken on 15 August 2012 (Figure 50). The sampled profile was located on the northern side of the upper headwall in the organic-rich top layers (Figure 5). The aim was to have a data catalogue of all units from Slump D. Previously, samples of the ice-rich headwall were taken in 2008 (Fritz et al., 2012) as well as of the massive ground ice in 2012 (Tanski, 2013). This new profile was chosen since the organic-rich top layer contributed the most sediment to the discharge.

The exposed headwall profile was 280 cm high and consisted of one major sediment-rich ice unit. It showed eight sub-units, each of which was sampled. The lowest sub-unit I consisted of sediment-rich ice with an ice volume of approximately 75 %, including silt, sand, rounded pebbles up to 1 cm in size in a vertical ice structure. Sub-unit II at a depth of between 230-260 cm was an organic-rich layer with mossy peat and wood of 3 cm in size within sediment-rich ice with lenses up to 5 cm in size. The overlying sub-unit III (at depths of 200-230 cm) contained bright grey, silty sand with horizontal ice lenses up to 1 cm in size as well as pore ice. At a depth of 125-200 cm, sub-unit IV was restored by cryoturbation. This unit held a peat lens with 1.5 cm thick roots and had a maroon brown surface that turned black immediately after exposure. At these depths the ice lenses showed no specific orientation and silty-sand lenses reached a size of 10 cm. The sub-unit V had a bright green-grey matrix with sand lenses and organic rich intrusions and was found at depths from 120-125 cm. Ice lenses

with a vertical structure indicated the next 15 cm-thick sub-unit VI. Sub-unit VII was from 42-105 cm deep with a dark red brown silty sand matrix with wood pieces and horizontal ice lenses of 2 cm in size. The cryostructure was made of fine ice lenses and segregating ice (up to 3 cm in size) with vertical freezing horizons. The top of the headwall profile (sub-unit VIII) was the active layer. On the 15 August 2015 it was 42 cm deep, containing silty-sand with roots and sub-angular pebbles up to 2 cm in size within a beige matrix and 10 cm of peat on top.

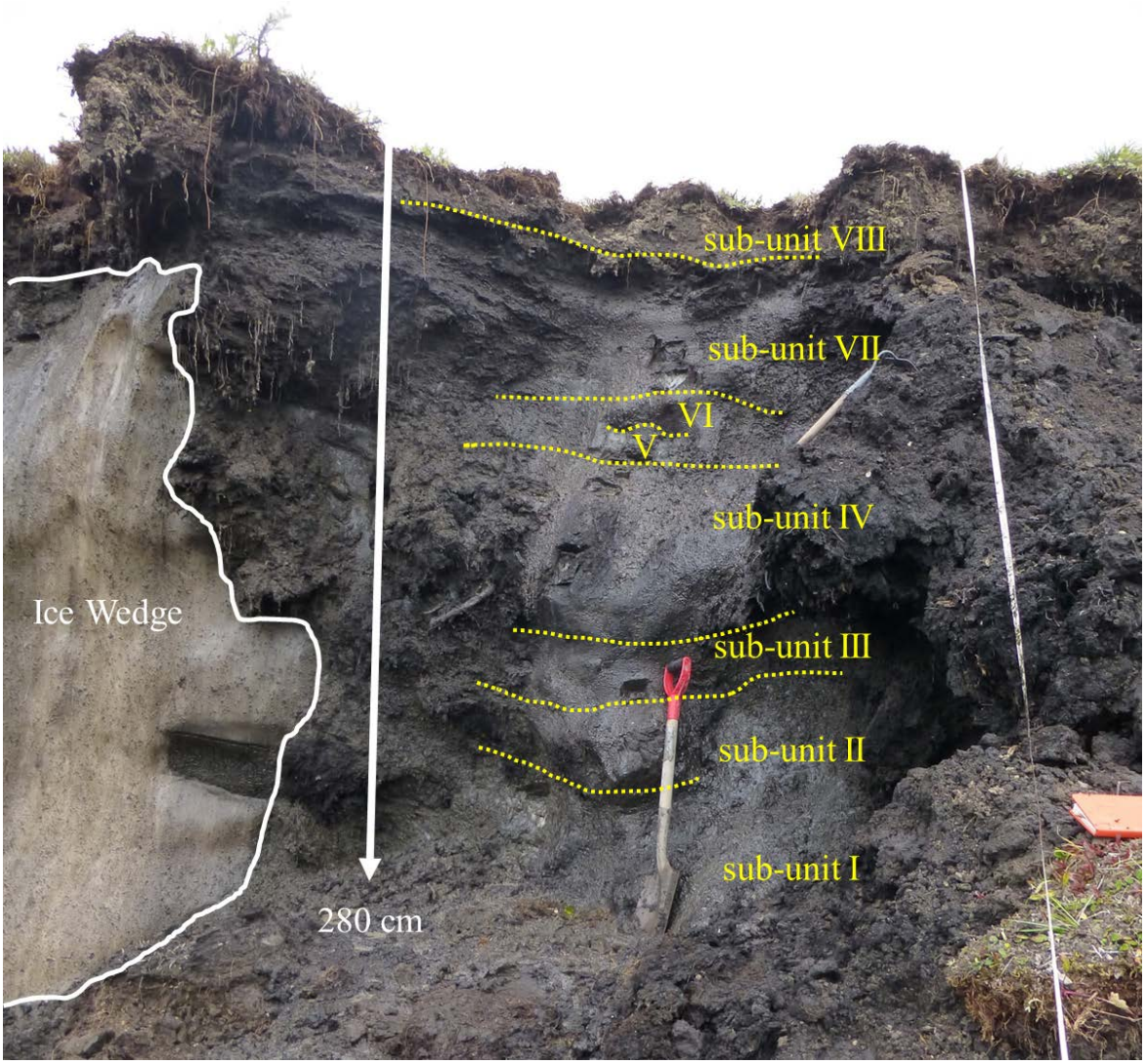

Figure 50. The 280 cm deep profile of Slump D on the north side of the upper northern headwall with eight ice-rich sediment sub-units.

8.1.2. Collinson Head slump

Collinson Head slump is situated on the northeastern tip of Herschel Island at 58 ± 3 m above sea level (N 69.57275, W 138.86986; Figure 4). In 2012, the active headwall (facing south) was more than 60 m wide and up to 1.9 m high. Terrain images were taken from the helicopter and the edge of the lower headwall (Figure 51 and Figure 52). On 4 August 2012 Collinson Head slump was examined (Figure 53). The headwall profile of the Collinson Head slump was subdivided into five units from the bottom of the mud pool to the top of the tundra vegetation (Figure 54). Unit I started from a depth of 130 cm and extended at least to a depth of 190 cm. The ice content was between 40-50 %, with ice veins, horizontal and sub-horizontal ice lentils of up to 1 cm in size, and massive pore ice. Its appearance was light grey with pebbles of up to 5 cm in size within sandy silt with clay. Unit II had the same grey occurrence, but with coarse lenticular-like ice of up to 1-2 cm in size, and formed the transition horizon of just 10 cm to Unit III. Unit III began at a depth of 120 cm and contained ice lenses up to 1 cm in size as well as a lenticular net in silty clay with pebbles. The ice content was more than 80 % and its color was grey-brown. At a depth of 60 cm, the active layer occurred and defined the next Unit IV (4 August 2012). This unit contained roots from the upper tundra surface in dark brown silty clay and peat lenses of up to 5 cm in size, with a distinct absence of ice lenses. The upper most Unit V was between 7-40 cm thick and made up of a red-brown, thick organic top layer with the tundra vegetation. Samples were taken at depths of 10 and 30 cm (Unit V), 40 cm (Unit IV), 50 and 80 cm (Unit III), 120 cm (Unit II), and 130 cm (Unit I).

Figure 51. Collinson Head slump on the northeast spit of Herschel Island. The active headwall facing south was about 60 m wide and up to 1.9 m high. The undisturbed tundra was about 58 m above sea level.

Figure 52. The headwall of the Collinson Head slump was about 2 m exposed with a sediment-rich top layer.

Figure 53. Collinson Head slump had an active headwall of more than 60 m in width and chunks of tundra eroded into the mud pool.

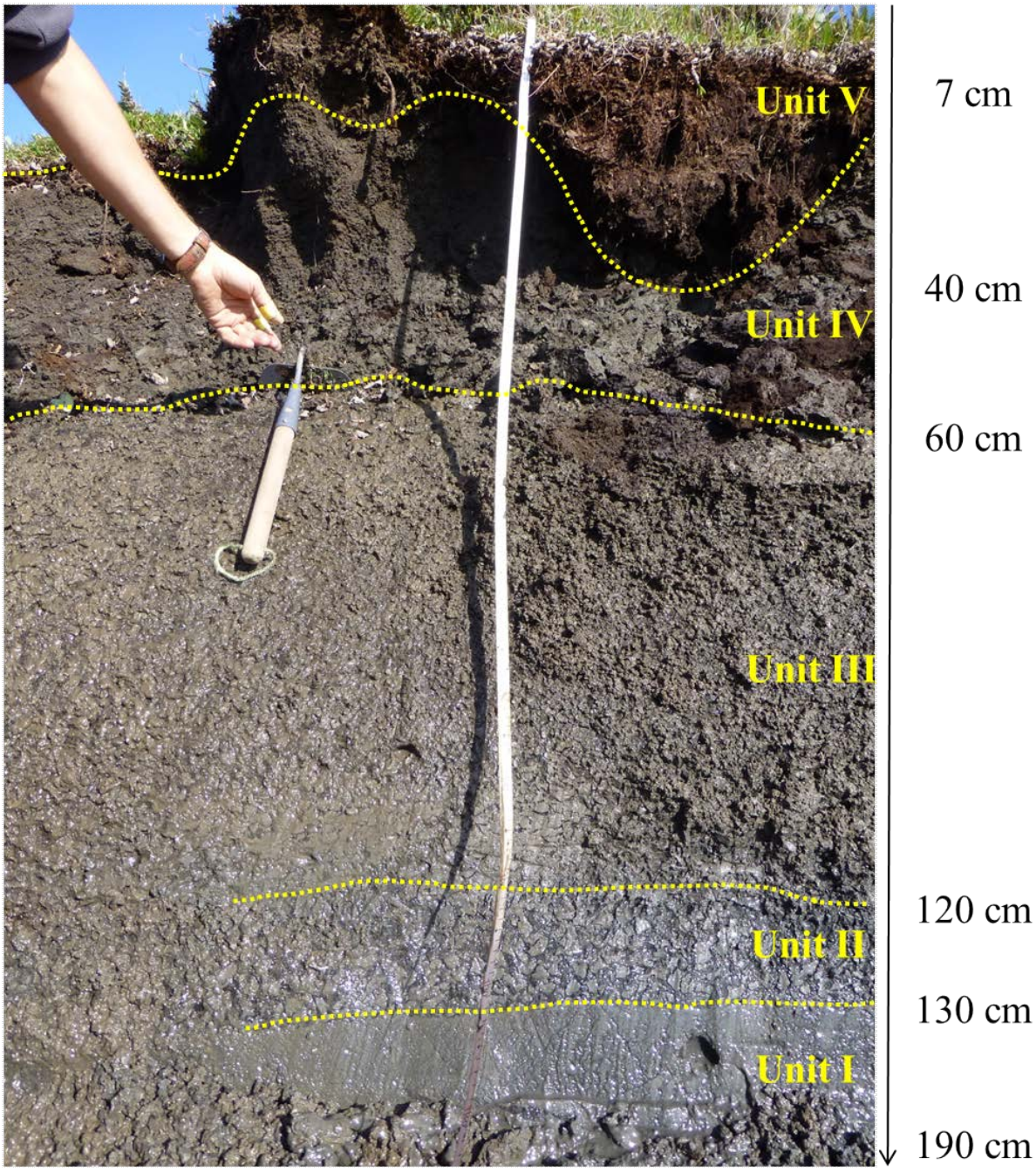

Figure 54. Profile of the Collinson Head slump which was about 190cm high and was divided into five units.

8.1.3. Herschel Island West Coast slump

The Herschel Island West Coast slump was over 200 m wide and the headwall faces northwest (N 69.606672, W 139.221540; Figure 4). The retrogressive thaw slump is subdivided into two levels with each headwall over 12 m high (Figure 55). The lower headwall consisted of laminated massive ground ice with air bubbles and clayey sediments. The upper headwall appeared to be made of ice-rich sediment.

On 11 August 2012 one profile was sampled along the lower and upper headwall of the Herschel Island West Coast slump (Figure 56 and Figure 57). The lower headwall showed laminated massive ground ice gently dipping westward. It included clear- to milky-white ice layers, distinct bands of ice and clay, intra-sedimental ice and air bubbles up to 5 mm in diameter (samples 1-6). More than 50 % of the upper headwall was covered with debris. Exposed headwall areas up to 10 m showed a chaotic lamination of grey ice-rich sediment (samples 7-12). The top of the headwall, at 47 m above sea level, was defined by a 40 cm thick, unfrozen, brown peat layer with roots (Figure 57).

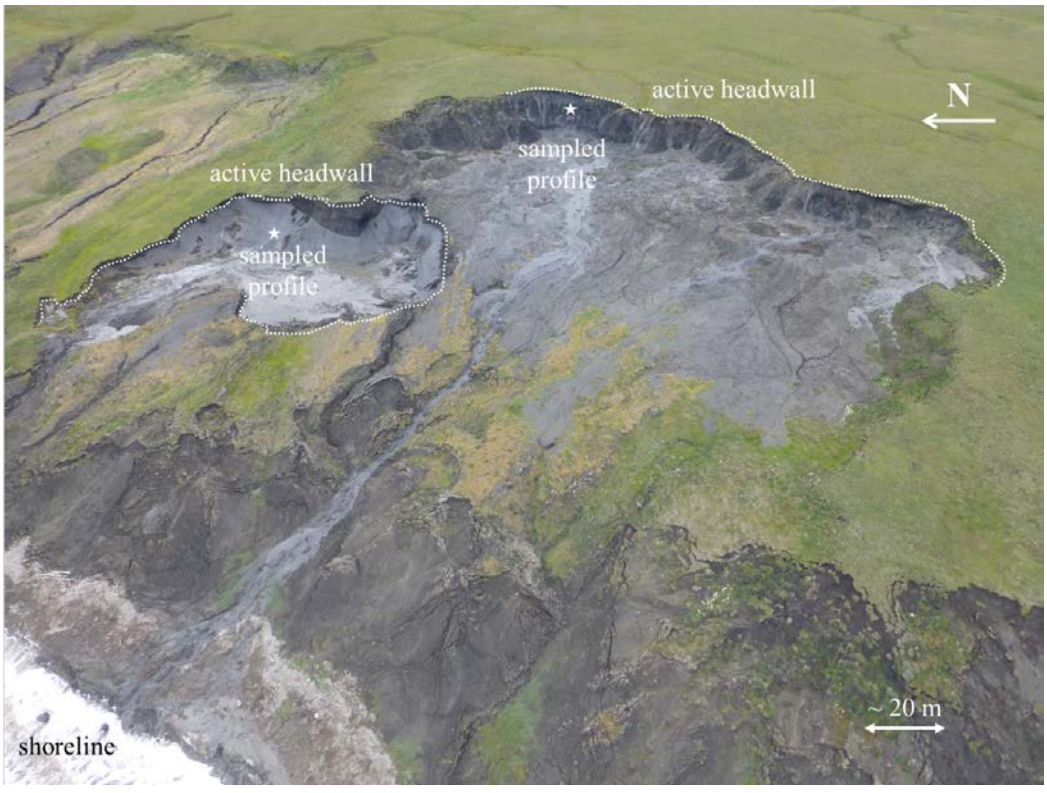

Figure 55. Herschel Island West Coast slump with two active headwalls. The lower headwall made of massive ice and the upper headwall made of less ice-rich sediment.

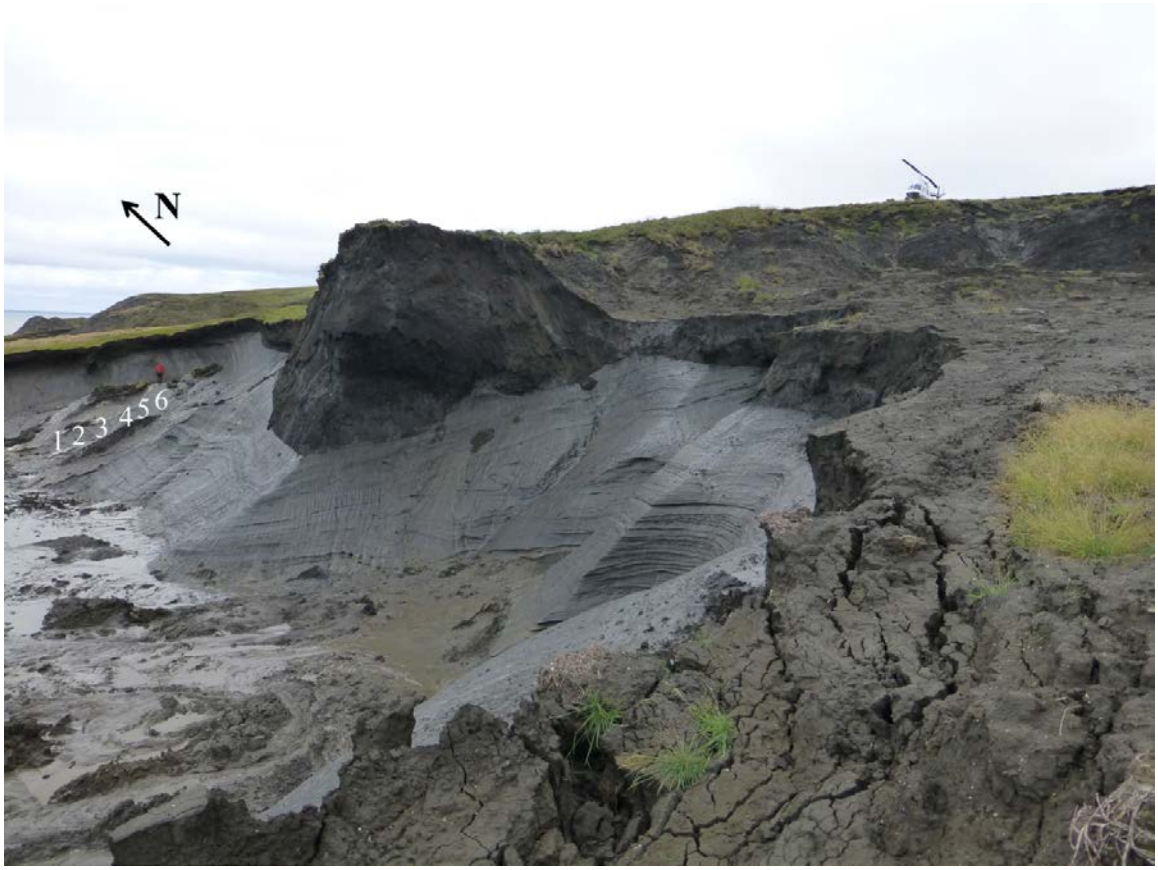

Figure 56. The lower headwall with westward-dipping laminated massive ice (samples 1-6) and on top chaotic ice-rich sediment.

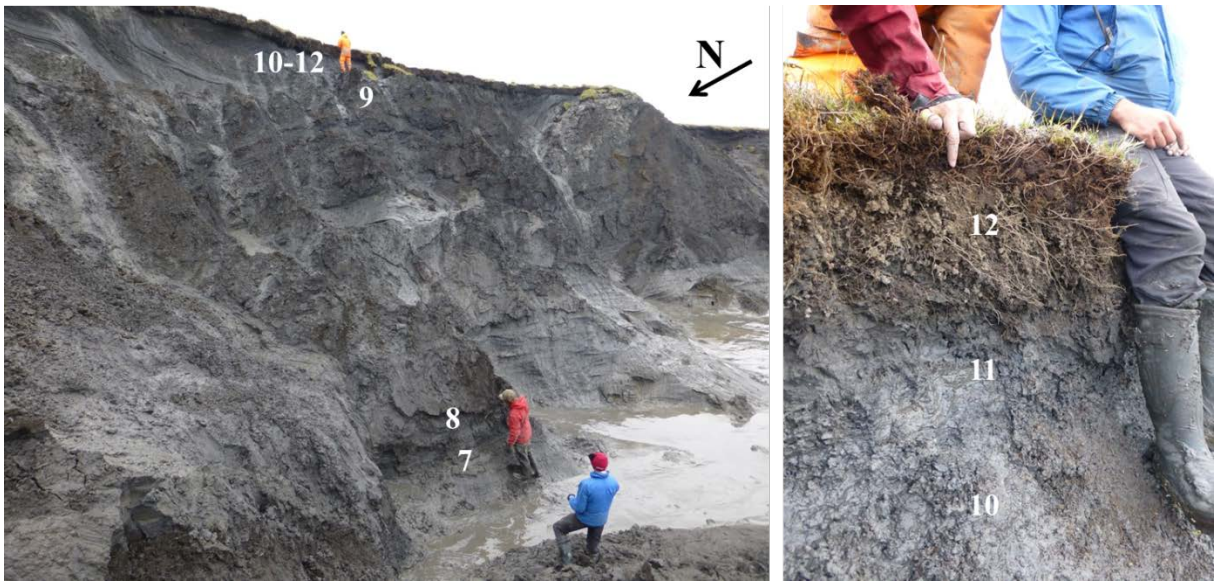

Figure 57. The upper headwall of the Herschel Island West Coast slump was about 17 m high with ice-rich sediment (samples 7-12).

8.1.4. Roland Bay slump

Roland Bay slump is situated about 11 km southeast of Herschel Island, 500 m east of Whale Bay and 6 km west of Roland Bay (N 69.42677, W 138.99857; Figure 4). The active headwall facing northeast was 208 m long and up to 4.5 m high. Further to the east, contiguous to the slump, an old headwall scarp indicated a former larger extent (300 m more) of the retrogressive thaw slump (Figure 58). More than 20 % of the exposed headwall had ice wedges in it. The eroded slump floor within the retrogressive thaw slump (Figure 59) was divided into 1) the active mud pool with big chunks of grass from the former tundra floating in liquefied debris, 2) big patches of white Mastodon flowers (Senecio congestus), 3) stabilized and dried mud surface with growing vegetation, and 4) outflow and mud fan showing the recent drainage into the ocean.

Headwall samples were taken between two ice wedges where the four stratigraphic units were the least deformed (Figure 60). The top of the headwall profile and therefore of the retrogressive thaw slump was 27 m ± 3 m above sea level. From the bottom to the top of the exposed 4.5 m high headwall: Unit I showed an exposed massive ice extend at least 1.5 m thick and consisted of 10 cm thick folded ice layers. The unit contained dark silt with milky segregated ice lenses up to 2 cm in size and deformed clear-ice lenses up to 1 m in size (samples 1 and 2). Unit II was 1 m thick and showed several laminated layers up to 20 cm in thickness. This unit was darker and more resistant. It was composed of more obvious thin black laminated silt layers in massive ground ice (samples 3 and 4). Unit III was a 1.5 m thick brown bank of clay-sand rich in massive ice with ice lenses (samples 5 and 6). Unit IV was about 50 cm thick and included light grey clay with dark grey peat on top (samples 7 and 8). On 10 August 2012, the active layer was 50 cm deep.

Figure 58. Roland Bay slump with a former headwall scarp and a 208 m long active headwall 11 km southeast of Herschel Island.

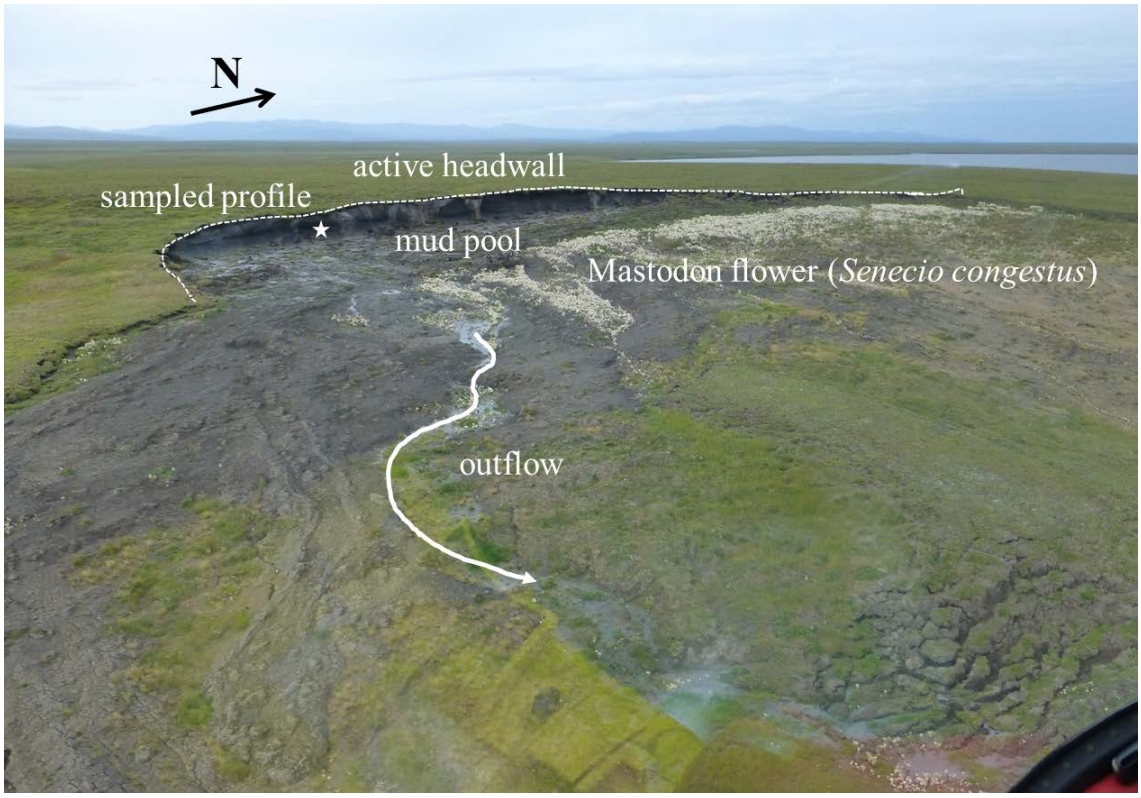

Figure 59. The 208 m long active headwall of Roland Bay slump with its ice wedges as well as the mud pool and below it Mastodon flowers (Senecio congestus).

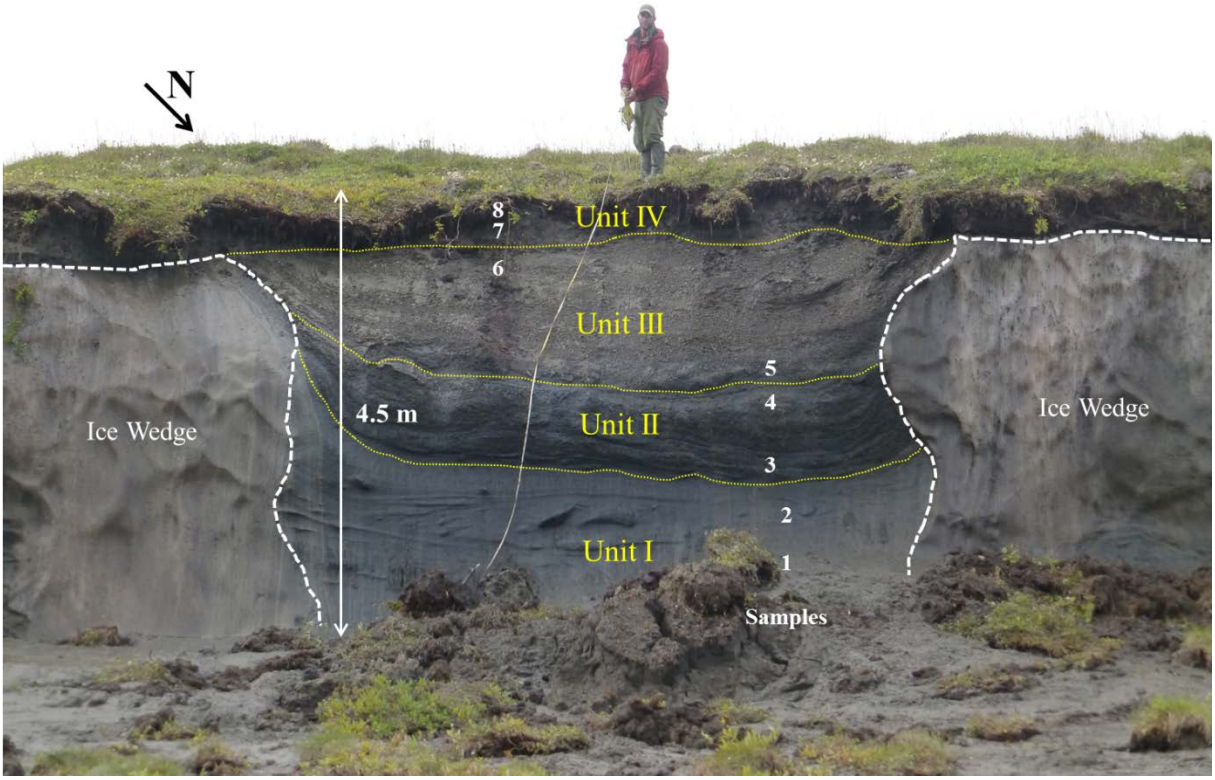

Figure 60. Profile of the Roland Bay slump between two ice wedges. The headwall was 4.5 m high and was subdivided into four units, each of them sampled twice.

8.1.5. Kay Point slump

Kay Point slump is situated 43 km southeast of Herschel Island. The highest point of the north facing headwall was 58 m ± 2 m above sea level (N 69.24677, W 138.31834; Figure 4). The main headwall was over 200 m wide and subdivided into the western part with structure-less ice-rich sediment with 7 m deep ice wedges and the eastern headwall made up of blue, sediment-rich and clear folded massive ground ice (Figure 61). Aerial oblique photography from the helicopter showed that the sharp transition correlated with a former headwall scarp northwards. The samples were taken along the eastern headwall (140 m long) of the 12.4 m high headwall. The top of the headwall was composed of a 2.4 m thick layer of ice-rich sediment and above 10 m of massive ground ice.

The headwall profile of 10.85 m was divided into three units from the bottom to the top (Figure 62). Unit I was folded massive ground ice with blue ice, white milky ice, and sediment layers. This unit was about 10 m thick and had a sharp edge to the upper units. Unit II was 85 cm thick and made up of ice-rich sediment. This lower 30 cm of this unit had a lenticular cryostructure with ice lenses up to 5 mm in size. The matrix was bright grey (clay) to brown (sandy). In the middle section, at a depth of 30 cm, there were vertical to sub-vertical ice lenses up to 2 mm in thickness. The top 25 cm had a lenticular cryostructure with 1 mm big ice lenses, rounded pebbles (2-3 cm in size) and beige organic-rich lenses of decomposed plant material. The top Unit III was 1.55 m thick and had roots until a depth of 1.1 m. Unit III had elongated ice lenses up to 10 mm in thickness, clay-silty sand with pebbles up to 12 cm in size, and peat lenses up to 40 cm in size. The active layer was 55 cm deep (12 August 2012).

Figure 61. Kay Point slump with its white-blue bands of massive ground ice to the east (left) and structure-less ice-rich sediment headwall to the west (right).

Figure 62. Folded massive bands of blue ice, white milky ice and sediment layers (Unit I) with ice-rich sediment layer on top (Units II and III) and an ice wedge cutting through the units.

8.2. Laboratory Work

Sedimentological analyses (as described in section 4.2.1) of the 43 headwall samples were conducted to determine sediment content, grain size distribution, total carbon, total organic carbon, total nitrogen, and $\delta^{13}C$ (Figure 63). Ten samples were analyzed from Slump D, seven from Collinson Head slump, twelve from Herschel Island West Coast slump, eight from Roland Bay slump and six from Kay Point. No hydrochemical analyses of the headwall samples were made due to the difficulty in extracting water from the sediment-rich samples.

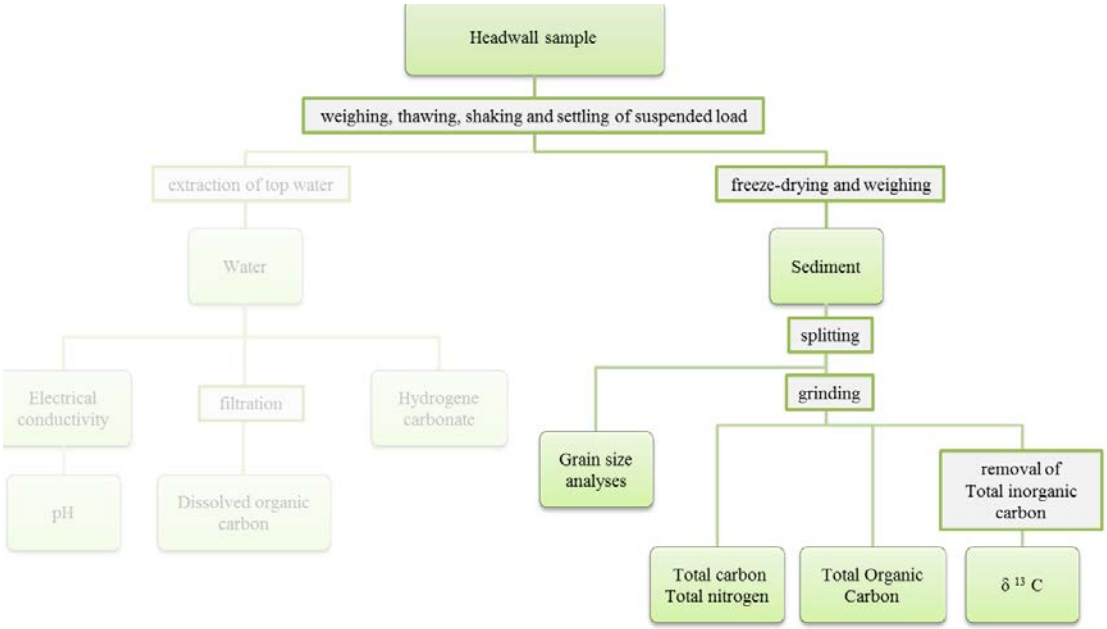

Figure 63. All 43 ice-rich permafrost samples from the five retrogressive thaw slump headwalls were sedimentologically analysed. Hydrochemical analyses were not possible due to the difficulties associated with extracting the pore water.

8.2.1. Volumetric Ice Content

The volumetric ice content varied between 33-100 % (Figure 45). The lowest ice volumes were measured in the active layers and top layers of the retrogressive thaw slumps but then increased with depth. The headwall samples from Slump D had a volumetric ice content between 62-93 %, Collinson Head slump between 39-75 %, Herschel Island West Coast slump between 33-100 %, Roland Bay slump between 33-76 %, and Kay Point slump between 41-100 %. All of the headwall samples from retrogressive thaw slumps along the Yukon Coast were therefore in the range of the ice content of Slump D (Table 5). The water

volume of Slump D´s outflow was 97 % in July 2013 and 93 % in August 2012 and was higher than the ice content sampled from the Slump D profiles (62-93 vol %). This illustrates the large contribution from massive ground ice in the permafrost headwall.

8.2.2. Grain Size

Grain size distributions from all five retrogressive thaw slumps were clayey to sandy silt. Samples from Roland Bay (blue) and Collinson Head (black) had two peaks in fine silt and sand (Figure 64, left). Herschel Island West Coast samples (green) showed two peaks in coarse clay/fine silt and coarse silt/fine sand (Figure 64, right). The sample from Slump D (red) showed a wide peak in the range of fine to mid-sized silt while the Kay Point sample (yellow) showed two peaks in fine silt and fine sand. The range of grain size distribution of all five retrogressive thaw slumps mirrored the range of grain size of Slump D´s outflow samples, with two major peaks in fine silt and fine sand (Figure 32). The sediment triangle diagram following Shepard (1954) shows that the samples from the five retrogressive thaw slumps are in the same range as for the Slump D outflow samples, in the range of clayey/sandy silt (Figure 32 and Figure 47).

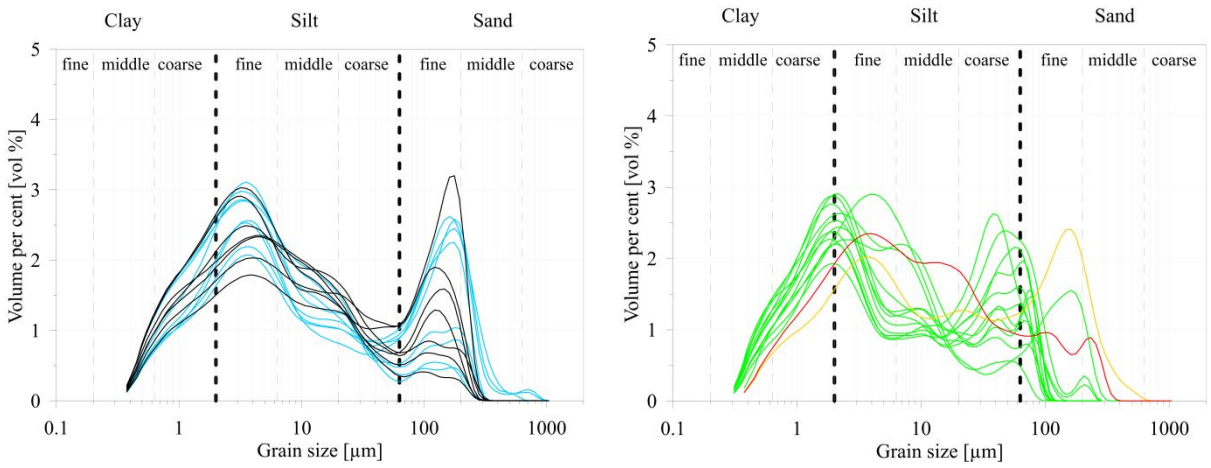

Figure 64. Left: Grain size distributions from Roland Bay (blue) and Collinson Head (black) showed two peaks in fine silt and fine sand, defined as clayey to sandy silt. Right: Grain size distribution from Herschel Island West Coast slump (green) showed two dominant peaks in coarse clay/fine silt and coarse silt defined mostly as clayey to sandy silt. Grain sizes from Kay Point (yellow) had two peaks in fine silt and sand, while the sample from the Slump D headwall (red) was poorly sorted with a wide range of fine silt to fine sand.

8.3. Evolution of Slump D

8.3.1. Geo Eye satellite of Slump D

Geo Eye satellite image 2001

Geo Eye satellite image 2011

8.3.2. Aerial Oblique Photography of Slump D

Aerial oblique photo 2006

Aerial oblique photo 7 August 2008

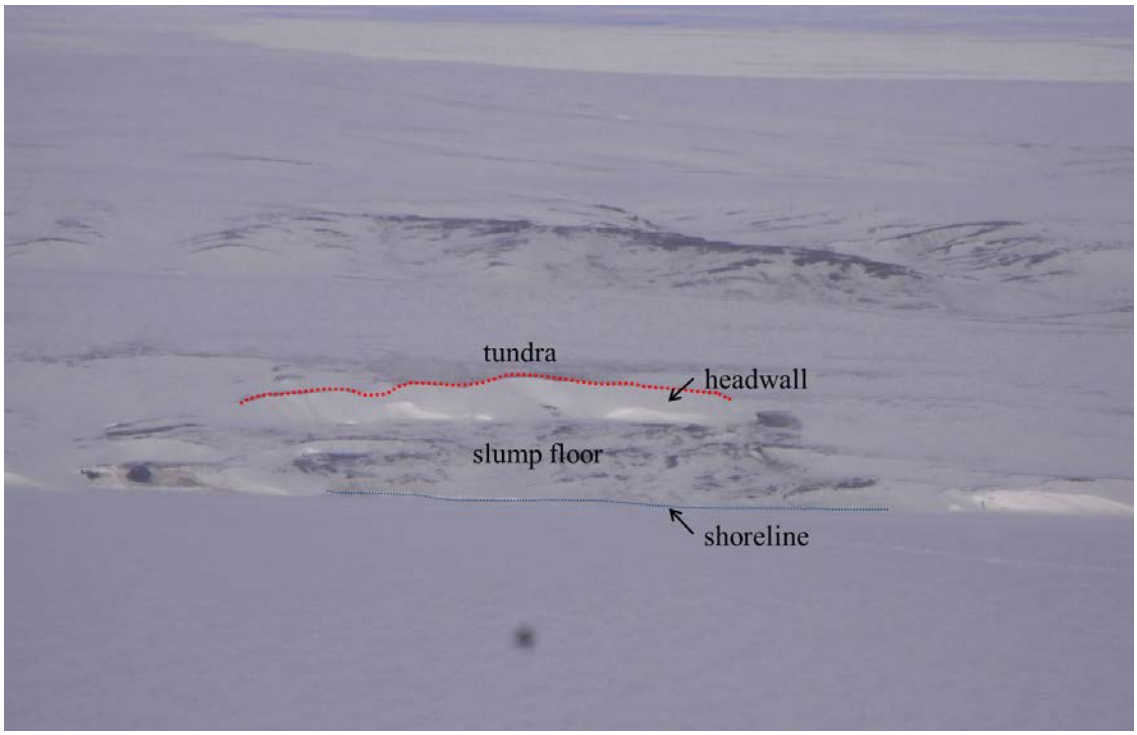

Aerial oblique photo 26 April 2009

Aerial oblique photo 28 July 2010

Aerial oblique photo 11August 2014

Aerial oblique photo 19 July 2016

8.3.3. LiDAR of Slump D

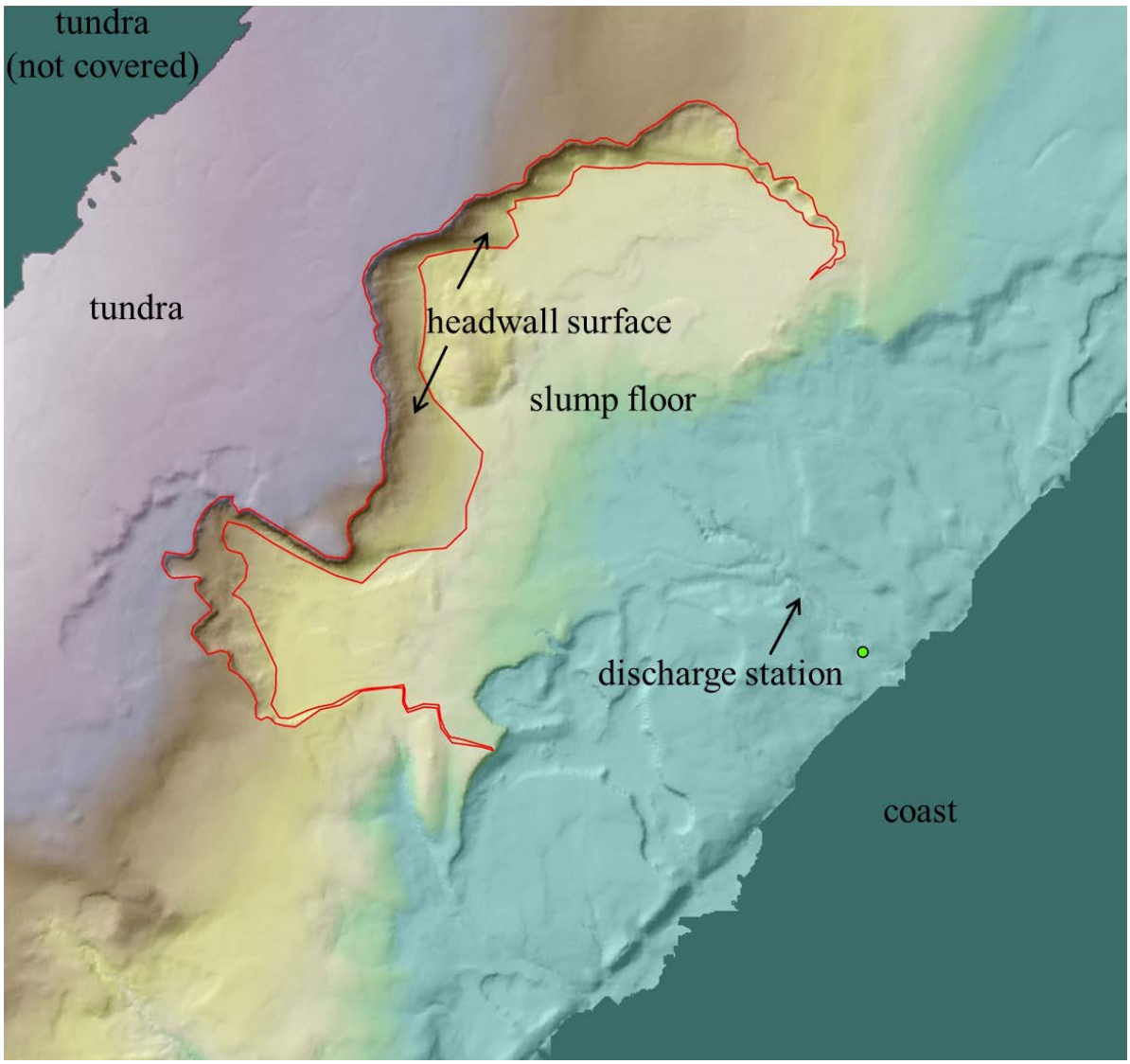

LiDAR 22 July 2013: Headwall surface between undisturbed tundra and slump floor

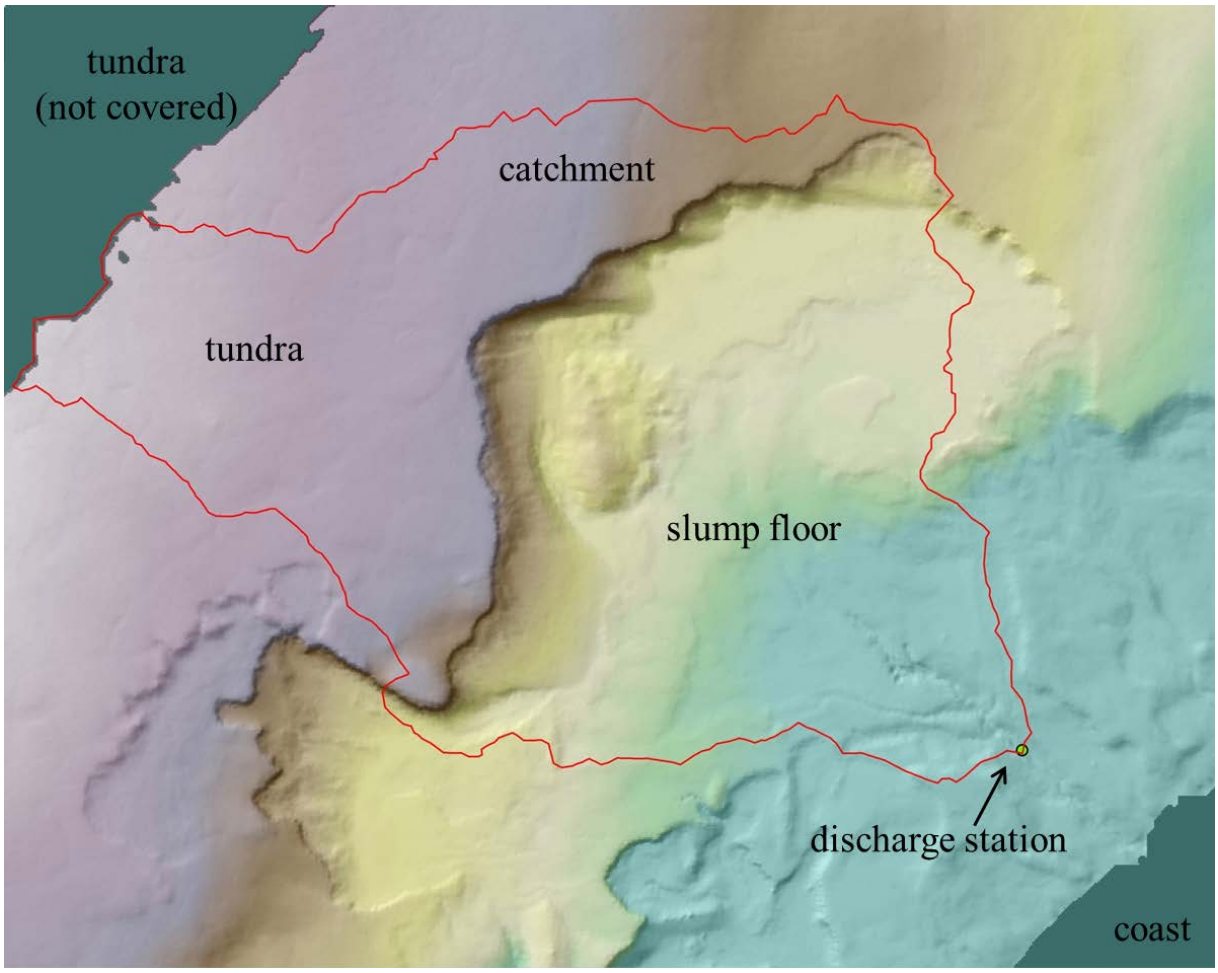

LiDAR 22 July 2013: Catchment including undisturbed tundra, headwall and slump floor

8.3.4. Time Lapse Photography of Slump D´s Headwall

The following photos are time lapse photos taken in July 2013 of the snowmelt in the middle section of the upper headwall. The photo section is about 15 m wide and 10 m high.

9 July 2013 1:30 am

11 July 2013 06:00 pm

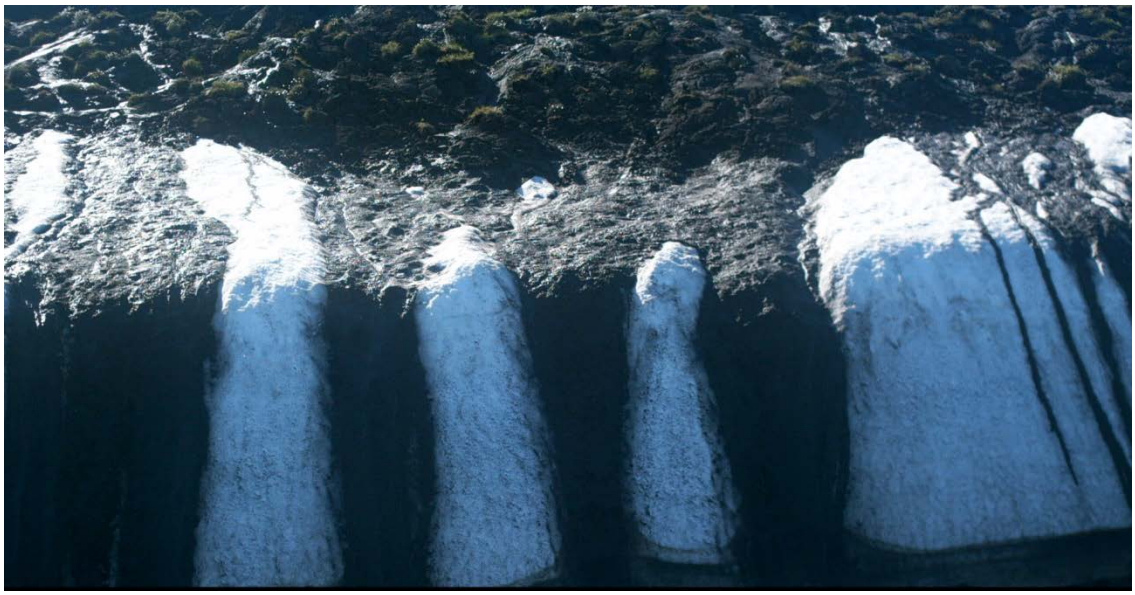

13 July 2013 06:00 pm

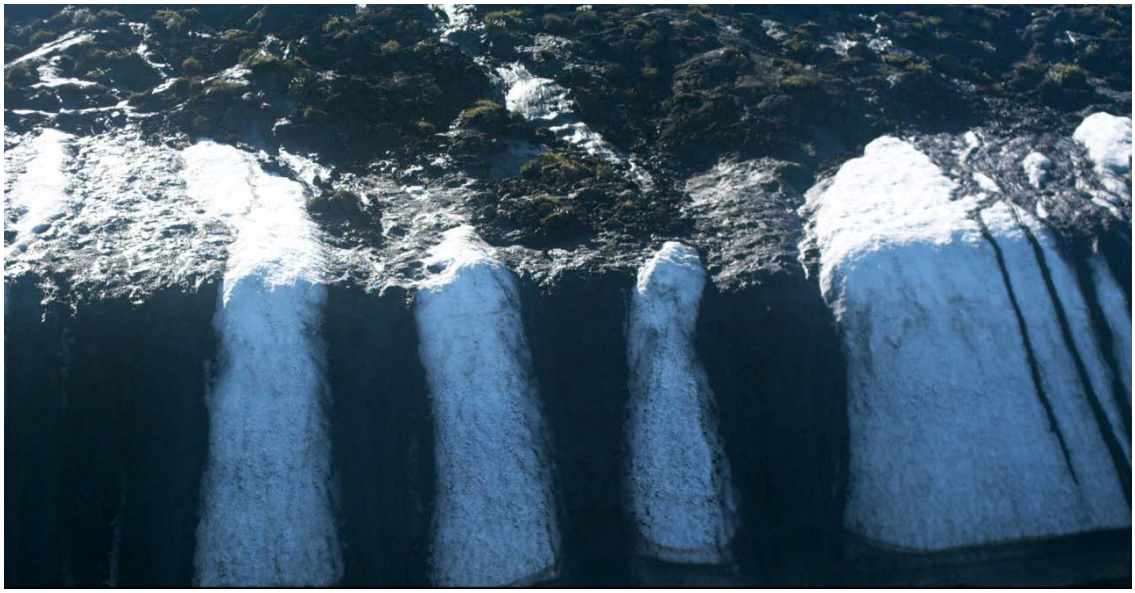

13 July 2013 6:30 pm

15 July 2013 12:30 am

17 July 2013 12:00 pm

23 July 2013 01:00pm

9. References

Ashastina, K., Schirrmeister, L., Fuchs, M., Kienast, F., 2016. Pleistocene climate characteristics in the most continental part of the northern hemisphere: insights from cryolithological features of the Batagay mega thaw slump in the Siberian Yana Highlands. Climate of the Past Discussion.

Balser, A.W., Jones, J.B., Gens, R., 2014. Timing of retrogressive thaw slump initiation in the Noatak Basin, northwest Alaska, USA. Journal of Geophysical Research: Earth Surface 119, 1106-1120.

Battin, T.J., Kaplan, L.A., Findlay, S., Hopkinson, C.S., Marti, E., Packman, A.I., Newbold, J.D., Sabater, F., 2008. Biophysical controls on organic carbon fluxes in fluvial networks. Nature Geoscience 1, 95-100.

Blott, S.J., Pye, K., 2001. GRADISTAT: a grain size distribution and statistics package for the analysis of unconsolidated sediments. Earth surface processes and Landforms 26, 1237-1248.

Boike, J., Langer, M., Lantuit, H., Muster, S., Roth, K., Sachs, T., Overduin, P., Westermann, S., McGuire, A.D., 2012. Permafrost–physical aspects, carbon cycling, databases and uncertainties, Recarbonization of the Biosphere. Springer, pp. 159-185.

Bouchard, M., 1974. Surficial Geology of Herschel Island, Yukon Territory. M. Sc. thesis University of Montréal (70 pp.).

Brown, J., Ferrians Jr, O., Heginbottom, J., Melnikov, E., 1997. Circum-Arctic map of permafrost and ground-ice conditions.

Burn, C., Lewkowicz, A., 1990. CANADIAN LANDFORM EXAMPLES-17 RETROGRESSIVE THAW SLUMPS. The Canadian Geographer/Le Géographe canadien 34, 273-276.

Burn, C., Zhang, Y., 2009. Permafrost and climate change at Herschel Island (Qikiqtaruq), Yukon Territory, Canada. Journal of Geophysical Research: Earth Surface 114.

Carson, M., Jasper, J., Conly, F.M., 1998. Magnitude and sources of sediment input to the Mackenzie Delta, Northwest Territories, 1974–94. Arctic, 116-124.

Chen, Y., Miller, J.R., Francis, J.A., Russell, G.L., 2011. Projected regime shift in Arctic cloud and water vapor feedbacks. Environmental Research Letters 6, 044007.

Church, J.A., Clark, P.U., Cazenave, A., Gregory, J.M., Jevrejeva, S., Levermann, A., Merrifield, M.A., Milne, G.A., Nerem, R.S., Nunn, P.D., 2013. Sea level change, Climate Change 2013: The Physical Science Basis. Contribution of Working Group I to the Fifth Assessment Report of the Intergovernmental Panel on Climate Change ed. PM Cambridge University Press.

Collins, M., Knutti, R., Arblaster, J., Dufresne, J., Fichefet, T., Friedlingstein, P., Gao, X., Gutowski, W., Johns, T., Krinner, G., 2013. Climate change 2013: the physical science basis.

Contribution of Working Group I to the Fifth Assessment Report of the Intergovernmental Panel on Climate Change. Long-term Clim. Chang. Proj. Commitments Irreversibility, Cambridge Univ. Press. Cambridge, UK, New York.

Couture, N.J., 2010. Fluxes of soil organic carbon from eroding permafrost coasts, Canadian Beaufort Sea.

Covington, A., Bates, R., Durst, R., 1985. Definition of pH scales, standard reference values, measurement of pH and related terminology (Recommendations 1984). Pure and Applied Chemistry 57, 531-542.

Cray, H.A., Pollard, W.H., 2015. Vegetation recovery patterns following permafrost disturbance in a Low Arctic setting: case study of Herschel Island, Yukon, Canada. Arctic, Antarctic, and Alpine Research 47, 99-113.

Czudek, T., Demek, J., 1970. Thermokarst in Siberia and its influence on the development of lowland relief. Quaternary Research 1, 103-120.

Favaro, E.A., Lamoureux, S.F., 2014. Antecedent controls on rainfall runoff response and sediment transport in a high arctic catchment. Geografiska Annaler: Series A, Physical Geography 96, 433-446.

French, H., 1974. Active thermokarst processes, eastern Banks Island, western Canadian arctic. Canadian Journal of Earth Sciences 11, 785-794.

French, H.M., 2007. The Periglacial Environment. Wiley.

Fritz, M., Opel, T., Tanski, G., Herzschuh, U., Meyer, H., Eulenburg, A., Lantuit, H., 2015. Dissolved organic carbon (DOC) in Arctic ground ice. The Cryosphere Discussions 9, 77-114.

Fritz, M., Wetterich, S., Meyer, H., Schirrmeister, L., Lantuit, H., Pollard, W.H., 2011. Origin and characteristics of massive ground ice on Herschel Island (western Canadian Arctic) as revealed by stable water isotope and hydrochemical signatures. Permafrost and Periglacial Processes 22, 26-38.

Fritz, M., Wetterich, S., Schirrmeister, L., Meyer, H., Lantuit, H., Preusser, F., Pollard, W.H., 2012. Eastern Beringia and beyond: late Wisconsinan and Holocene landscape dynamics along the Yukon Coastal Plain, Canada. Palaeogeography, Palaeoclimatology, Palaeoecology 319, 28-45.

Grom, J., Pollard, W., 2008. A study of high Arctic retrogressive thaw slump dynamics, Eureka Sound Lowlands, Ellesmere Island, Proceedings of the Ninth International Conference on Permafrost, pp. 545-550.

Günther, F., Overduin, P.P., Sandakov, A.V., Grosse, G., Grigoriev, M.N., 2013. Short-and long-term thermo-erosion of ice-rich permafrost coasts in the Laptev Sea region. Biogeosciences 10, 4297-4318.

Harris, S.A., 2002. Causes and consequences of rapid thermokarst development in permafrost or glacial terrain. Permafrost and periglacial processes 13, 237-242.

Hill, P.R., Blasco, S.M., Harper, J.R., Fissel, D.B., 1991. Sedimentation on the Canadian Beaufort Shelf. Continental Shelf Research 11, 821-842.

Hugelius, G., Strauss, J., Zubrzycki, S., Harden, J.W., Schuur, E., Ping, C.-L., Schirrmeister, L., Grosse, G., Michaelson, G.J., Koven, C.D., 2014. Estimated stocks of circumpolar permafrost carbon with quantified uncertainty ranges and identified data gaps. Biogeosciences 11, 6573-6593.

Huscroft, C.A., Lipovsky, P.S., Bond, J.D., 2004. Permafrost and landslide activity: Case studies from southwestern Yukon Territory, in: Emond, D.S., Lewis, L.L. (Eds.), Yukon Exploration and Geology 2003. Yukon Geological Suvey, pp. 107-119.

Johannessen, O.M., Bengtsson, L., Miles, M.W., Kuzmina, S.I., Semenov, V.A., Alekseev, G.V., Nagurnyi, A.P., Zakharov, V.F., Bobylev, L.P., Pettersson, L.H., 2004. Arctic climate change: Observed and modelled temperature and sea-ice variability. Tellus A 56, 328-341.

Jorgenson, M.T., Shur, Y.L., Pullman, E.R., 2006. Abrupt increase in permafrost degradation in Arctic Alaska. Geophysical Research Letters 33.

Kerfoot, D.E., 1969. The geomorphology and permafrost conditions of Garry Island, NWT. University of British Columbia.

Keuper, F., Bodegom, P.M., Dorrepaal, E., Weedon, J.T., Hal, J., Logtestijn, R.S., Aerts, R., 2012. A frozen feast: thawing permafrost increases plant-available nitrogen in subarctic peatlands. Global Change Biology 18, 1998-2007.

Kohnert, K., Serafimovich, A., Hartmann, J., Sachs, T., 2014. Airborne measurements of methane fluxes in Alaskan and Canadian tundra with the research aircraft Polar 5. Berichte zur Polar-und Meeresforschung= Reports on polar and marine research 673.

Kokelj, S., Lacelle, D., Lantz, T., Tunnicliffe, J., Malone, L., Clark, I., Chin, K., 2013. Thawing of massive ground ice in mega slumps drives increases in stream sediment and solute flux across a range of watershed scales. Journal of Geophysical Research: Earth Surface 118, 681-692.

Kokelj, S., Lantz, T., Kanigan, J., Smith, S., Coutts, R., 2009. Origin and polycyclic behaviour of tundra thaw slumps, Mackenzie Delta region, Northwest Territories, Canada. Permafrost and Periglacial Processes 20, 173-184.

Kokelj, S., Tunnicliffe, J., Lacelle, D., Lantz, T., Chin, K., Fraser, R., 2015. Increased precipitation drives mega slump development and destabilization of ice-rich permafrost terrain, northwestern Canada. Global and Planetary Change 129, 56-68.

Lacelle, D., Bjornson, J., Lauriol, B., 2010. Climatic and geomorphic factors affecting contemporary (1950–2004) activity of retrogressive thaw slumps on the Aklavik Plateau, Richardson Mountains, NWT, Canada. Permafrost and Periglacial Processes 21, 1-15.

Lacelle, D., Brooker, A., Fraser, R.H., Kokelj, S.V., 2015. Distribution and growth of thaw slumps in the Richardson Mountains–Peel Plateau region, northwestern Canada. Geomorphology 235, 40-51.

Lamoureux, S.F., Lafrenière, M.J., 2009. Fluvial impact of extensive active layer detachments, Cape Bounty, Melville Island, Canada. Arctic, Antarctic, and Alpine Research 41, 59-68.

Lamoureux, S.F., Lafrenière, M.J., 2014. Seasonal fluxes and age of particulate organic carbon exported from Arctic catchments impacted by localized permafrost slope disturbances. Environmental Research Letters 9, 045002.

Lantuit, H., Overduin, P.P., Couture, N., Wetterich, S., Aré, F., Atkinson, D., Brown, J., Cherkashov, G., Drozdov, D., Forbes, D.L., 2012a. The Arctic coastal dynamics database: a new classification scheme and statistics on Arctic permafrost coastlines. Estuaries and Coasts 35, 383-400.

Lantuit, H., Pollard, W., 2005. Temporal stereophotogrammetric analysis of retrogressive thaw slumps on Herschel Island, Yukon Territory. Natural Hazards and Earth System Science 5, 413-423.

Lantuit, H., Pollard, W., 2008. Fifty years of coastal erosion and retrogressive thaw slump activity on Herschel Island, southern Beaufort Sea, Yukon Territory, Canada. Geomorphology 95, 84-102.

Lantuit, H., Pollard, W., Couture, N., Fritz, M., Schirrmeister, L., Meyer, H., Hubberten, H.W., 2012b. Modern and late Holocene retrogressive thaw slump activity on the Yukon coastal plain and Herschel Island, Yukon Territory, Canada. Permafrost and Periglacial Processes 23, 39-51.

Lantuit, H., Rachold, V., Pollard, W., Steenhuisen, F., Ødegård, R., Hubberten, H.-W., 2009. Towards a calculation of organic carbon release from erosion of Arctic coasts using non-fractal coastline datasets. Marine Geology 257, 1-10.

Lantz, T.C., Kokelj, S.V., 2008. Increasing rates of retrogressive thaw slump activity in the Mackenzie Delta region, NWT, Canada. Geophysical Research Letters 35.

Leibman, M., Gubarkov, A., Khomutov, A., Kizyakov, A., Vanshtein, B., 2008. Coastal processes at the tabular-ground-ice-bearing area, Yugorsky Peninsula, Russia, Proceedings of the 9th International Conference on Permafrost, Fairbanks, Alaska, pp. 1037-1042.

Leibman, M.O., 1995. Cryogenic landslides on the Yamal Peninsula, Russia: preliminary observations. Permafrost and Periglacial Processes 6, 259-264.

Lewkowicz, A.G., 1985. Use of an ablatometer to measure short-term ablation of exposed ground ice. Canadian Journal of Earth Sciences 22, 1767-1773.

Lewkowicz, A.G., 1986. Rate of Short-Term ablation of Exposed Ground Ice Banks Island Northwest Territories Canada. Journal of Glaciology 32, 511-519.

Lewkowicz, A.G., 1987. Headwall retreat of ground-ice slumps, Banks Island, Northwest Territories. Canadian Journal of Earth Sciences 24, 1077-1085.

Lewkowicz, A.G., Young, K.L., 1990. Hydrology of a perennial snowbank in the continuous permafrost zone, Melville Island, Canada. Geografiska Annaler. Series A. Physical Geography, 13-21.

Macdonald, R., Solomon, S., Cranston, R., Welch, H., Yunker, M., Gobeil, C., 1998. A sediment and organic carbon budget for the Canadian Beaufort Shelf. Marine Geology 144, 255-273.

Mackay, J.R., 1959. Glacier ice-thrust features of the Yukon coast. Geographical Bulletin 13, 5-21.

Mackay, J.R., 1966. Segregated epigenetic ice and slumps in permafrost, Mackenzie delta area, NWT. Geogr. Bull 8, 59-80.

Malenfant-Lepage, J., Doré, G., Burn, C.R., 2014. Field Guide-Alaska Highway: Advanced Seminar on Permafrost Engineering Applied to Transportation Infrastructure. Yukon College, Whitehorse, Yukon.

Marsh, P., Woo, M.K., 1984. Wetting front advance and freezing of meltwater within a snow cover: 1. Observations in the Canadian Arctic. Water Resources Research 20, 1853-1864.

McGuire, A.D., Anderson, L.G., Christensen, T.R., Dallimore, S., Guo, L., Hayes, D.J., Heimann, M., Lorenson, T.D., Macdonald, R.W., Roulet, N., 2009. Sensitivity of the carbon cycle in the Arctic to climate change. Ecological Monographs 79, 523-555.

Meyers, P., Ishiwatari, R., 1995. Organic matter accumulation records in lake sediments, Physics and chemistry of lakes. Springer, pp. 279-328.

Meyers, P.A., 1994. Preservation of elemental and isotopic source identification of sedimentary organic matter. Chemical Geology 114, 289-302.

Meyers, P.A., 2003. Applications of organic geochemistry to paleolimnological reconstructions: a summary of examples from the Laurentian Great Lakes. Organic geochemistry 34, 261-289.

Myers-Smith, I.H., Forbes, B.C., Wilmking, M., Hallinger, M., Lantz, T., Blok, D., Tape, K.D., Macias-Fauria, M., Sass-Klaassen, U., Esther, L., 2011a. Shrub expansion in tundra ecosystems: dynamics, impacts and research priorities. Environmental Research Letters 6, 045509.

Myers-Smith, I.H., Hik, D.S., Kennedy, C., Cooley, D., Johnstone, J.F., Kenney, A.J., Krebs, C.J., 2011b. Expansion of canopy-forming willows over the twentieth century on Herschel Island, Yukon Territory, Canada. Ambio 40, 610-623.

Nelson, F.E., Anisimov, O.A., Shiklomanov, N.I., 2001. Subsidence risk from thawing permafrost. Nature 410, 889-890.

Obu, J., Lantuit, H., Fritz, M., Pollard, W.H., Sachs, T., Günther, F., 2016a. Relation between planimetric and volumetric measurements of permafrost coast erosion: a case study from Herschel Island, western Canadian Arctic. Polar Research 35.

Obu, J., Lantuit, H., Grosse, G., Günther, F., Sachs, T., Helm, V., Fritz, M., 2016b. Coastal erosion and mass wasting along the Canadian Beaufort Sea based on annual airborne LiDAR elevation data. Geomorphology.

Oliva, M., Ruiz-Fernández, J., 2015. Coupling patterns between para-glacial and permafrost degradation responses in Antarctica. Earth Surface Processes and Landforms 40, 1227-1238.

Pohl, S., Marsh, P., 2006. Modelling the spatial–temporal variability of spring snowmelt in an arctic catchment. Hydrological Processes 20, 1773-1792.

Pollard, W., 1990. The nature and origin of ground ice in the Herschel Island area, Yukon Territory, Proceedings, Fifth Canadian Permafrost Conference, Québec, pp. 23-30.

Priestley, C.H.B., Taylor, R.J., 1972. On the assessment of surface heat flux and evaporation using large scale parameters, Mon. Weather Rev. Citeseer, Division of Atmospheric Physics,

Commonwealth Scientific and Industrial Research Organization,

Aspendale, Victoria, Australia.

Rachold, V., Eicken, H., Gordeev, V., Grigoriev, M.N., Hubberten, H.-W., Lisitzin, A.P., Shevchenko, V., Schirrmeister, L., 2004. Modern terrigenous organic carbon input to the Arctic Ocean, The organic carbon cycle in the Arctic Ocean. Springer, pp. 33-55.

Rampton, V.N., 1982. Quaternary Geology of the Yukon Coastal Plain. Geological Survey of Canada.

Rawlins, M., Nicolsky, D., McDonald, K., Romanovsky, V., 2013. Simulating soil freeze/thaw dynamics with an improved pan-Arctic water balance model. Journal of Advances in Modeling Earth Systems 5, 659-675.

Retamal, L., Bonilla, S., Vincent, W.F., 2008. Optical gradients and phytoplankton production in the Mackenzie River and the coastal Beaufort Sea. Polar Biology 31, 363-379.

Romanovsky, V., Burgess, M., Smith, S., Yoshikawa, K., Brown, J., 2002. Permafrost temperature records: indicators of climate change. EOS, Transactions American Geophysical Union 83, 589-594.

Romanovsky, V.E., Smith, S.L., Christiansen, H.H., 2010. Permafrost thermal state in the polar Northern Hemisphere during the international polar year 2007–2009: A synthesis. Permafrost and Periglacial Processes 21, 106-116.

Schaefer, K., Lantuit, H., Romanovsky, V.E., Schuur, E.A., Witt, R., 2014. The impact of the permafrost carbon feedback on global climate. Environmental Research Letters 9, 085003.

Schaefer, K., Zhang, T., Bruhwiler, L., Barrett, A., 2011. Amount and timing of permafrost carbon release in response to climate warming. Tellus B 63, 165-180.

Schirrmeister, L., Kunitsky, V., Grosse, G., Wetterich, S., Meyer, H., Schwamborn, G., Babiy, O., Derevyagin, A., Siegert, C., 2011. Sedimentary characteristics and origin of the Late Pleistocene Ice Complex on north-east Siberian Arctic coastal lowlands and islands–A review. Quaternary international 241, 3-25.

Schuur, E., McGuire, A., Schädel, C., Grosse, G., Harden, J., Hayes, D., Hugelius, G., Koven, C., Kuhry, P., Lawrence, D., 2015. Climate change and the permafrost carbon feedback. Nature 520, 171-179.

Schuur, E.A., Bockheim, J., Canadell, J.G., Euskirchen, E., Field, C.B., Goryachkin, S.V., Hagemann, S., Kuhry, P., Lafleur, P.M., Lee, H., 2008. Vulnerability of permafrost carbon to climate change: implications for the global carbon cycle. BioScience 58, 701-714.

Screen, J., Simmonds, I., 2010. The central role of diminishing sea ice in recent Arctic temperature amplification. Nature 464, 1334-1337.

Séjourné, A., Costard, F., Fedorov, A., Gargani, J., Skorve, J., Massé, M., Mège, D., 2015. Evolution of the banks of thermokarst lakes in Central Yakutia (Central Siberia) due to retrogressive thaw slump activity controlled by insolation. Geomorphology 241, 31-40.

Shepard, F.P., 1954. Nomenclature based on sand-silt-clay ratios. Journal of Sedimentary Research 24.

Skogerboe, G., Bennett, R., Walker, W., 1972. Generalized discharge relations for cutthroat flumes. Journal of Irrigation and Drainage Engineering 98.

Smith, C., Kennedy, C., Hargrave, A., McKenna, K., 1989. Soil and vegetation survey of Herschel Island, Yukon Territory. Yukon Soil Survey Report.

Streletskiy, D.A., Shiklomanov, N.I., Nelson, F.E., 2012. Permafrost, infrastructure, and climate change: a GIS-based landscape approach to geotechnical modeling. Arctic, Antarctic, and Alpine Research 44, 368-380.

Subcommittee, P., 1988. Glossary of permafrost and related ground-ice terms. Associate Committee on Geotechnical Research, National Research Council of Canada, Ottawa, 156.

Tanski, G., 2013. Release of dissolved organic carbon from coastal erosion into the southern Canadian Beaufort Sea. Freie Universität Berlin/Alfred Wegener Institute Helmholtz Centre for Polar and Marine Research.

Tanski, G., Couture, N., Lantuit, H., Eulenburg, A., Fritz, M., 2016. Eroding permafrost coasts release low amounts of dissolved organic carbon (DOC) from ground ice into the nearshore zone of the Arctic Ocean. Global Biogeochemical Cycles.

Vavrus, S., Waliser, D., Schweiger, A., Francis, J., 2009. Simulations of 20th and 21st century Arctic cloud amount in the global climate models assessed in the IPCC AR4. Climate Dynamics 33, 1099-1115.

Vonk, J., Mann, P., Dowdy, K., Davydova, A., Davydov, S., Zimov, N., Spencer, R., Bulygina, E., Eglinton, T., Holmes, R., 2013. Dissolved organic carbon loss from Yedoma permafrost amplified by ice wedge thaw. Environmental Research Letters 8, 035023.

Vonk, J., Sánchez-García, L., Van Dongen, B., Alling, V., Kosmach, D., Charkin, A., Semiletov, I.P., Dudarev, O.V., Shakhova, N., Roos, P., 2012. Activation of old carbon by erosion of coastal and subsea permafrost in Arctic Siberia. Nature 489, 137-140.

Walker, W.R., Skogerboe, G.V., 1987. Surface irrigation. Theory and practice. Prentice-Hall.

Wolfe, S., Kotler, E., Dallimore, S., 2001. Surficial characteristics and the distribution of thaw landforms (1970 to 1999), Shingle Point to Kay Point, Yukon Territory. Geological Survey of Canada, Open File 4115, 18.

Woo, M.-k., Lewkowicz, A.G., Rouse, W.R., 1992. Response of the Canadian permafrost environment to climatic change. Physical geography 13, 287-317.

Zhang, T., Barry, R.G., Knowles, K., Heginbottom, J., Brown, J., 1999. Statistics and characteristics of permafrost and ground-ice distribution in the Northern Hemisphere 1. Polar Geography 23, 132-154.

Zimov, S., Davydov, S., Zimova, G., Davydova, A., Schuur, E., Dutta, K., Chapin, F., 2006. Permafrost carbon: Stock and decomposability of a globally significant carbon pool. Geophysical Research Letters 33, L20502.

Zoltai, S., Pettapiece, W., 1973. Terrain, vegetation and permafrost relationships in the northern part of the Mackenzie Valley and northern Yukon. Environmental-Social Committee, Northern Pipelines. Task Force on Northern Oil Development. report, 105.

10. Financial and technical support

This work has been supported by the PAGE21 project, grant agreement number 282700, funded by the EC seventh Framework Programme theme FP7-ENV-2011. Further, this research was supported by the Helmholtz Young Investigator's group "COPER" (grant VH-NG-801 to H. Lantuit) and by the German Federal Ministry of Education and Research (grants CAN 09/001 and 01DM12002 to H. Lantuit). In addition, I would like to thank the Alfred Wegener Institute Helmholtz Centre for Polar and Marine Research for their logistical and financial support. I would like to acknowledge the support for numerous Workshops, travel grants and the POLMAR Outgoing Scholarship financed by the Helmholtz Graduate School for Polar and Marine Research- POLMAR. Further, I am grateful for the support for workshops and travel grants financed by the Potsdam Graduate School-POGS. I am deeply grateful for the administrative and logistical support of the Aurora Research Institute and Parks Canada office in Inuvik.

11. Acknowledgement - Danksagung

Zuerst möchte ich mich bei **Hugues Lantuit** bedanken: für seine kreativen Ideen, seine ansteckende Begeisterung und das Verständnis, welches er mir in schwierigen Zeiten entgegen brachte. Insbesondere bedanke ich mich für die unendlich vielen Möglichkeiten, die er mir gab, ein eigenes internationales Netzwerk aufzubauen und mir mit vielen wertvollen Ratschlägen zur Seite stand. Es war sehr schön, dass Hugues seine COPERniküsse als Teil seiner Familie betrachtet, und wir mit unseren queren Charakteren ein sehr gutes Team bilden, u.a. mit vielen konstruktiven und lustigen Gruppentreffen bei Kaffee und Kuchen oder eigenartigen Momenten in Kanada. Vor allem Hugues ansteckende Begeisterung für Herschel Island, sein Gespür für das angemessene Verhalten in der vielseitigen kanadischen Kultur und sein Glaube, dass eine Messstation in einem hochdynamischen System überleben kann, haben mir zu dieser Dissertation verholfen. Selbst die klitzekleine Schlammlawine, die die Messstation auf die Hälfte der Größe zusammenfaltete, hat seinem Enthusiasmus nichts angetan und so buddelte er auch im nächsten Jahr wieder fleißig und voller Begeisterung mit uns im Schlamm. Damit bedanke ich mich besonders bei ihm und den Copernikü̈ssen für die vielen Hilfen beim Buddeln im Schlamm und gegenseitigen aus dem Dreck ziehen in allen Lebenslagen.

Ich möchte mich bei **Hans-Wolfgang Hubberten** bedanken, den ich erstmals auf Spitzbergen an der Universität traf. Insbesondere bedanke ich mich bei ihm für seine konstruktiven Ratschläge aus seiner langjährigen Erfahrung und seine unterstützende Begeisterung für jegliche Aktivitäten der Nachwuchswissenschaftler. Diese haben sehr geholfen neue Projekte ins Leben zu rufen und so haben wir wieder ein europäisch-kanadisches Netzwerk auch auf Nachwuchswissenschaftlerebene.

Des Weiteren möchte ich mich bei **Paul Overduin** bedanken. Sein offenes Ohr und die zahlreichen neuen Ideen (inklusive neuster interessanter Zeichnungen) waren immer eine sehr große Hilfe. Ein Treffen mit ihm hat mir immer wieder geholfen, die Doktorarbeit richtig im wissenschaftlichen Sinn und im Leben einzuordnen. Seine größte Hilfe war die Aussage: „Steffi, du bist ganz normal“. Vielen Dank Paul, es hat sehr geholfen!

Besonders danken möchte ich für die unschätzbare Hilfe, die lustigen Momente und die kritisch-konstruktiven Ratschläge im Labor **Antje Eulenburg**, **Ute Kuschel**, **Dyke**

Scheidemann, **Daniel Gorzawski**, **Izabela Milczarek**, **Stefanie Hohberg**, **Hanno Meyer**, **Lutz Schönicke**, **Sylvia Pinkerneil** und **Birgit Plessen**.

Eine große menschliche Komponente zur Fertigstellung der Doktorarbeit habe ich zwei wundervollen Frauen zu verdanken. **Claudia Hanfland** und **Claudia Sprengel** danke ich für herzliche, aufmunternde und einfühlsame Ratschläge, sowie schließlich sanfte Schubser zur Zielgrade. Ihr beide seid das Herz des AWIs. Vielen Dank auch, dass ihr mit POLMAR immer wieder finanzielle Unterstützung für Workshops und Konferenzen gegeben habt.

Ein besonders herzlicher Dank gilt **Heiko Gericke** und **Tobias Schmidt** für die manchmal fast täglichen SOS Hilfen, wenn der Rechner mal wieder irgendwo aufschrie oder in einen plötzlichen Ruhestreik ging. Ich danke euch beiden für eure unermüdliche Geduld mit meiner computertechnischen Ahnungslosigkeit.

Vielen Dank möchte ich an **Frau Litz** und **Frau Gräning** richten, insbesondere da sie sehr zeitige Wochenend-Anrufe der Pforte freundlich entgegen nahmen und in der Endphase sofort ein Schreiben für die Pforte aufsetzten, dass ich spontan Nacht- und Wochenendschichten einlegen konnte! Ein herzliches Dankeschön gilt **Frau Otto**, mein persönlicher Sherlock Holmes, die mich immer in kürzester Zeit mit Literatur versorgte und selbst, wenn diese nicht aufzufinden war, mich mit Kontaktdaten der Autoren versorgen konnte. Ein besonderer Dank geht an **Conrad Kopsch** für seine unermüdliche Hilfe mit den Wetterstationen und dem Flume. Conny, ohne dich wäre ich ganz schön arm dran gewesen! Ein lieber Dank geht an **Birgit Heim**, die mich in den letzten Wochen immer wieder mit lustigen Anekdoten und motivierenden Geschichten aus eigener Erfahrung unterstützt hat.

I am grateful for all the international exchange we had at the AWI. **Scott Lamoureux**, **Toni Lewkowicz** and **Denis Mercier** brought an invaluable expertise to the AWI and shared their knowledge. Thank you very much for all the scientific and personal dialogs and ideas we have exchanged! Special thanks goes to Scott and **Linda Lamoureux**, **Ashley Rudy**, **Julie Lepage** and **Benoit Loranger** who gave me a warm welcome and introduced me to their beautiful country and culture. In uncountable dinner invitations I experienced the tastiest south Canadian cuisine. **Liz Kjikjerkovska** gave me amazing support in Canada and during the last years. I am grateful for the most beautiful holiday in Macedonia!

I would like to acknowledge the amazing help the rangers **LeeJohn Meyook**, **Ricky Joe**, **Samuel McLeod**, **Edward McLeod** and **Richard Gordon** have been during the field work in 2012 and 2013. They made me feel home and welcomed, showed me their life and why their

land is such a beautiful place and so valuable. Thank you very much for all the knowledge and tasty fresh hunted food you shared, the uncountable spontaneous help, the funny card games, your personal thoughts in the evening after long days in the field and that you showed me how to fish and how to cut a fish to a perfect filet for having the most tastiest smoked fish on earth.

There were a lot of moments during the last years were I was grateful for amazing support. Herewith I would like to thank **Leena-Kaisa Viitanen** and **Heike Midleja** for their support in PAGE 21. Further, I would like to thank for their help and knowledge during expedition **Wayne Pollard**, **Christopher Burn**, **Michael Krautblatter**, **Michael Angelopoulos**, and **David Fox** (It was difficult to find an image for this thesis without the chain saw written "I love Nat" heart in the thaw slump) and **Isla Myers-Smith** and **Louise Beveridge** for funny and tasty moments. Further I would like to thank a fantastic "**EUCOP workshop**", "**Frozen-Ground Cartoon**" and "**Frozen Fable" team**. It was amazing to see what can be produced with short notice and a lot of enthusiastic friends!

I would like to thank **Matthew Jones**. Somehow this thesis started with a tasty Burrito in Berlin, a phone call from Hugues and your advice to take each year all of my holidays. This advice was one of the most valuable you could give to me as my holidays always recharged my batteries to keep on going and to finish this thesis. And now gratefully, this thesis ends with your final English proofread in the Material and Method section!

Ich bedanke mich bei jedem einzelnen **COPERnikuss**. Für eure unermüdliche Hilfe im Gelände und die zahlreichen Gespräche in den letzten Jahren. Die Wetterstation, an der sich Bären so gern den Rücken kratzen, hätte ohne diverse Huckepack-Aktionen nicht errichtet werden können, zahlreiche Schlammproben, und Daten auslesen, wäre nicht ohne euch möglich gewesen (insbesondere **Juliane Wolter** und **Ute Kuschel**). Vor allem Jule danke, dass du die Gelände-Schokolade verwaltet hast und besonders auf die gelben M&M´s geachtet hattest. Vielen Dank **Michael Fritz** und **George Tanski** bei der Beprobung der Slumps. Insbesondere George vielen Dank für deine unglaubliche Geduld, die viele tatkräftige Hilfe im Gelände, und für die Wochen, die du für uns mit den Packlisten verbracht hast. Lieben Dank **Anna Irrgang** und **Boris Radosavljevic** für eure DGPS Kenntnisse, und die unzähligen Gespräche. **Jaroslav Obu**, danke für die LiDAR Datenauswertung und **Justine Ramage**, vielen Dank für die Slump Daten entlang der Yukon Küste (und noch viel mehr für deine leckeren Kuchen). Die Daten sind ein wichtiger Teil dieser Doktorarbeit

geworden. Vielen Dank für die zahlreichen Leckereien, die alle immer zu den Gruppentreffen mitgebracht haben. Sie haben einem Arbeitstreffen ein familiäres Gefühl gegeben.

Nicht nur die Copernikusse waren an einem schönen Arbeitsumfeld beteiligt. Die lustigen und hilfreichen Gespräche mit **Fabian Kneier** (du machst das beste Eis der Stadt), **Katrin Kohnert** (für die vielen schönen Gespräche zwischen Tür und Angel und insbesondere für die Nervennahrung in den letzten 24 Stunden) **Liv Heinecke**, **Mareike Wieczorek**, **Bastian Niemeyer**, **Stefan Kruse**, **Heike Zimmermann** (ich grinse immer noch heimlich) und **Romy Zibulski** (wo bleibt eigentlich die zweite Auflage des Borkenkäfers) haben den Doktorandenalltag immer aufgeheitert und den administrativen Dschungel verständlicher gemacht. Insbesondere **Jens Strauß**, mit seiner verständnisvollen Art, hat so einige Nervenflatterer von mir beruhigt. Vielen Dank für deine wissenschaftlichen, administrativen und zwischenmenschlichen Ratschläge!

Interessanter weise wurde während meines Geologie Studiums Mathematik von vier Semestern auf drei Semester reduziert und dabei das einzig nützliche, das Statistiksemester, gestrichen. Diese Doktorarbeit wäre ohne **Christopher Irrgang**, **Bert Gollnick** und **André Beinrucker** signifikant schlechter ausgefallen. Vielen Dank!

Lieben Dank möchte ich an **Boris Radosavljevic** aussprechen. Es ist nicht alles aufzuzählen, was wir seit dem 1. April 2012 gemeinsam erlebt haben: Ein überglücklicher Boris im farbigen Shirt am ersten Tag, ein ausgiebiger IKEA Besuch, viele Radtouren, mentale und tatkräftige Unterstützung im Gelände, unzählige Computer, R Statistik und DGPS Hilfen, viel Schnaps, noch mehr Meierei-Bier, sehr viel leckeres Essen und deine unendliche Gastfreundschaft. Boris ohne dich wäre Potsdam nicht mein Zuhause geworden!

Ein wichtiger Teil meines Lebens sind in den letzten Jahren **Karina Schollän**, **Josefine Lenz** und **Anna Irrgang** geworden. Danke Karina, dass ich die ersten drei Monate auf deiner Couch schlafen durfte und ihr mich in deiner Familie immer so herzlich aufnehmt. Danke, dass du immer so auf Endnote gepocht hast! Josi und Anna, euch verdanke ich viele intensive Gespräche und auch einige Kater.

Niklas Allroggen und **Katrin Hannemann** verdanke ich eine lange Freundschaft und sehr viele lustige Momente, immer verbunden mit fantastischem Frühstück oder gemütlichen Kochabenden. Lieben Dank **Tina Swierczynski** für die vielen gemütlichen Momente bei Kaffee und Wein.

Danke **Gabi Gollnick**, **Anne Ahrens**, **Corinna Backasch** und **Julia Ely** für unsere langjährigen Freundschaften durch alle Höhen und Tiefen. **Jules Probst**, du bist mein Sonnenschein und zeigst mir immer wieder wie schön und wertvoll das Leben ist.

Ich bin sehr froh, dass **Caroline Coch** eines Abends spontan ihr Interesse für Craftbeer entdeckte und sich dies zu einer sehr engen Freundschaft mit Massen an Eiscreme entwickelte. Vielen Dank, dass du all diese Discharge-Berechnungen noch einmal nachgerechnet hast. Deine asiatischen Kochkünste sind einfach glückselig machend und verhalfen locker flockig mal eben gemeinsam das Diskussionskapitel aufzustellen. Ich habe immer noch deine Worte im Ohr „Willst du das etwas so lassen?“ Danke, danke dass du mir in meiner „ist doch fertig“- Mentalität mit dem Layout geholfen hast!

Fiona Tummon is the main reason that this thesis was finished in only 49 days. I am not even sure which language I should write now as you are not only my friend. Here, you are my translator, my support, my hope and the person who believes in me! Du bist meine Freundin seitdem ich dich das erste Mal mit pinken Füssen sah. Wir gehen durch alle Höhen und Tiefen und wir haben die wunderschönsten und traurigsten Momente gemeinsam verbracht. Danke, dass du immer für mich da bist, ohne jeden Zweifel und ohne jegliches Zögern! Danke, dass du gesagt hast, dass ich es schaffe und diese Doktorarbeit innerhalb von vier Tagen einmal vollständig auf das englische Herz und dessen Seele geprüft hast. Ohne dich wäre es nicht möglich gewesen!

In den letzten drei Jahren ist mir mehrfach bewusst geworden, dass man sein Leben nicht immer planen kann und dieses immer viel zu früh endet. Danke, **Julia Wittig**, dass du mir gezeigt hast, dass man alles im Leben schaffen kann, egal ob in der Antarktis zu überwintern oder eine Boeing zu fliegen, wenn man nur wirklich an sich glaubt. Du hast mir gezeigt, das Leben und jeden einzelnen Augenblick mit einem Lachen zu genießen. Nach der Abgabe trinke ich einen Sekt auf dich!

Und das Beste kommt zum Schluss. Ich danke meiner **Familie** für ihre bedingungslose Liebe, nie endende Fürsorge, ihre tatkräftige Hilfe, die seelische Unterstützung, das viele leckere Essen, die gemeinsamen sehr lustigen und besonders laut quasseligen Momente. Hätten **Oma** und **Opa** nicht solch eine liebevolle Familie geschaffen, die einander so sehr liebt und gegenseitig unterstützt, wäre diese Arbeit nicht entstanden. **Mama, Papa, Kathi, René, Melina, Netti, Thomas, Madelyn, Christopher** und nun auch **André**, ihr seid das Wichtigste in meinem Leben!

Eidesstattliche Erklärung

Hiermit versichere ich, dass ich die vorliegende Arbeit selbstständig verfasst und keine anderen als die angegebenen Quellen und Hilfsmittel verwendet habe.

Ich habe diese Dissertation am Alfred-Wegener-Institut Helmholtz Zentrum für Polar und Meeresforschung in Potsdam erarbeitet und in englischer Sprache angefertigt. Diese Dissertation wird erstmalig und ausschließlich an der Universität Potsdam eingereicht.

Die dem Promotionsverfahren zugrundeliegende Promotionsordnung vom 18.09.2013 ist mir bekannt.

Potsdam, den 23.11.2016 Stefanie Weege

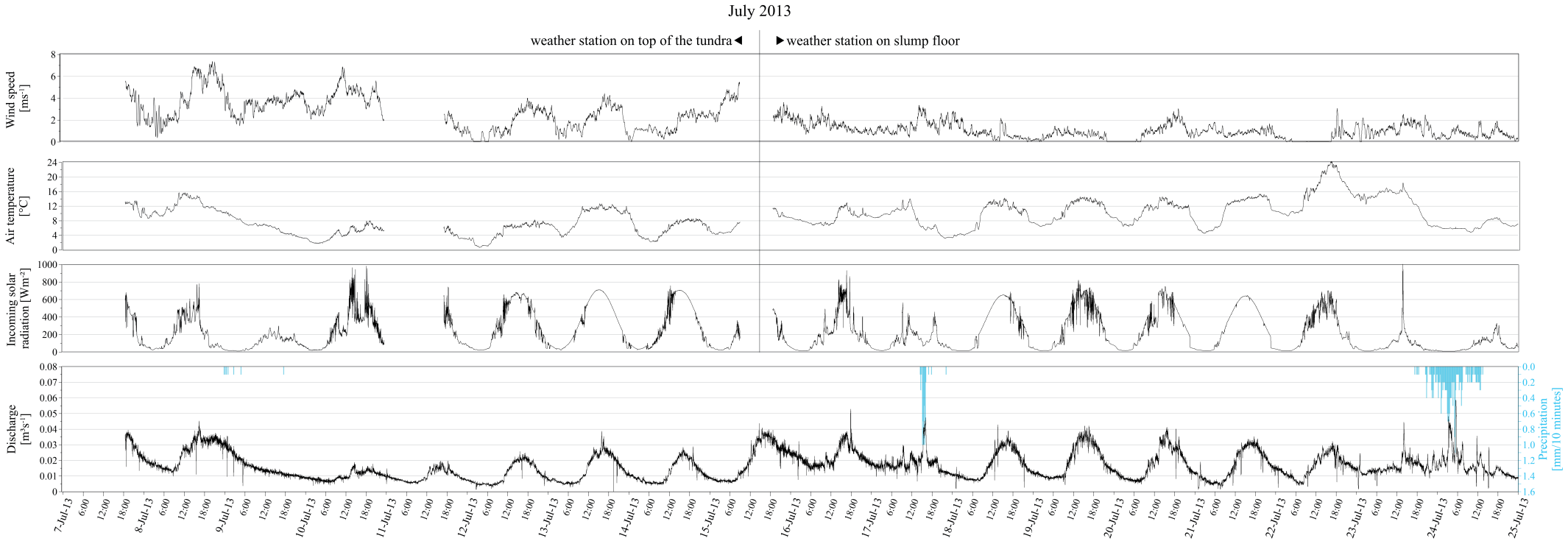
July 2013
weather station on top of the tundra◄
►weather station on slump floor
Wind speed [ms-1]
Air temperature [°C]
Incoming solar radiation [Wm-2]
Discharge [m3s-1]
Precipitation [mm/10 minutes]
7-Jul-13
8-Jul-13
9-Jul-13
10-Jul-13
11-Jul-13
12-Jul-13
13-Jul-13
14-Jul-13
15-Jul-13
16-Jul-13
17-Jul-13
18-Jul-13
19-Jul-13
20-Jul-13
21-Jul-13
22-Jul-13
23-Jul-13
24-Jul-13
25-Jul-13

August 2012

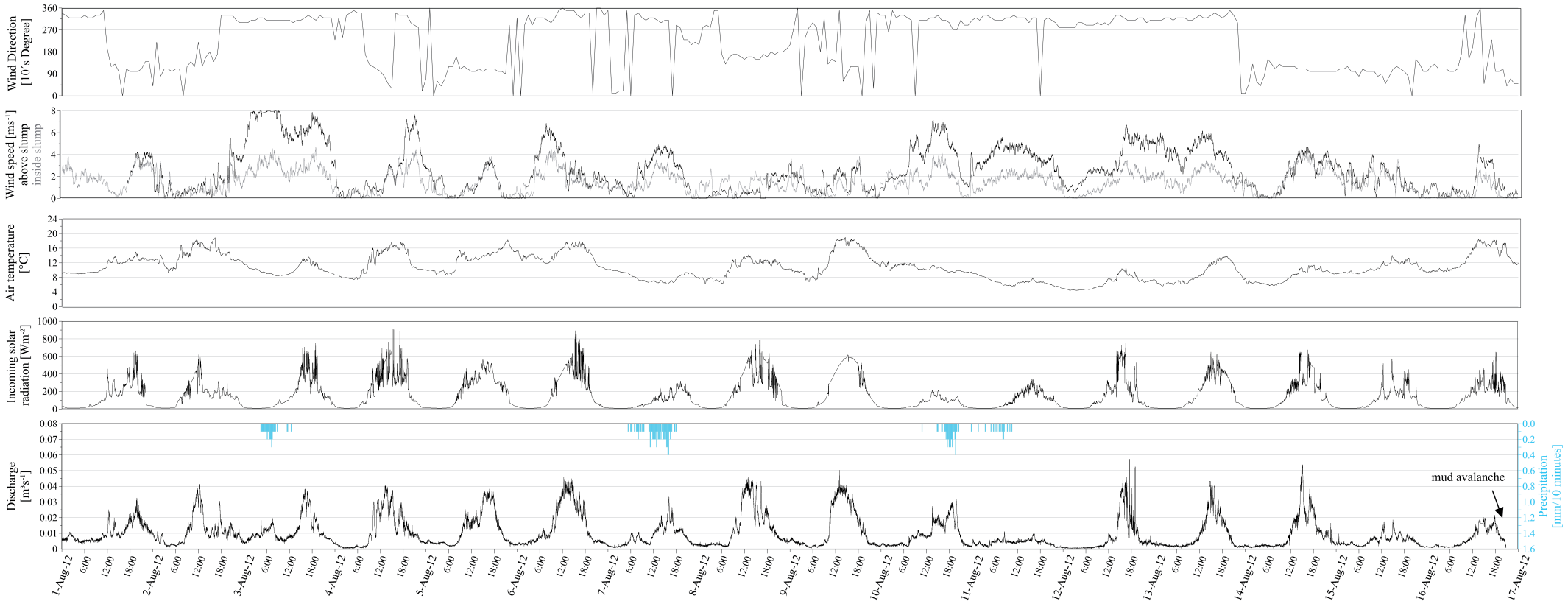
Wind Direction [10's Degree]
360
270
180
90
0
Wind speed [ms-1] above slump
inside slump
8
6
4
2
0
Air temperature [°C]
24
20
16
12
8
4
0
Incoming solar radiation [Wm-2]
1000
800
600
400
200
0
Discharge [m³s-1]
0.08
0.07
0.06
0.05
0.04
0.03
0.02
0.01
0
Precipitation [mm/10 minutes]
0.0
0.2
0.4
0.6
0.8
1.0
1.2
1.4
1.6
mud avalanche
1-Aug-12
2-Aug-12
3-Aug-12
4-Aug-12
5-Aug-12
6-Aug-12
7-Aug-12
8-Aug-12
9-Aug-12
10-Aug-12
11-Aug-12
12-Aug-12
13-Aug-12
14-Aug-12
15-Aug-12
16-Aug-12
17-Aug-12
6:00
12:00
18:00